
WIND TUNNELS

Edited by **Satoru Okamoto**

INTECHWEB.ORG

Wind Tunnels

Edited by Satoru Okamoto

Published by InTech

Janeza Trdine 9, 51000 Rijeka, Croatia

Copyright © 2011 InTech

All chapters are Open Access articles distributed under the Creative Commons Non Commercial Share Alike Attribution 3.0 license, which permits to copy, distribute, transmit, and adapt the work in any medium, so long as the original work is properly cited. After this work has been published by InTech, authors have the right to republish it, in whole or part, in any publication of which they are the author, and to make other personal use of the work. Any republication, referencing or personal use of the work must explicitly identify the original source.

Statements and opinions expressed in the chapters are these of the individual contributors and not necessarily those of the editors or publisher. No responsibility is accepted for the accuracy of information contained in the published articles. The publisher assumes no responsibility for any damage or injury to persons or property arising out of the use of any materials, instructions, methods or ideas contained in the book.

Publishing Process Manager Ivana Lorkovic

Technical Editor Teodora Smiljanic

Cover Designer Martina Sirotic

Image Copyright corepics, 2010. Used under license from Shutterstock.com

First published February, 2011

Printed in India

A free online edition of this book is available at www.intechopen.com

Additional hard copies can be obtained from orders@intechweb.org

Wind Tunnels, Edited by Satoru Okamoto

p. cm.

ISBN 978-953-307-295-1

INTECH OPEN ACCESS
PUBLISHER

INTECH open

free online editions of InTech
Books and Journals can be found at
www.intechopen.com

Contents

Preface VII

Part 1 Wind Tunnel Technologies and Devices 1

- Chapter 1 **Environmental Wind Tunnels 3**
Jonathan Merrison
- Chapter 2 **Dynamically Improved 6-DOF System for Measurements of Forces and Torques in Wind Tunnels 23**
V. Portman, B. Sandler and V. Chapsky
- Chapter 3 **Stiffness Enhancement and Motion Control of a 6-DOF Wire-driven Parallel Manipulator with Redundant Actuators for Wind Tunnels 41**
Xin Liu, Yuanying Qiu and Xuechao Duan
- Chapter 4 **Rebuilding and Analysis of a SCIROCCO PWT Test on a Large TPS Demonstrator 57**
Sara Di Benedetto, Giuseppe C. Rufolo,
Marco Marini and Eduardo Trifoni
- ### **Part 2 Applications of Wind Tunnels Testing 85**
- Chapter 5 **Flow Visualization and Proper Orthogonal Decomposition of Aeroelastic Phenomena 87**
Thomas Andrianne, Norizham Abdul Razak
and Grigorios Dimitriadis
- Chapter 6 **Wind Tunnel Testing of Pneumatic Artificial Muscles for Control Surface Actuation 105**
Curt S. Kothera and Norman M. Wereley
- Chapter 7 **Experimental Study of Flow-Induced Vibrations and Scattering of Roof Tiles by Wind Tunnel Testing 121**
Satoru Okamoto

Preface

Wind tunnels are the primary research tools used in aerodynamic research. They are used to study the effects of air moving past solid objects. Although great advances in computational methods have been made in recent years, wind tunnel tests remain essential for obtaining the full range of data required to guide detailed design decisions for various practical engineering problems.

This book collects original and innovative research studies on recent applications in wind tunnel tests, exhibiting various investigation directions and providing a bird's eye view on this broad subject area. It is composed of seven chapters that have been grouped in two major parts. The first part of the book (chapters 1–4) deals with wind tunnel technologies and devices. The second part (chapters 5–7) deals with the latest applications of wind tunnel testing.

The following is a brief description of the subjects that are covered in each chapter:

Chapter 1 reviews some examples of environmental wind tunnels.

Chapter 2 describes a 6-DOF system for the measurements of forces and torques in wind tunnels.

Chapter 3 proposes a 6-DOF wire-driven parallel manipulator with redundant actuations for wind tunnels.

Chapter 4 introduces the plasma wind tunnel test on a large thermal protection system demonstrator.

Chapter 5 describes the flow visualization and the proper orthogonal decomposition of aeroelastic phenomena.

Chapter 6 introduces the wind tunnel testing of pneumatic artificial muscles.

Chapter 7 provides the flow-induced vibrations and scattering of roof tiles by wind tunnel testing.

The text is addressed not only to researchers but also to professional engineers, engineering lecturers, and students seeking to gain better understanding of the current status of wind tunnels.

Through its seven chapters, the reader will have an access to a wide range of works related to wind tunnel testing.

I am extremely honored to be editing such a valuable book, which contains contributions of a selected group of researchers describing the best of their work. I would like to express my sincere gratitude to all of them for their outstanding chapters.

I also wish to acknowledge the InTech editorial staff, in particular Ms. Ivana Lorković, for indispensable technical assistance in book preparation and publishing.

Prof. Satoru Okamoto
Department of Mathematics and Computer Science
Shimane University
Matsue Japan

Part 1

Wind Tunnel Technologies and Devices

Environmental Wind Tunnels

Jonathan Merrison
Aarhus University,
Denmark

1. Introduction

Wind tunnels have been used extensively in industry and research applications over the past 50 years. They vary greatly in scale and geometry, with some large enough to house and test small aircraft (see for example NASA, ATP facilities) and others are miniaturized flow generators used in the calibration of small sensors. However they invariably utilize the same basic technology and design elements. Similarly environmental simulators are also used widely in research, for example in climate and planetary studies. Here again they superficially vary greatly in size and configuration, but basically consist of a hermetic chamber with some form of temperature control [Jensen et al. 2008]. There is therefore a broad array of standard and often commercial technologies and construction techniques which have been successfully applied within the fields of wind tunnel and environmental simulator design. Some of these technologies and techniques will be outlined in this chapter to aid researchers or technology developers in their efforts to design or use environmental wind tunnels and also serve as an informative guide to those new to these fields of investigation.

The fusion of an environmental simulator and a wind tunnel is a natural evolution of laboratory based technology to fulfill the need to reproduce specific physical conditions found in nature. Although facilities of this kind are only now being fully developed, they have the potential to expand into a new research field that could substantially contribute to our understanding of climate and mediate growth in advanced sensor technologies. In this chapter many of the challenges in designing and constructing environmental wind tunnels will be introduced and possible solutions presented, with some emphasis placed on extreme terrestrial and Martian planetary conditions. In addition some of the many and varied scientific and industrial applications will be discussed. Generally environmental wind tunnels are already in current use as a method of testing and calibrating meteorology sensors of various kinds especially wind flow sensors (anemometers). Application of wind tunnels in civil engineering and town planning is becoming common place. Here through wind tunnel simulation and modeling the flow of air around buildings and through built-up areas may be useful to avoid the generation of high wind shear and hazardous vortices at periods of high wind or storms. Such simulations can also aid in the design and placement of wind generation systems such as wind turbines.

The formalized scaling laws developed by *Reynolds* (Reynolds equations) allows measurements, for example in smaller scale laboratory wind tunnels, which generate the same (or extremely similar) flow to that generated in the natural setting [Monin and Yaglom

1973, Hall 1988, Mollinger and Nieuwstadt 1996, Fay and Sonwalkar 1991]. This scaling law involves the relationship between wind speed, spatial scale and viscosity such that adjusting and combining these parameters can allow realistic laboratory simulation for example on the cm-m scale of flow dynamics on the 10s to 100s of meters. It can also, for example, allow comparison of effects in one fluid (e.g. air) to be translated into those seen in another fluid such as water. This technique has been successfully applied in the design of all forms of transport, such as aircraft, ships and cars.

Wind tunnel studies have and are contributing powerfully in attempts to understand and describe the action of wind in arid areas. Following the pioneering work of *Bagnold*, including the use of laboratory (and field) wind tunnels, the study of Aeolian (wind driven) sand transport has evolved into a scientific research field [Bagnold 1941]. It is now clear that Aeolian transport has a great impact on local environments and on the global climate through the production of aerosols, the erosion of surface material and the serious environmental problem of desertification. Aeolian transport of sand/dust under planetary conditions other than Earth's is also of great importance to understanding these extreme environments and can help achieve a deeper understanding of our own environment. For example Aeolian processes are seen on Mars, Venus and Saturn's moon Titan, but are probably found on any planetary body with a significant atmosphere. Sand features such as dunes are common on these planets and in the case of Mars dust entrainment is seen to be the most powerful climatic factor. Interesting differences in the Aeolian features seen in these extra-terrestrial environments is the spatial scale compared to those on Earth. The study of extra terrestrial Aeolian phenomena can only effectively be studied in the laboratory using an environmental wind tunnel simulator. Even with such simulators, only some aspects of Aeolian transport on other planets can be successfully reproduced, such as the surface shear stress, wind speed, fluid density, temperature, humidity and (more ambitiously) surface microstructure, adhesive properties. Other physical aspects are extremely problematic, for example gravity and specifics of the surface composition (mineralogy).

An obvious application for an environmental wind tunnel is the study of the upper atmosphere (the troposphere and stratosphere), specifically low temperatures, low pressures and the presence of aerosols of various types. Clearly this is of relevance to the aircraft industry, especially (high altitude) jet aircraft. The recent (2010) disturbance in Atlantic flights due to the generation of dust aerosols by the Icelandic volcano (Eyjafjallajökull) is a good example, where a deeper understanding of these aerosols in the upper atmosphere could possibly have avoided a large degree of disruption. The development of new aerosol sensor technologies also appears to be necessary. In fact wind tunnels can both help to unravel the complex dynamics of aerosol behavior and to understand their formation processes through the generation of fine suspended mineral particulates (dust). It should be stressed here that the study of aerosols is far from being limited to a global climatic factor. Aerosols present a real hazard to environmental and human safety both in the home and in local environments. Conversely aerosols are also used widely in medicine and the pharmaceutical and cosmetics industries. Specifically nano-micro meter scale particulates suspended in the air can penetrate the deep lung as well as be suspended for long periods of time (months) in the atmosphere and transported great distances (globally). Smoke, clouds, dust, are just some of the many forms of aerosol that affect our environment and can be studied in environmental wind tunnels to better understand their (apparently complex) behavior as well as develop new technology in order to quantify and control them.

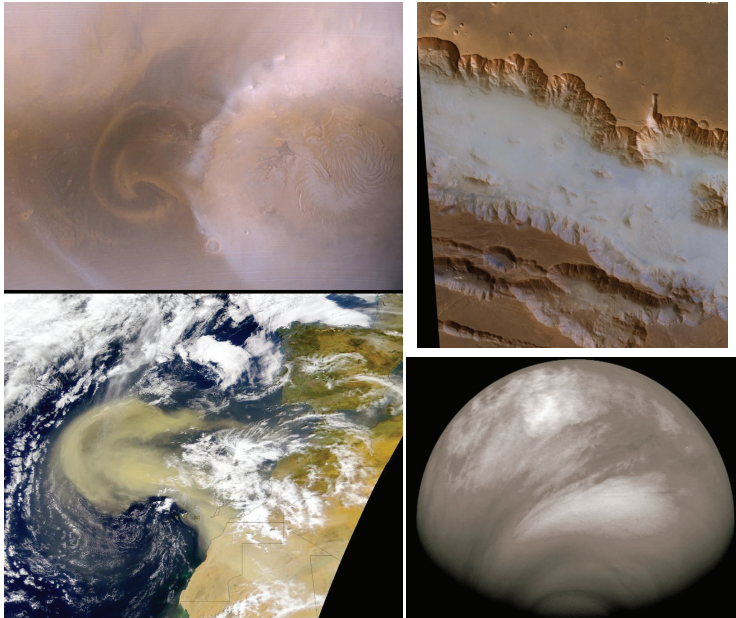


Fig. 1. Left upper and lower; satellite photographs of Mars and Earth, North Africa respectively, showing dust storms and clouds. (Courtesy NASA/JPL-Caltech). Right upper fog in Mars, Valles Marineris taken by the High Resolution Stereo Camera (HRSC) on board ESA's Mars Express spacecraft, Right lower; acid haze seen amongst the thick clouds of Venus, photographed by the ESA's Venus Express spacecraft.

In the future the study of aerosols will probably be the single most important application of environmental wind tunnels and it is hoped that the work presented here will contribute towards these types of study.

2. Environmental wind tunnel mechanical design

There are two basic types of wind tunnel design which may be referred to as Open Circuit or Closed Circuit (or closed cycle). In a terrestrial (ambient pressure) open circuit wind tunnel design fresh air is drawn (or blown) into the entrance and expelled at the exit, whereas in a closed circuit wind tunnel the expelled air is fed again into the inlet such that the same air is re-circulated. Either of these two wind tunnel types can be housed in an environmental (or planetary simulation) chamber giving rise to two distinct types of environmental wind tunnel design. These different wind tunnel types (shown schematically in figures 2a-2d) have distinct characteristics, their advantages and disadvantages will be discussed.

The implementation of thermal and flow control within these differing system designs will vary. In the case of the open circuit design flow and thermal control systems should be implemented upwind and focus primarily on manipulating the gas which is inlet. In the case of a re-circulating design, since the system is a closed cycle, flow correction and thermal control can in principle be implemented in any (or all) sections of the circuit. In practice the

implementation of thermal control will depend on the thermal control system chosen and general technical restraints of the wind tunnel design. Similarly flow control will depend on the desired flow characteristics and the practical limitations on resources.

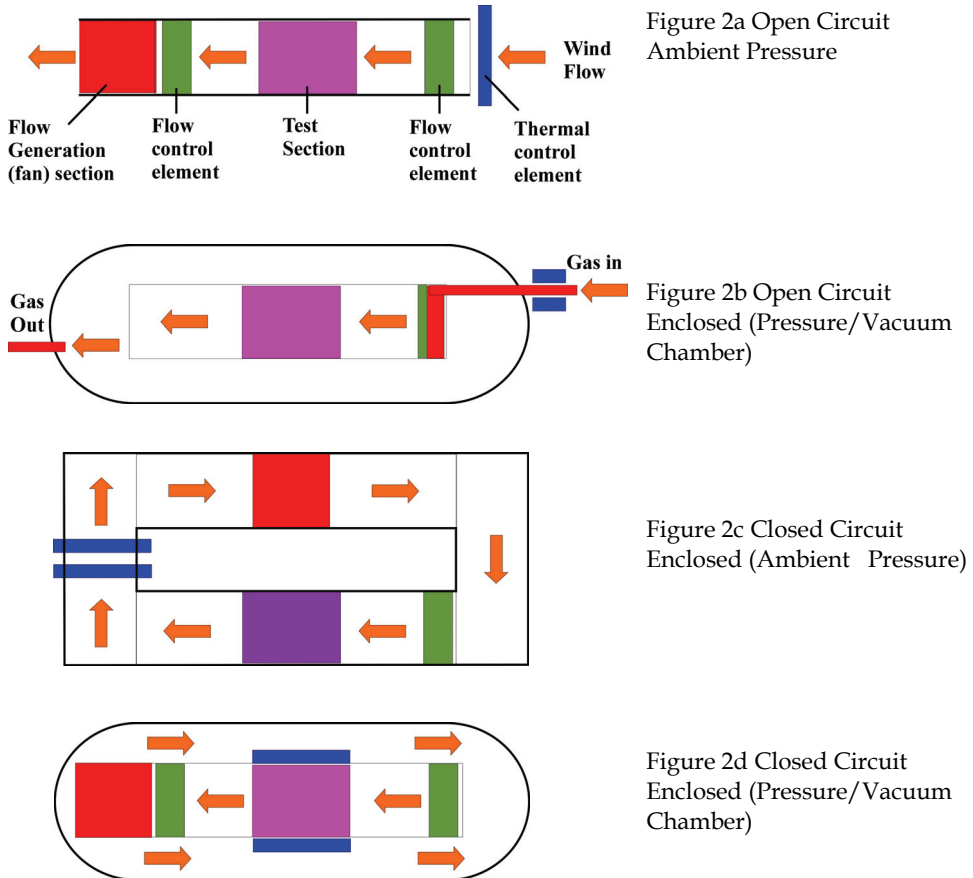


Fig. 2. Different types of Wind Tunnel geometry combining open/closed circuit designs and ambient or enclosed (environmental control).

In traditional ambient pressure wind tunnel facilities the choice of construction materials is largely unrestricted. Materials are therefore chosen dependent on mechanical properties (strength, weight, etc.) and possibly also cost and availability, wood for example is used in many wind tunnels. For environmental wind tunnels the choice of materials is generally far more restrictive since, to maintain low pressure or gas purity, materials with low out-gassing properties should be chosen and for temperature control the thermal properties and mechanical properties at low temperatures must be considered. The choice of materials subsequently affects the mechanical design of the wind tunnel structure.

External access to the wind tunnel (especially the test section) is also of great importance in most cases, both during operation and installation or maintenance. Here access includes, for

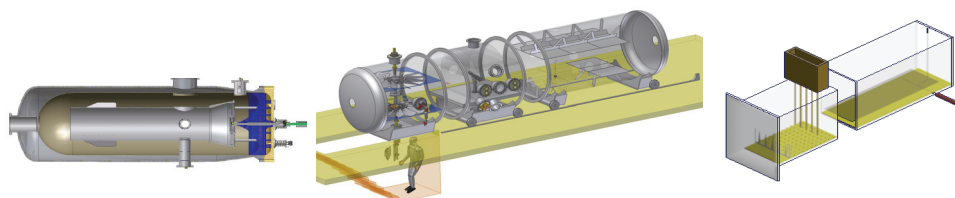


Fig. 3. Schematics of Left; Aarhus University Wind Tunnel I (AWTSI) design, Center; AWTS II design, Right; open circuit ambient showing upwind flow control (see flow control)

example mechanical, electrical and optical (visual) systems. Specifically mechanical access could involve being able to orientate a sample or sensor and therefore require rotation or translation mechanisms. Electrical access may be in the form of cabling for power and data transfer. Optical access could be cameras, lighting, spectrometers or other optical sensors. Ideally these forms of access should be as spatially close to the active section of the wind tunnel as possible and preferably large in cross section. For ideal flow (i.e. minimizing boundary effects) a wind tunnel should be cylindrical in cross section, however for the housing and access of samples/sensors, as well as many other practical applications of wind tunnels, it is desirable to use a rectangular cross section. This does not constitute a problem for most ambient-pressure applications; however for an enclosed (pressurized) wind tunnel this does present a technical challenge. The two environmental wind tunnel systems at Aarhus University apply two radically different geometrical solutions to this problem, with the AWTS-I system housing the cylindrical wind tunnel within its own (cylindrical) return flow, giving a rather attractive flow transport and uniform cross-section, though poor access to the test section and a non-optimal (circular) cross-section [Merrison et al. 2008]. The AWTS-II design conversely has an attractive, almost rectangular wind tunnel cross-section and good access to the test section, however the return flow is divided into two, above and below the test section, giving extremely non-ideal flow and constriction of the flow in the return section, which resulted in the need for extensive flow correction. At low pressure (below 100mbar) the highest wind speed achieved by AWTSI is around 15-20m/s, whereas AWTSII has achieved 20-25m/s, with similar degrees of (free flow) turbulence for both wind tunnels i.e. 5-20% increasing with wind speed.



Fig. 4. Photographs of the (10m long) AWTS-II facility showing the mobile environmental chamber sections, the central test section can be removed laterally.

In contrast to the Aarhus environmental wind tunnels the NASA Ames MARSWIT (Mars Surface Wind Tunnel, California USA) is an open-circuit, low pressure wind tunnel powered by a high pressure nozzle ejector system, the total length is 13m with a main test section of 1.2m by 0.9 m and is housed in a 4000 m³ low-pressure chamber which can operate at pressures down to ~3.8 mbar and wind speeds of 20m/s - 180m/s (at low

pressure) [White 1981, Greeley and Iversen 1985]. This system cannot be cooled and has been used for boundary layer studies.

For low pressure wind tunnel systems the structure of the vacuum chamber is one of the primary design features. This will typically require the use of a thick (bulky) steel shell and frame which, for mechanical strength, will optimally be cylindrical/spherical in form. This is similarly true for high pressure vessels. For open circuit environmental wind tunnels the limitations on the pressure vessel will limit the size and geometry of the test section. However for a re-circulating environmental wind tunnel the pressure vessel will even more strongly restrict design of the wind tunnel since, assuming the largest free flow cross section is desired then there must still be sufficient space for the return flow to be housed. It is desirable for this return flow cross section to be comparable to the test section cross section to avoid high turbulence and turbulent losses. The AWTS-II facility is one of the largest environmental wind tunnels with a cross section of around $2\text{m}\times 1\text{m}$ and a chamber volume of around 40m^3 , it is significantly larger than the almost 1m^3 volume and cross section of $0.4\text{m}\times 0.4\text{m}$ of the AWTS-I.

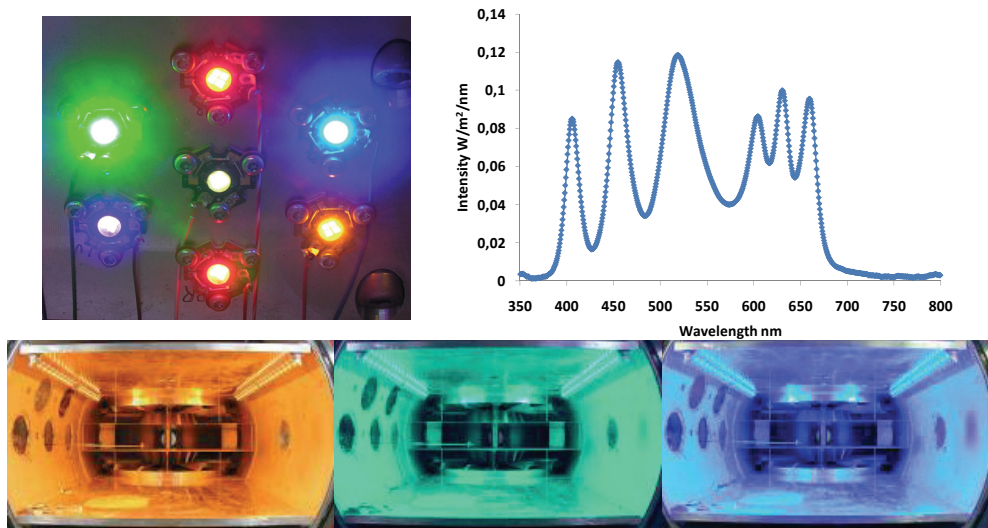


Fig. 5. A Light Emitting Diode based light source for solar simulation, illumination or crude spectroscopy in an environmental wind tunnel. Upper Left shows a photograph of a single array section including one of each of the seven different (wavelength) LEDs, Upper Right shows the irradiance measured within the wind tunnel (with all LEDs activated) showing the single wavelength components, the Lower photographs are taken inside the wind tunnel test section as different colored LED arrays are activated (red, green blue), the LED array strips are mounted in the upper two edges of this section.

In both industrial and scientific applications a common requirement is a light source which simulates the solar irradiance over a broad wavelength range. A problem with many light sources, for example halogen lamps and discharge lamps, is the generation of heat, both conductive and as thermal radiation (infra-red) which can make environmental temperature control difficult. Employing a light source outside the environmental chamber alleviates this

problem, however it then restricts the illumination of samples considerably. Compromise here will generally be necessary. An attractive option is the use of light emitting diodes (LEDs) which are efficient and monochromatic, being available as intense sources though generating relatively little heat. LEDs are low voltage making them technically easy to implement in most cases. With the use of arrays of variously colored LED the correct light irradiance can be achieved within broad optical wavelengths and even into the near infrared (more than 1000nm) and the Ultra Violet, with the latest UV LEDs below 250nm.

3. Flow control

Wind tunnels vary in their requirements for flow uniformity, while some are designed for low turbulence (close to laminar) flow, others apply techniques in order to reproduce particular boundary layer conditions (often referred to as boundary layer wind tunnels) whereas for some a specific free-flow degree of turbulence is required. In these differing cases it is probably fair to say that they are attempting to reproduce differing turbulence regimes present in nature and that it is therefore difficult to generalize about these wind flow designs. However it is worth discussing differing flow control techniques which are commonly employed and how specifically they can be applied.

Flow guides are smooth plates of differing geometry which are installed in order to steer the wind flow to obtain a desired wind pattern. For example they may be; curved in order to guide the flow around bends, they may be planar in order to straighten the flow or they may be used to partition the flow into sections in order to prevent unwanted lateral flow/eddies. In open circuit wind tunnels flow control should (obviously) be installed upwind. However, in a re-circulating wind tunnel they should generally be installed at the source of the unwanted flow pattern, which could be upwind or down wind. In the case of the European Mars Environmental Wind Tunnel (see figure 6) flow guides have been used to great effect at the entrance to the wind generating fans system and prevented extremely destructive back-flow caused by the rotation of the fan blades. Meshes are used to reduce turbulence in the wind flow and to obtain a more homogeneous flow profile, especially on scales larger than the mesh size which is typically of the order of 1mm. This is done at the expense of wind speed. Meshes are often utilized as a set of two separated by some mm-cm. In this case a pressure gradient is generated across the meshes, this helps to disrupt turbulence and non-uniformities in the flow. It should be noted that both flow guides and meshes while improving flow properties, will typically increase friction and therefore reduce the (net) wind flow for a particular wind generation power. The use of upwind roughness blocks and turbulence spires manipulate the vertical wind flow profile (at the test section) in order to emulate an infinite upwind 'fetch' i.e. to reproduce the surface boundary layer flow which would be produced if the wind tunnel were infinite in length. Clearly this is of great importance when studying boundary layer effects such as the entrainment and transport of sand or the flow patterns around a surface feature [Irwin 1981, Shao and Raupach 1992]. Expansion and compression stages can be used in wind tunnel design to increase wind speed, improve flow linearity and reduce turbulence. Here compression of the wind tunnel will increase the downwind flow speed and reduce the relative transverse turbulence. Clearly this is done at the cost of wind tunnel cross-sectional size and is not always possible to implement especially within a re-circulating wind tunnel. Often in open circuit wind tunnels and invariably in re-circulating systems wind generation is provided by a fan or fans. Fan design is in many cases non trivial, involving modeling and calculation regarding

the specific choice of fan blade size, number, form, angle and also motor power, torque and rotation rate. Such modeling and calculation can be aided by computational fluid dynamic calculations. Here one begins with the required parameters of wind speed (and ambient pressure), based on the wind tunnel design. The flow calculations will then predict a certain degree of frictional loss as a function of wind speed. The fan system can then be modeled as a system to generate a pressure gradient necessary to balance this frictional loss and maintain the desired flow rate. Given the flow rate and the required pressure differential a particular fan design can be chosen i.e. these are the required input parameters for the choice of fan design. In the case of environmental wind tunnels the choice of fan material must also be considered, for example to be compatible with out-gassing limits and low/high temperature.

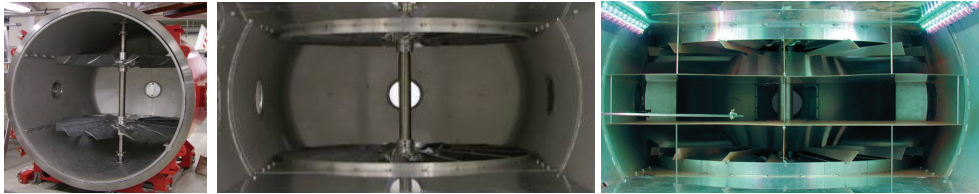


Fig. 6. Photographs into the flow generation section at the AWTS-II facility, Left shows the 1.8m diameter fans installed, Center shows with the upper and lower flow separators and Right the system of vertical and horizontal flow guides compartmentalizing the flow, preventing rotation and excessive turbulence.

Since almost all forms of high power motor are incompatible with the demands of (low) pressure and temperature within an environmental chamber, the drive mechanism for a fan system must be mounted externally. This presents a problem for the transfer of torque to the fan since passing a rapidly rotating axel through a pressure seal system is also incompatible with avoiding pressure leaks and maintaining low temperatures. A possible solution which has been employed in the various facilities at Aarhus University is the use of a magnetic coupling [Merrison et al. 2008]. Such couplings are commercially available and transfer torque from the drive axel (external) to the fan axel (internal) through a complex of magnetic fields generated by permanent magnets. This avoids physical contact of the two axels and allows this coupling to be completely hermetic (vacuum tight). A drawback with this system is the limited degree of torque which can be transferred by such couplings before they begin to slip which may limit the rotation rate (wind speed) within the wind tunnel. It does however have the benefit of protecting the drive-fan system from damage as slippage of this coupling is not hazardous.

A type of open circuit environmental chamber has been employed for Mars simulation conditions at Oxford University. Here gas is injected from an array of (relatively small) inlets into a flow volume which is continually being evacuated by a pump. In this case an extremely low turbulence flow can be achieved along with high flow speeds as well as cooling. A drawback can be that the flow rate is dependent upon the chamber pressure such that control of low flow speed involves inlet and pump rate control. Such a system can be well suited to anemometer calibration and high wind speed tests [Wilson et al. 2008]. Discussion here has focused on low wind speeds (subsonic flows). There are however, forms of wind tunnel which generate and utilize supersonic and even hyper sonic flows for various studies. Specific applications are in the design and testing of supersonic aircraft or

re-entry devices. It should be noted that such wind tunnels utilize specialized techniques and the flow in such high velocity regimes differs from that at wind speeds significantly below that of sound [Barlow 1999]. Generally environmental wind tunnels will involve compromising the 'ideal' wind flow characteristics due to geometric constraints imposed by the environmental chamber or environmental control systems, for example reduced cross section, increased turbulence, reduced maximum wind speed or the use of cumbersome flow control systems.

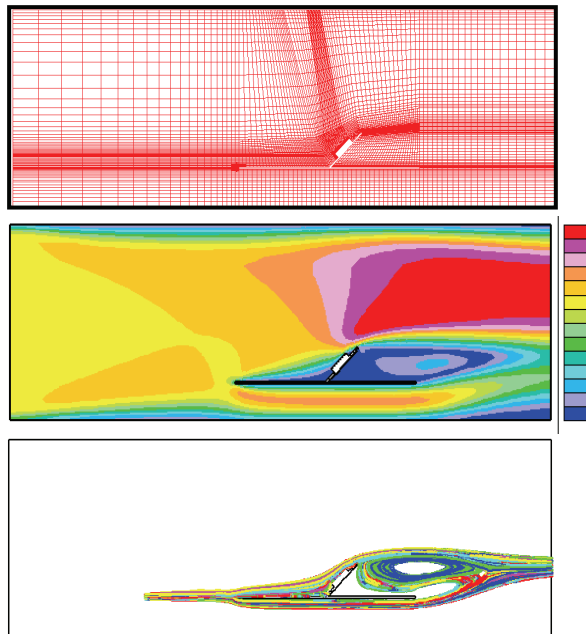


Fig. 7. Computational Fluid Dynamic calculations of an object within a wind tunnel showing: Upper; the finite element structure, Center; the calculated wind speed flow from red (high) to blue (low) and Lower; suspended (aerosol) particulates added to the flow and their trajectories traced.

4. Computational fluid dynamics

This chapter has focused upon experimental/laboratory studies using environmental wind tunnels, however discussion should be made of the use of computational fluid dynamic modeling in this regard as in some cases this may be an alternative to laboratory simulation. However in most cases these two techniques are complementary. When constructing a fluid dynamic model in order to perform computational flow analysis it is necessary to make simplifications and assumptions which in most cases must be verified experimentally in order for confidence to be placed on the results [Peric et al. 1999]. A specific example is the calculation of flow around an irregular shaped object. In this case it is necessary to construct a finite element representation of this geometry before inputting wind flow boundary conditions. Although the resolution of this finite element array can be increased in order to

ascertain convergence, this will also be limited by computing power. Here comparison with experiment can be of great benefit in identifying sources of high sensitivity in the flow such that resolution be enhanced in this volume (see figure 7). A combination of targeted laboratory measurements and computational analysis can be ideal in simulating complex and difficult flow problems [Kinch et al. 2005]. Typically CFD is employed in the design phase of wind tunnels, though often the flow is complex and multi-dimensional such that empirical measurement and the implementation of correction elements is necessary to arrive at the most satisfactory flow characteristics.

5. Environmental sensing technology

A crucial aspect to any application of wind tunnels and/or environmental simulators is the use of accurate and reliable sensor systems for control and reproducibility of the simulated conditions. Some sensor systems are readily and commercially available at a well evolved level, for example for temperature and pressure. Other sensor systems can be complex, expensive and require adaptation, examples are wind sensors (anemometers) and gas composition. For some sensor systems there is a clear demand for new technology, yet this technology awaits development, examples are shear stress sensing and aerosol analysis.

In *temperature* sensing thermo-resistors are widely available (for example 100 Ohm platinum resistors i.e. Pt100), these are typically inexpensive and are accurate (typically around 1°C) over a wide range. The same could also be said of thermocouples (e.g. K-type), though these generally have a limited low temperature range. Thermocouples can also be difficult to integrate into an environmental chamber due to the need to maintain the contact potential i.e. maintain the exotic metal cables. *Pressure* sensor systems are available either for high pressure use, low pressures or specific to terrestrial conditions, i.e. limited to around 1 bar. Low pressure sensors are typically (generically) referred to as vacuum gauges. A type of vacuum gauge which is ideal for moderate low pressures (down to say 0.1mbar) and which is accurate even in differing gas compositions is the capacitance vacuum sensor, it is therefore well suited to study of Earth's upper atmosphere or Mars. Such capacitor based techniques are also useful for determining pressure differentials which can be important in wind tunnel design or wind sensing (see Pitot tube). Although absolute humidity (water vapor pressure) sensors are typically complex and expensive, relative humidity sensors are often extremely compact and operate over wide temperature and pressure ranges. Specifically thin polymer film type sensors are commercially available and are easily implemented into an environmental system (e.g. Honeywell HHH series).

In environmental systems where the *atmospheric composition* may be controlled it is important to be able to monitor it. There are few available options in this case and typically a sensor system called a Rest Gas Analyzer is used. These are often a type of quadrapole (radio frequency) mass spectrometer. They operate by ionizing the gas at low pressure (i.e. leaked through a valve) and extracting the ion fragments individually to determine their mass to charge ratio. It may then be possible to re-construct the original molecular structure of the gas, it is however difficult if the atmosphere contains several species where some fragments are ambiguous and it is often difficult to precisely determine abundances without careful control/calibration of the system and some expertise. Although these systems are relatively expensive and cumbersome to install, there is at present a lack of viable alternatives.

Finally in any application where an array of sensory systems is used, it is desirable to implement a data-logging system which records the various sensor outputs during

measurement cycles. For environmental wind tunnel systems it is also natural then to integrate this data logging capability into a computer system which also interfaces (and records) some of the control parameters of the facility such as wind generation (driving fan rotation rate), vacuum/pressure control system (pumps, valves etc.), cooling/heating systems or lighting subsystems. Although this constitutes an added level of complexity it allows for a higher level of reproducibility, sensor correlation and possibly safety.

6. Flow sensing technology

Clearly of primary importance with regard to wind tunnels is the accurate sensing of wind flow (Anemometry). There is a wide variety of available anemometer techniques, some dating back over 500 years, others are still being developed. These wind sensing systems vary in accuracy, complexity, price, size, and so on. In the following paragraphs some of the most common wind sensing technologies will be presented and briefly discussed, specifically with respect to their application in wind tunnels.



Fig. 8. Photographs of Laser Anemometers (acting also as suspended dust sensors), Left prototype time of flight instrument, Center the sensor during aerosol testing in an environmental wind tunnel, Right A commercial Laser Doppler Anemometer operating through an environmental wind tunnel access window, note the beams illuminating the suspended dust in the flow.

6.1 Laser anemometers

These are probably the most advanced and desirable type of wind sensor which have been applied in wind tunnels, specifically the Laser Doppler Anemometer (LDA) is used extensively. Several more recent variations on this instrument can measure in multiple dimensions, image and determine suspended grain size. This technique has the benefit of being non contact, such that it is independent of the environmental conditions within the flow (pressure, temperature, composition, etc.), it is also accurate and does not normally require external calibration. In fact LDA based systems are widely used in wind tunnel applications for the calibration of other types of wind sensor. The principle behind the technique is the scattering and detection of light by suspended aerosol particles, by measuring the frequency shift due to the velocity induced Doppler effect. More specifically two (or more) beams are used to produce an interference pattern, measurement of the shift in this pattern allows single velocity components of the grains to be determined. The system does have the disadvantage of requiring the presence of suspended particulates within the flow, which are introduced as smoke in many systems. However, for systems studying aerosols this is a major advantage since the suspended grain concentration can be quantified using this technique. Typically LDA systems are expensive and bulky, though can use

optical fibers and therefore achieve a relatively compact sensing head. Miniature (even micro-scale) laser based wind sensors are being developed, though have yet to advance from prototyping. One such system is based on a time of flight principle in which a light pattern is generated within the sensing volume. Single suspended aerosol particulates traversing this light pattern will scatter light with a modulated signal from which its velocity can be established, specifically in the case of the prototype shown in figure 8 a three line light pattern is used and the scattered light signal will consist of three pulses the time separation is then directly related to the velocity [Merrison et al. 2004, Merrison et al. 2006]. This type of technology has the potential to become miniaturized (on the sub-cm scale) and have low power consumption as well as being robust. Although limited in precision compared to LDA systems, it may be applied in systems too small or inaccessible for larger sensors and provide an affordable (and portable/battery driven) aerosol sensor. The current advancements in solid state laser and other optoelectronic technology give sensors of this kind a promising future.

6.2 Mechanical (cup anemometers or wind socks)

Mechanical anemometers are by the far the oldest, simplest, most common and varied form of wind sensor. Most widely used are cup anemometers and forms of wind sock or wind vane. A cup anemometer consists typically of conical cups mounted on a axel such that wind drag causes rotational motion which can be sensed by a tachometer in order to relate the rotation rate to the wind speed. Wind vanes and socks are typically more primitive and consist of a structure (tube/sock or plate) which is deflected by the wind such that the deflection angle is a measure of the wind speed and the direction may often be seen in the direction of the deflection. Such mechanical wind sensors are rarely used in wind tunnel applications due to their poor accuracy/precision and often limited dynamic range. They are however an invariable component of weather/climatic stations on Earth and have even been adapted for the extreme environment of Mars and Venus. Such systems can potentially be extremely compact, light weight, sensitive and robust given careful design and testing [Gunnlaugsson et al. 2008].

6.3 Hot wire or hot film

These sensors have been used extensively in wind tunnel experiments over several decades. They are typically accurate and sensitive in terrestrial conditions, they can also be multi dimensional and have reasonably fast response times. Compared to mechanical wind sensing techniques they therefore provide improvement in precision. The measurement technique relies on (electrically) heating a thin wire or foil which is then cooled by the flow of air. The cooling rate is therefore related to the wind speed. There are many variations on the this concept including specialized geometries, multiple heated elements (to determine wind direction), pulsed operation and heater-sensor feedback circuitry. Challenges to this technique are thermal (conductive) losses and temperature dependences in addition to the sensitivity to atmospheric properties. Also the heated sensors are often physically fragile and poorly suited to harsh environments. However it has been demonstrated that careful design, testing and importantly calibration can allow these sensors to be used even in low pressure, thermally unstable environments such as Mars. The first successful wind sensor system developed by NASA was such a hot film anemometer.

6.4 Pitot tubes

Pitot tubes are a simple and widely applied wind velocity sensor. This type of sensor is used in the aerospace industry (airplanes) as well as wind tunnels. The principle is measuring the overpressure generated in a wind facing tube compared to a non wind facing aperture. This pressure differential is a function of the wind speed relative to the tube. It is therefore well suited to situations where the direction of the wind flow is known. Despite their wide use, the Pitot tube is typically limited in range (due to its strong dependence upon wind speed) and requires careful calibration, since it is dependent upon atmospheric conditions (pressure, temperature, etc.).

6.5 Sonic anemometers

Sonic anemometers are a relatively modern and commercially available sensor for determining wind flow, they utilize the transmission of high frequency sound (ultrasonic) in order to measure wind flow by determining the acoustic propagation speed. Sonic anemometers can simultaneously measure wind velocity in all three dimensions and at high sampling rate. These sensors are precise and being three dimensional are capable of quantifying vertical as well as lateral flow rates. This makes them the instrument of choice for the study of boundary layer transport. They are currently used widely in climatic/atmospheric studies, though not usually in wind tunnel applications. Unfortunately sonic anemometers are sensitive to the physical properties of the atmosphere (composition, pressure, temperature, humidity etc.). This makes them poorly suited to many environmental applications. Research groups have attempted to adapt sonic anemometers to extreme environments such as that on Mars, though have been hindered by the low pressure.

6.6 Shear stress

The quantification of surface shear stress within a wind tunnel is crucially important when trying to evaluate the threshold or transport rates of granular material or more generally mass transport rates or heat transfer. Currently a large body of semi-empirical work allows the measurement of surface wind velocity to be related to the surface shear stress (friction velocity). More crudely measurement of the wind velocity, turbulence and surface roughness can be used to obtain estimates of shear stress [White 1991]. However experimentally these are often difficult and indirect approaches to the determination of surface shear stress. Ideally the application of nano-micro scale force/pressure sensors could now allow the direct measurement of wind shear stress [Xu et al 2003], however these are not commercially available and have not advanced from research prototypes.

7. Thermal control

Most of the discussion here will concern cooling within environmental wind tunnels rather than heating, though in many respects the problems and solutions are essentially the same. In industry environmental wind tunnels typically refer to wind tunnels within which the temperature can be controlled, with heating and cooling over the range typically expected on earth i.e. around -60°C to $+50^{\circ}\text{C}$, though with no control of pressure. Such wind tunnels are used extensively in the automobile and aerospace industries and are often on a scale (many square meters cross section) such that full size vehicles can be housed. In this case commercial refrigeration (freezer) technology can be employed. Cooling systems vary depending on the temperature range and power requirements, typically for temperatures

above -80°C closed cycle refrigeration (using refrigerants such as haloalkanes, ammonia, alcohol, etc.) can be used. Below this and down to around -190°C it is common to use liquid nitrogen flow through systems of some kind, since this is readily available and relatively cheap [Jensen et al. 2008]. Cryogenic pumps (e.g. closed cycle helium refrigeration systems) are used for very low temperatures (a few K) or smaller systems which operate for long periods of time and require stability. A convenient cooling or rather heat exchange system is the Peltier element. This is a low voltage DC driven thermo-electric device for generating a temperature gradient across thin plate type bimetallic networks. Thermal power exchange of the order of 100W and temperature gradients of the order of 70°C (from room temperature) are typical. These are easily installed and relatively cheap and often used for thermal control of small detectors, solid state lasers, etc. A limitation is that they operate poorly at low temperature with a decrease in operating voltage (power) and temperature gradient, for example at around -130°C the maximum temperature gradient possible falls to around 10°C . In the case of heating systems, although electrical heaters are commonly available and a well established technology, their use in an environmental simulator imposes certain restrictions on the applicable materials and geometry, for example that the material should not outgas, should be compatible with cryogenic temperatures, be fully electrically encapsulated and available in various geometries depending on the wind tunnel structure. A commercially available solution which has many of these qualities are custom manufactured encapsulated heater mats (X-Mat®) they consist of copper conductors encased in Capton foil (3 mm thick) with silicone encased cables.

In addition to an effective cooling/heating system there is the need for efficient transport of thermal power to the sample or test section from the cooling system and possibly also to the ambient wind tunnel gas. Similarly there will be the desire to prevent thermal transport to the sample/test section from external sources or even heating due to power generated by electrical systems. Thermal transport is therefore of importance and an understanding of it necessary. Three thermal transport processes are relevant in wind tunnel and environmental chamber design. Conductive thermal transport is generally of most importance and the method by which most thermal control can be achieved. Specifically, metals with high thermal conductivity are used, such as copper or aluminum. When dealing with fluids (such as gas) thermal transport can also occur by convective transport, here thermal power is transported by the physical flow of mass. This must be considered even when dealing with low pressure gases (a few mbar) since thermal conductivity is not strongly dependent upon pressure/mass density and is therefore still significant at low pressure. An added complication is the possibility for volatiles, such as water, to condense/freeze, evaporate and transfer heat through this mechanism. Radiative thermal transport i.e. the transport of heat through light emission/absorption (typically at infrared wavelengths) is significant even in the absence of fluid/solid contact. It can be of comparable importance in the thermal balance of samples or gas within the wind tunnel. Manipulation of this effect can be achieved by alteration of the surface properties of materials within the environmental chamber for example with the use of coatings (paints).

For extreme temperatures (especially cryogenic) environmental chambers are necessarily going to have to employ some form of thermal insulation, preferably with good efficiency such that there is as little thermal contact (loss) between the test section and the ambient environment as possible. There are many types of ambient pressure insulation material available, varying in insulation efficiency, price, mass, volume etc. For low pressure systems the use of double walled (vacuum) insulation techniques (such as that used in Dewar flasks)

is effective and widely applied, however this technique essentially requires two nested vacuum systems and is therefore generally expensive and complex to construct. Efficient vacuum compatible thermal (cryogenic) insulation is available. One example is multi-layer thin film super-insulation developed at CERN-CryoLab and commercially available (JEHIER). Despite its high price relative to ambient pressure insulation, it is simple to apply multilayer super insulation within an environmental chamber design, it is also reasonably efficient and affordable compared to a multi-walled vacuum insulation solution.

In a closed circuit systems the frictional loss of power within wind tunnel can cause significant heating at elevated wind speeds (of the order $100\text{W}/\text{m}^3$). This can become problematic for thermal control systems in such situations. Specifically heating of the gas will ensue and heat deposition on surfaces in contact with the gas. This must be considered when designing thermal control systems if stable temperatures are to be achieved.

As mentioned previously with respect to sensors, in addition to a thermal sensor system and a cooling/heating system an automated (intelligent) control network needs to support these sub-systems in order to achieve effective thermal control. In many research and industrial applications it is necessary to perform complex *thermal cycling*. Such cycling may involve specific thermal ramp rates and extend over long periods of time (days) necessitating computer control.

Even in a thermally controlled system where effective thermal insulation has been employed, effective thermal conduction to the sample has been used and sufficient heat is exchanged, this does not ensure thermal stability since typically the cooling system will not be continuously in operation and will have a certain time delay between activation and the onset of cooling. In practice therefore thermal control will consist of a feedback system of thermal sensors and thermal control which will introduce oscillation of the test section temperature. Additionally ensuring thermal stability may not ensure thermal uniformity as the application of cooling may not be physically at the same location as the source of heating or thermal loss which therefore leads to spatial temperature gradients. An obvious method to both stabilize the test section (or sample) temperature and achieve improved thermal uniformity is the use of a massive conductive (metal) test section element or sample mounting section. Here the thermal inertia of the mass achieves thermal stability and the high thermal conductivity of the mass ensures uniformity. It is however often difficult to find space to house such a massive element and the cooling/heating time of this element will necessarily be long. In the case of the AWTSI and AWTSII facilities a compromise has been reached between the desired stability/uniformity and the available space/required response time. In the case of the AWTS-II facility at a temperature of around -120°C the uniformity of the test region is around $15^\circ\text{C}/\text{m}$ and the stability is around $\pm 2^\circ\text{C}$ despite the use of a 0.1m thick sample (aluminum) mounting plate.

8. Ice formation and sensing

The transport of water vapor is often an important physical parameter for environmental simulators, both with regard to industrial and research applications. For example on Mars the desiccation of surface materials and subsequent frost formation (re-hydration) may lead to geophysical changes in the surface materials, specifically salt crust formation (which are widely observed) or even erosion. Similarly man made materials can be susceptible to weathering by the transport of water vapor from the surface. For the control of humidity at low temperatures it is necessary to both cool the sample and another element within the

environment. Typical research environmental chambers rely only on mounting the sample on a cold finger, in this case the sample will typically be at the lowest temperature within the environment and therefore attract out gassed water vapor and be hydrated (often forming surface ice). Other environmental chambers either cool the outer chamber or the atmosphere directly. In this case the sample will typically be warm compared to this environment and lose water vapor i.e. become desiccated. If the sample and environmental element(s) are thermally controlled independently then water diffusion to and from the sample can be regulated allowing detailed study of water transport phenomena. This does however require more sophisticated cooling and (computer) control systems. It is also then additionally desirable to have both cooling and heating systems for enhanced thermal regulation. Environmental (cooled) wind tunnels have been used occasionally in studies of snow transport, often involving processes of electrification which is relevant to the generation of electrical thunder storms and lightening [Maeno 1985, Schmidt et al. 1999]. This field of research is sparsely investigated and still largely empirical, despite being of great importance to human safety (anywhere that people interact with snow and ice) and relevant to understanding a variety of (dangerous) meteorological phenomena including the vast Arctic/Antarctic regions. The technology for such research is readily available and straightforward to implement, involving the combination of a wind tunnel structure and (sub-zero) refrigeration techniques.

9. Aeolian sand and dust transport

Desertification involves the erosion and degradation of drylands which affects 25% of the Earth's landmass and more than 2.1 billion people. Each year 12 million hectares of land are lost to desertification. This is the UN launched decade for deserts and the fight against desertification. The relevance of this work into Aeolian grain transport is to understand, predict and control this environmental effect [Ofori and Showstack 2010]. As well as being affected by the climate (and climate change) through changes in wind and surface conditions, Aeolian transport can also strongly affect the climate through the generation of aerosols (e.g. suspended dust). As an example, every year of the order of 1 billion tons of dust is removed from north Africa into the atmosphere and is carried great distances, around 200 million tons is subsequently deposited on south America. The affect of such aerosols in the atmosphere, also including smoke, clouds, ash etc., is complex. There is the need for a lot more research to understand the role of aerosols, including laboratory studies (environmental wind tunnel studies), remote and in-situ sensing as well as modeling.

The definition of sand in the context of wind tunnel operation is granular material which cannot be suspended by the flow, but can be entrained i.e. can be removed from the surface by the wind shear. The definition of dust in this regard is therefore granular material which is fine enough to be suspended. Typically in nature sand particles will be transported by **saltation** wherein they are repetitively removed (entrained) from the surface, but cannot remain suspended and return to the surface in a ballistic impact referred to as a splash [Pye and Tsoar 1990]. This definition of sand and dust is not a strict size/mass scale since it is dependent upon many physical parameters for example; the wind shear, atmospheric properties, gravitational conditions, etc. Under terrestrial conditions sand is typically greater than around 60 μ m up to mm size. Particulates larger/more massive than this can be moved by wind shear without leaving the surface either by rolling, sliding or by impact of sand, this transport process is referred to as creep.

Saltation is an effective erosion process due to the destructive nature of the splash. These impacts typically lead to chipping and the generation of dust sized particulates. Aeolian (wind driven) particulate transport is also effective at sorting granular material, specifically separating sand, dust and stones/pebbles. This leads to the generation of the many sand dune forms observed, their character depending on the nature of the wind flow. The threshold wind conditions (surface wind shear) required for sand saltation transport has been widely studied, both in wind tunnel simulators and in nature following the pioneering work of Bagnold [Owen 1964, Greeley and Iversen 1985]. Despite this the work remains semi-empirical, mainly due to the complexity of the physical parameters involved, such as; wind induced lift and torque, adhesion, gravitation and the effect of splash. Similarly a large body of work exists in which the transport rate (above threshold) has been studied. Again resulting in an array of increasingly sophisticated and intricate semi-empirical expressions with especially the effect of splash being problematic [Shao and Raupach 1992, Rasmussen and Sorensen 2008]. Interesting aspects to be noted is that the rate of sand transport increases rapidly above the threshold wind speed (varying as the cube of the wind speed) and that due to the effect of splash saltation can be maintained below (by around 20%) the initial threshold speed once the process has begun.

As discussed in the introduction the different gravity on other planets is problematic to reproduce in terrestrial laboratories. However, it is possible to vary the effective mass density either by using low density material or hollow structures (glass bubbles), this has been effectively utilized in wind detachment studies. Unfortunately a complex process such as the splash in saltation involves both the inertial mass (on impact) and the gravitational mass (during the trajectory) of the sand particulates. This makes this process impossible to entirely reproduce in a terrestrial laboratory and can probably only be studied through partial experimental simulation, modeling and observation in the respective gravitational field [Merrison et al. 2007].

Wind tunnels involved in sand transport are typically of the order of a square meter cross section, several meters long and are constructed as boundary layer simulators with the use of (upstream) flow control to reproduce the correct surface boundary layer (and shear stress) [Young 1989]. These flow control units include roughness arrays, inlet meshes, turbulence spires, and systems for injecting sand upstream (see figure 3). The results of laboratory based wind tunnels can be complemented by the use of field wind tunnels. These are portable wind tunnels which are taken into the field and thereby use real surface material and environments and possibly even the actual wind flow.

Dust can be entrained and therefore transported by wind shear in two ways. The generally accepted process of dust entrainment on Earth is through the action of saltating sand grains impacting dust particulates and ejecting them into suspension. This process is extremely effective at wind speeds above the threshold for saltation. The entrainment of single (e.g. micron sized) dust grains directly by wind shear requires extremely high shear stress (extremely large wind speeds), however dust grains generally cohere and form larger aggregates, often up to mm sized. The mass density of these aggregates can be low (below 1 g/cm^3) and can therefore be mobilized at much lower wind stress than solid sand grains. Once detached from the surface the dust aggregates may disintegrate and liberate free dust grains into suspension. This process has been observed and quantified in (environmental) wind tunnel studies and helps to explain the otherwise paradoxical observation of dust transport in the Martian atmosphere (at wind stress below the sand transport threshold) [Merrison et al. 2007]. This transport mechanism may also be important for dust transport in areas not rich in sand, though dusty.

An interesting erosion effect which has emerged as a result of studies in a Mars simulation wind tunnel is the possibility that saltation may also lead to alteration in mineralogy and thereby not just the generation of dust, but also for example oxidation. This may explain the presence of the reddish iron oxide giving Mars its distinctive hue. On earth mineral change due to presence of liquid water and high atmospheric oxygen content probably makes such erosion induced mineral change only a minor and not easily identified process, though may also have importance through the chemical reactivity of the erosion generated dust. The mineral change appears to occur through mechanical activation of freshly cleaved surfaces, for example in the case of silicate leading to an oxidizing surface which may be hazardous to organic material [Merrison et al. 2010]. This phenomenon is as yet poorly researched and requires the further application of laboratory simulation.

10. Aerosol formation and sensing

Open circuit wind tunnels are poorly suited to studies of suspended particulates, i.e. aerosols, due to problems of contaminating the environment with the aerosol particulates and also since the aerosols only perform a single pass through the detection volume. This limits the type of aerosol dynamics which can be studied, for example investigating their temporal evolution would not be possible. In a re-circulating wind tunnel the aerosol can be confined and studied for long periods of time, limited only by loss due to settling and adhesion [Merrison et al. 2002, Merrison et al. 2008].

As discussed previously fine solid particulates (i.e. dust grains) generally tend to cohere and are found as large aggregates. In order to inject dust particulates into suspension these aggregates must be dispersed. A problem affecting many dust injection systems (aerosolizers) is that of blockages caused by dust aggregation (clumping). A system which functions well and is widely used in the medical industry for dry powder aerosol dispersion, is the use of a gas jet. When merged with the dust material, the process of gas expansion (usually from a nozzle) disperses and separates the aggregates. This same technique has been successfully employed in planetary aerosol simulation where (relatively) high pressure gas is passed through a chamber containing the dust material and subsequently expands at high velocity into the wind tunnel flow. This system of gas injection is also successfully applied in the case of liquid (droplet) aerosols. Liquid aerosols are commonly used in pharmaceutical applications, for example inhalers and the many types of commercial 'aerosol cans'. Another method for entrainment (suspension) which resembles that seen in nature, involves emplacing a thick dust layer in the wind tunnel and increasing the wind speed briefly in order to suspend it. Aerosols may also be formed as a result of condensation/precipitation from the gas phase. In this case a system of vapor injection from an external source may be utilized. Alternatively the vapor source could be internal to the system and be generated by heating to generate sublimation/boiling. This may be especially effective if the process of condensation (or nucleation) is to be studied. Surprisingly there is still a great deal yet to be understood about the properties of ice/water aerosols (e.g. clouds and snow). For example; the electrification process or processes which are responsible for generating lightning, the details of nucleation (for example by dust, radiation or ions), the micro/nano structure and adhesive/cohesive properties. It seems likely that this will be an active research field in the near future and that this will involve the construction of new low temperature environmental simulators, possible including re-circulating wind tunnel systems.

Particulate deposition from suspension is of great importance with regard to the climate as well as being a hazard to instrumentation, machinery and human health. Lacking commercial instrumentation to quantify this deposition process, a prototype optoelectronic instrument has been developed to determine the deposition rate of particulates [Merrison 2006]. This instrument also employs electrodes to generate electric fields and thereby attract electrified aerosol particulates. This method of determining the electrical charge (and sign) of suspended particulates could be of great use in industries dealing with aerosols. Electrostatic fields are already used routinely in industrial applications to remove or control particulates both in suspension and otherwise. Granular electrification is a ubiquitous effect and must be considered wherever granular material is found [Rasmussen et al. 2009]. In the case of dust particles electrification leads to the formation of aggregates which is key to the process of entrainment at low wind speeds (in the absence of saltating sand) [Merrison 2004a].

On earth aerosols may include (or consist) of biological material or micro organisms (such as pollen, virus, bacteria, spores, etc.). Bio-aerosols of this kind are clearly of great environmental interest with regard to health and ecology. It would be of much interest to study bio-aerosols and their production/transport mechanisms in a controlled environmental wind tunnel. Although such research is not currently active, there are plans to begin studies of this kind with relation to planetary protection (i.e. the protection of other planets from terrestrial micro organisms) by the space agencies NASA and ESA.

11. Acknowledgements

The author would like to thank Keld Rømer Rasmussen for fruitful discussions over the years and for financial support, ESA (Contract No. 21285/08/NL/GLC), EU Europlanets network (FP7) Trans-National Access (EC Grant agreement no 228319) and the Villum Kahn Rasmussen fund.

12. References

- Bagnold, R.A., 1941. *The Physics of Blown Sand and Desert Dunes*. Methuen, London
- Barlow, J.B., 1999. *Low-speed wind tunnel testing*. Wiley, New York.
- Fay, J.A. and Sonwalkar, N., 1991. "Fluid Mechanics", MIT, Boston.
- Greeley, R., Iversen, J.D., 1985. "Wind as a Geological Process on Earth, Mars and Venus." (Cambridge Planetary Science Series). Cambridge University Press, Cambridge.
- Gunnlaugsson, H.P., Holstein-Rathlou, C., Merrison, J.P., Knak Jensen, S., Lange, C.F., Larsen, S.E., Madsen, M.B., Nørnberg, P., Bechtold, H., Hald, E., Iversen, J.J., Lange, P., Lykkegaard, F., Rander, F., Renno, N., Taylor, P., Smith, P., 2008, "The Telltale Wind indicator for the Mars Phoenix Lander", *J. Geophys. Res.*, 113, E00A04,
- Hall, D. J. *Fluid. Mech.* 1988, 187, 451-466
- Irwin, H.P.A.H., 1981. "The design of spires for wind simulation". *Journal of Wind Engineering and Industrial Aerodynamics* 7, 361-366.
- Kinch, K. M. Merrison, J.P., Gunnlaugsson, H. P., Bertelsen, P. Madsen, M. B., Nørnberg, P. 2005, "Preliminary analysis of the MER magnetic properties experiment using a CFD model.", *Planet. Space. Sci.*, 54, 28-44.
- Jensen, L.L., Merrison, J., Hansen, A.A., Mikkelsen, K.A., Kristoffersen, T., Nørnberg, P., Lomstein, B.A. and Finster, K., 2008, "A facility for long-term Mars simulation experiments: the Mars Environmental Simulation Chamber (MESCH).", *Astrobiology*, 8, 537

- Merrison, J.P.; Bertelsen, P.; Frandsen, C.; Gunnlaugsson, H.P.; Knudsen, J.M.; Lunt, S.; Madsen, M.B., Mossin, L.A.; Nielsen, J.; Nørnberg, P.; Rasmussen, K.R. and Uggerhøj, E. J., 2002, *Geophys. Res. Planets*, 107, 5133-5141
- Maeno, N., Naruse, R., Nishimura, K., Takei, I., Ebinuma, T., Kobayashi, S., Nishimura, H., Kaneda, Y. and Ishida, T., 1985, "Wind-tunnel experiment on blowing snow.", *Ann. Glaciol.*, 6, 63-67.
- Merrison, J.; Jensen, J.; Kinch, K.; Mugford, R.; Nørnberg, P., 2004a, "The electrical properties of Mars analogue dust.", *Planetary and Space Science*; 52: 279-290
- Merrison, J.P.; Gunnlaugsson, H.P.; Jensen, J.; Kinch, K.; Nørnberg, P.; Rasmussen, K.R.: 2004b, "A Miniature Laser Anemometer for Measurement of wind speed and dust suspension on Mars", *Planetary and Space Science*; 52(13): 1177-1186
- Merrison, J.P., Gunnlaugsson, H.P., Kinch, K., Jacobsen, T.L., Jensen, A.E., Nørnberg, P., Wahlgreen, H., 2006, "An integrated laser anemometer and dust accumulator for studying wind induced transport on Mars", *Planet. Space. Sci.* 54, 1065-1072
- Merrison, J.P., Gunnlaugsson, H.P., Nørnberg, P., Jensen, A.E., Rasmussen, K.R., 2007, "Determination of the Wind Induced Detachment Threshold for Granular Material on Mars using Wind Tunnel Simulations.", *Icarus*, 191, 568-580
- Merrison, J.P., Bechtold, H., Gunnlaugsson, H., Jensen, A., Kinch, K., Nørnberg, P. and Rasmussen, K., 2008 "An Environmental Simulation Wind Tunnel for Studying Aeolian Transport on Mars", *Planet. Space. Sci.*, 56, 426-437
- Merrison, J.P., Gunnlaugsson, H.P., Jensen, S.J.K., Nørnberg, P., 2010 "Mineral alteration induced by sand transport; a source for the reddish colour of Martian dust.", *Icarus*, 205, 716
- Mollinger, A.M.; Nieuwstadt, F.T.M., 1996, *J. Fluid. Mech.* 316, 285-306
- Monin, A.S.; Yaglom, A.M.; *Statistical Fluid Mechanics: Mechanics of Turbulence Volume 1*, MIT Press, (1973)
- Ofori, L., and Showstack, R., 2010, "Desertification awareness decade", *EOS Transactions AGU*, 91, p. 327
- Owen, P.R., 1964. "Saltation of uniform grains in air.", *Journal of Fluid Mechanics* 20, 225-242.
- Peric, M.; Ferziger, J.H. *Computational Methods for Fluid Dynamics*, Springer, 2 Ed., 1999
- Pye, K.; Tsoar, H. *Aeolian Sand and Sand Dunes*, Unwin Hymann Ltd, 1990
- Rasmussen, K.R., Sorensen, M., 2008, "Vertical variation of particle speed and flux density in Aeolian saltation measurement and modeling", *J. Geophys. Res. Earth Surface* 113(F2), F02S12.
- Rasmussen, K.R., Kok, J.F., Merrison, J.P., 2009, "Enhancement in wind driven sand transport by electric fields", *Planetary and Space Science*, 57, 804-808
- Shao, Y., Raupach, M.R., 1992. "The overshoot and equilibrium of saltation.", *Journal of Geophysical Research* 97 (D18), 20559-20564.
- Schmidt, D.S., Schmidt, R.A., Dent, J.D., 1999. Electrostatic force in blowing snow. *Boundary-Layer Meteorology* 93 (1), 29-45.
- White, B.R.; *J. Fluids Engineering* 1981, 103, 624-630
- White, F.M., 1991. *Viscous Fluid Flow*. McGraw-Hill, New York
- Wilson, C. F., Camilletti, A. L, Calcutt, S. B., Ligrani, P. M., 2008, "A wind tunnel for the calibration of Mars wind sensors", *Planetary and Space Science*, 56, 1532-1541
- Xu, Y. Jiang, F., Newbern S., Huang A., Ho C., Tai Y., 2003, "Flexible shear-stress sensor skin and its application to unmanned aerial vehicles," *Sensors and Actuators A: Physical*, vol. 105, pp. 321-329
- Young, A. D., 1989. *Boundary Layers* 1st 413 edition. BSP Professional Books.

Dynamically Improved 6-DOF System for Measurements of Forces and Torques in Wind Tunnels

V. Portman, B. Sandler and V. Chapsky
*Ben Gurion University of the Negev,
ISRAEL*

1. Introduction

Investigation of bodies liable to high speed or variable airflows is a subject of importance. Determination of force and torque vectors acting on the latter is necessary to establish strength of the body and flow behavior. Airflow influence on a body (or system of bodies) is used in science and industry to define the values of air resistance parameters acting on this body. Resisting forces and torques, lifting or carrying forces and torques, and air attacking angles are examples of such types of parameters. This work deals 6-DOF force and torque measuring suited for use in air tunnels, comparing it with the existing methods used for the same purpose. Except for the body under investigation and its fastening elements nothing else is placed inside the tunnel. Six force sensors (load cells) and their fastening design is organized outside the air tunnel by means of a metal cubic (or other) frame were suspended on a massive base. Mathematical expressions describing the measurement and computation process of the values of the above mentioned 6 force and torque vectors are proposed. Examples of measuring processes and graphical presentations of some experimental results are given in this work. In this work we propose further development of the discussed design by reducing the mass and inertia moments of this frame and relative positioning the model to it, in such a way reducing the caused by these dynamic parameters disturbing the measurements. In this case the model pattern for air flow influence measurements were made on a flat disc-like body.

2. Brief overview of wind tunnels.

Means for studying and determining the forces and torques acting on bodies influenced by high air flow speeds or subjected to variable wind speeds in air tunnels are required for both science and industry. This airflows influence on a body (or a system of bodies) is used for estimation the air resistance acting on these bodies or body. In the authors work [1] is brought a brief list of three balances that are usually applied for measuring wind drag forces and torques, lifting or carrying forces and torques, "air attacking angle" are examples of such parameters.

Partly the described in the mentioned paper measuring lay-outs are illustrated by examples given in Ewalds paper [2] from 2000. Another type of internal six- component wind-tunnel

balance is that having three-dimensional mechanism, as described by Gorlin and Slezinger [3], 2000. A solution alike to mentioned here belongs also to Corliss and Cole [4] 1998. In these cases a multi-component balances are placed in the tunnel being by means of elastic cables connected to corresponding elements of the measured pattern. This set disturbs the air flow in the tunnel to some extent.

The model can be via an enough elastic rod connected to the tail part of the investigated model and provided with differently oriented strain gauges gives the needed measured information describing the acting forces and torques. Pope and Harper [5] 1999 describe developed some calibration rigs for internal strain gauge balances.

The closest to the proposed design is the model placed on a platform inside the tunnel. And the forces are measured with 6-DOF hexapod-like balances placed outside the tunnel. (See Nguen et al. [6], 2002 and Kerr et al [7], 1989)

In this work, we propose to use a fourth orthogonal structure of a parallel robot directly in the chain of force and moment components, acting on the model, and computation. An *idea came* to shorten the process of investigation of the forces and moments acting on the model in the tunnel, which avoids the amount of unnecessary bodies in the tunnel and their *interference*. This proposed measurement method in the wind tunnel is close to the discussed earlier external 6-DOF to certain extent improved approach. Some ideas of this kind were discussed in the authors work Chapsky et al. [10], 2007, and the work [11] of Lui, S.A. and Tso, H. L., 2002. The main purpose of this paper is to propose and demonstrate experimentation with a wind tunnel structure including the model to be investigated, a measuring element combined with a computer. This system (shown in Fig.1.) uses the corresponding functions (or equations) for each of six force and moment components depending upon the air speed and the shape of the investigated model. This work is devoted to introduce a different measuring approach and shows its advantages offering the fourth kind of dealing with the problem. The fourth kind of balance proposed in this paper has once calibrated load cells and once written computation program for any fixed model used for investigation.

- only one rod is placed in the tunnel for fastening the investigation pattern;
- the balances and measuring sensors (load-cells) are located outside the tunnel supplying the needed information to the computer;
- values of the acting, due to the wind, forces and torques are automatically shown on the computer's screen;
- there are no interactions between the six measured and computed values as it often happens in other systems.

Later we show 7 pages with computed examples of all here mentioned types (even those which we are not able to realize for our tunnel).

3. Experimental arrangement

A general view of the wind tunnel built at the Mechanical Engineering Department of Ben Gurion University of the Negev, Israel is shown in Fig.1.

In Fig.2 a close view of the wind tunnel near the outer frames and the places for movable frame's suspension are given. Also the door for the pattern fastening and its orientation is seen here. Fig.3 shows the load-cells used in this design. It used for the measuring the value of the mechanical response to the wind forces. The maximum air speed in the tunnel is 40 m/sec. Length of the tunnel is about 30 m.



Fig. 1. Wind tunnel device in the aerodynamic laboratory of BGU of the Negev, (general view).



Movable frame

Immovable frame

Fig. 2. Wind tunnel. The movable aluminum frame provides the information about the X, Y, and Z displacements of the pattern and its rotations around these axes. The steel made immovable frame is the base of the arrangement.

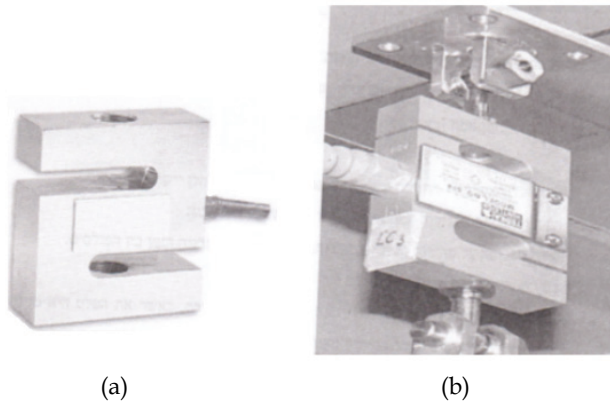


Fig. 3. The Data-Logger of the 34970 type: (a) S-beam load cell, (b) view of the suspension including the Data-Logger.

Cross-section of the tunnel equals $0.7 \times 0.7 \text{ m}^2$. The pattern is fixed in the middle of the earlier mentioned rod as it is schematically shown in Fig.4. This experimental case discussed in work [1];

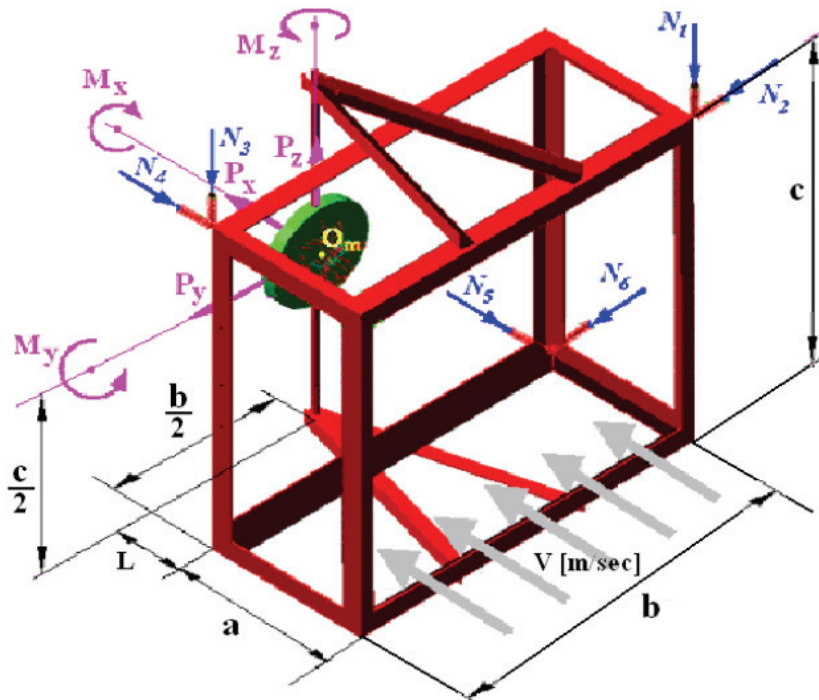


Fig. 4. Lay-out of the movable old frame primarily designed and built around the tunnel: $a = 470$, $b = 1050$, $c = 1030$, $L = 200$, (the dimensions are millimetres).

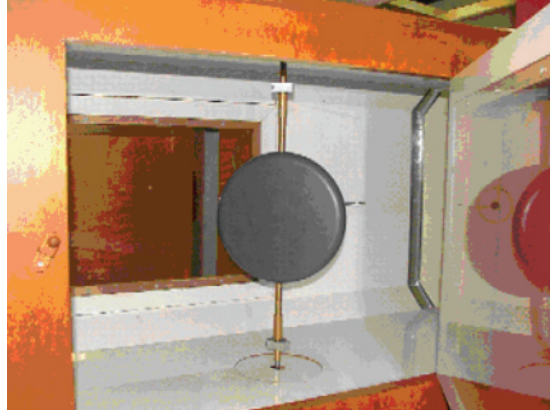


Fig. 5. Pattern location in the wind tunnel: flat disc placed in it.

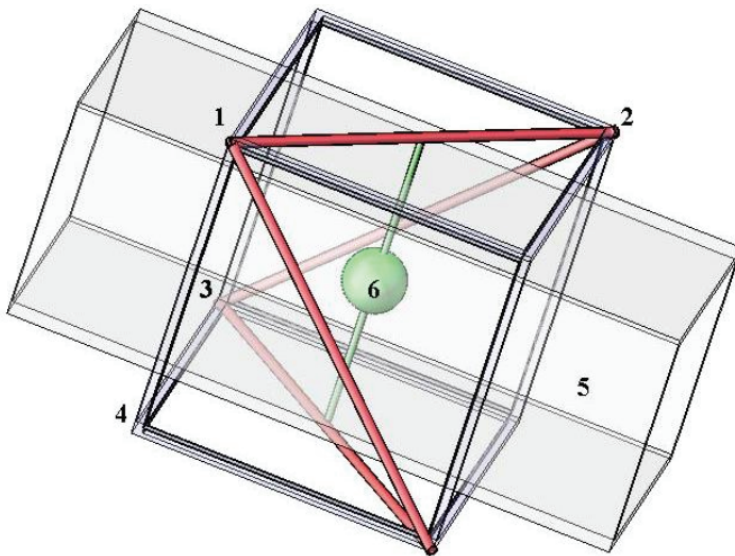


Fig. 6. Relative design of the new and old (previous) frame construction.

4. Main idea of the new frame design.

To improve the dynamical performance of the proposed apparatus the set of different frame arrangements has been investigated. The difference between experimental arrangements lies in the mass of the entire design, in the position of the tested pattern (flat disc) relative to the frame, and in the symmetry of the frame shape.

To reduce the mass of the frame without changing the geometric dimensions the new arrangement has been proposed. Its design is clear from figure 6. In the Fig.6 the red frame is the new proposed design, the "gray" profile 5 demonstrates the wind tunnel, the "black" frame 4 is the previous design, 1, 2, 3 are the fastening points of the frame suspensions for both cases (new and old design), the green sphere 6 is the investigated pattern.

Every point of the frame suspensions has two directions of force measuring. For instance, the point 1 measures in directions "x" and "z", the point 2 measures in directions "z" and "y", point 3 in directions "x" and "y".

The investigated models were conventionally named as follows:

“Old” - with full set of 12 edges, “New” - with reduced mass (4 edges);

“Regular” - with pattern, located outside the frame;

“Central” - with pattern in the geometrical center of the frame;

“Symmetric” - with cube-shaped frame coverage figure.

The investigated frame designs and their dimensions are shown in Table 1.

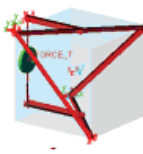
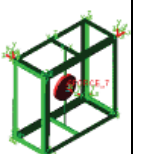
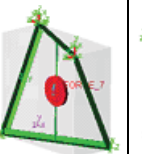
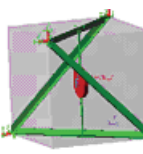
Old Regular	New Regular	Old Central	New Central	Old symmetric	New Symmetric
					
a = 470	a = 1050	a = 470	a = 470	a = 1050	a = 1050
b = 1050					
c = 1030	c = 1050	c = 1030	c = 1030	c = 1050	c = 1050
L = 200	L = 200	L = -a/2	L = -a/2	L = -a/2	L = -a/2

Table 1. Proposed frames, their design and dimensions.

All these “Old” and “New” kinds of frames are checked dynamically and therefore can be accordingly analyzed.

The item we propose for publishing is somehow continuation of the paper published earlier and caused your attention. We speak about an improved design of the same principal structure, however improved because its main mass is considerably smaller despite the same geometric dimensions. The said is clear from the figure 6.

5. Dynamical investigation

Comparative dynamic investigations of virtual models of tunnel balances have been carried out by means of the interactive computer-based motion simulation software MSC ADAMS/View.

Every virtual model was loaded consequentially in all directions by harmonic forces or moments $U(t)$ with varying frequency.

$$U(t) = U_0 \sin (\omega (t)*t) = U_0 \sin ((1000*t)*t),$$

Where U_0 - initial magnitude of the force or moment, $\omega (t)$ -frequency, which depends on the time according equation: $\omega (t) = 1000*time$.

The responses of each spring have been measured and Bode plots were calculated with purpose to define the bandwidth of tested model. Bandwidth corresponds to the frequencies, where Bode-magnitude plot lay in the $\pm 3dB$ range relative to the initial (steady-state) value. For convenience, the Bode plots were shifted to zero value in initial state by multiplying the measured results on some factors. All factors were calculated by symbolic mathematics software such as Mathematica-7. The applied Mathematica-7 program is shown in appendix 1.

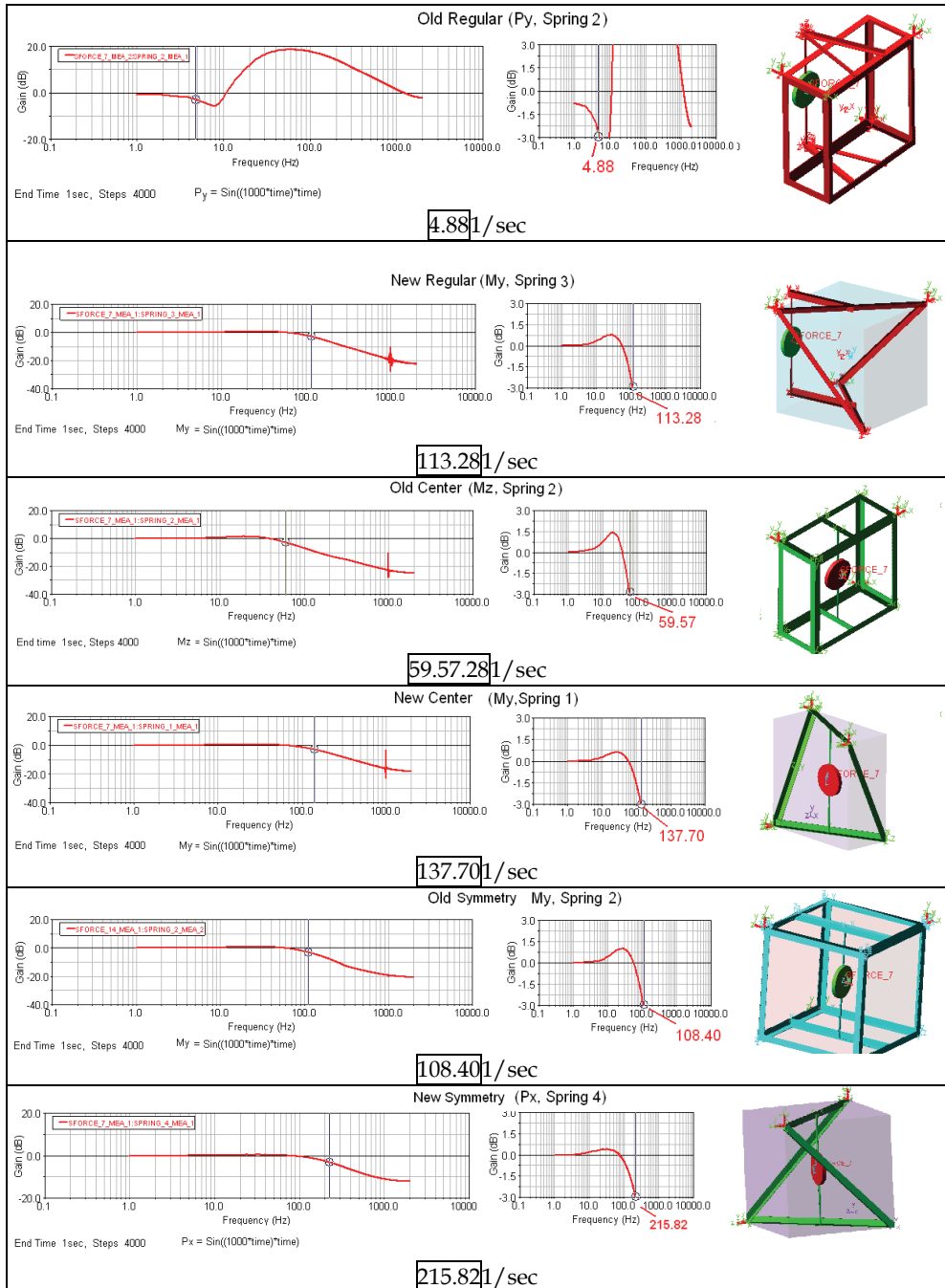


Table 2. The determinative Bandwidths

The worst Bode plots relative to spring forces and corresponding bandwidths for every force and torque directions (P_x , P_y , P_z , M_x , M_y , M_z , according notations in Figure 5) are shown in Appendix 2. The determinative ones for each design are shown in Table 2.

As clear from Table 2, the most desirable is the design "New Symmetry", which has bandwidth 215.82 Hz. The "New central" is applicable too. If it is not possible to locate the pattern in the center of the frame due to the limitations of the wind tunnel design the "New regular" model can be applied, but with bandwidth 113.28 Hz. All these models are better than earlier model "Old Regular", which has bandwidth 4.88Hz in P_y and P_z directions, despite the fact that in P_x direction it has bandwidth 156.25Hz.

6. Conclusions

1. The proposed device requires a universal sequence and simple action for receiving the measured data. Investigator must only fasten the pattern on the mentioned rod.
2. Dynamic estimations of the virtual model of proposed tunnel balance by means of the interactive computer-based ADAMS/View system showed that the working frequency of the proposed method and device are limited to a $\sim 100\div 200$ Hz bandwidth.
3. The translational isotropy of the proposed device is defined by the independence of the sensitivity of measurement from the direction of the operating forces.
4. For estimation of the anisotropy of devices, the anisotropy index which equals to the ratio of maximum and minimum stiffness values is applied. Two types of indexes are separately used: for translational and rotational stiffness values (see Table 2).
5. The proposed devices "New Symmetry" and "Old Symmetry" has better dynamic features than conventionally used systems: it is fully isotropic from the point of view of translational stiffness and has a high level of isotropy from the view point of rotational stiffness.
6. The proposed device shows at least the theoretical possibility to improve the dynamic properties of the wind tunnel comparing with the already offered.

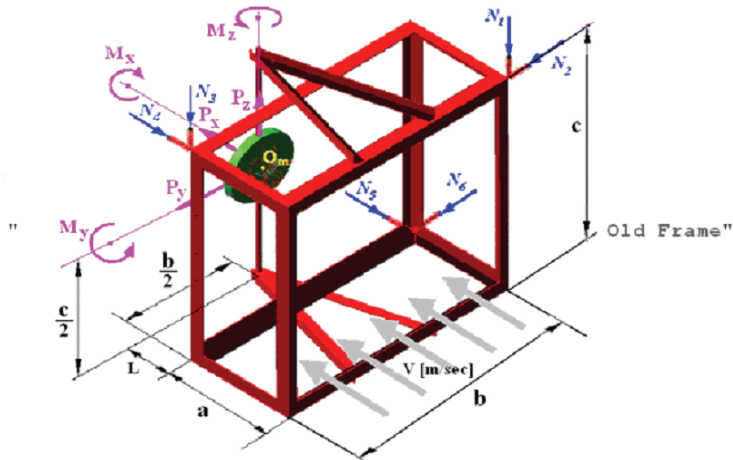
7. References

- [1] V. Portman, B.Z. Sandler, V. Chapsky, I. Zilberman, A 6-DOF isotropic measuring system for force and torque components of drag for use in wind tunnels, (Innovative design), *Int J Mech Mater Des* (2009) 5:337-352.
- [2] F R Ewald, Multi-component force balances for conventional and cryogenic wind tunnels, *Meas. Sci. Technol.*11 (2000) R81-R94. Conference, 20th, Albuquerque, NM, June 15-18, 1998
- [3] S.M.Gorlin, I.I. Slezinger, Wind tunnels and their instrumentation, translated from Russian for NASA tt f-346, 2000.
- [4] Alan Pope, Judu J. Harpes, Law speed wind tunnels testing, John Wiley & Sons, 1999.
- [5] A. Bentur, N. S. Berke, Sidney Diamond -... Steel Corrosion in Concrete: Fundamentals and Civil Engineering Practice Arnon Israel Sidney Diamond School of Civil Engineering, Purdue University, 1997, 201 pp.
- [6] Tuttle, S.L., Mee, D.J., Simmons, J.M., Daniel W.J., et al., "NASA technical reports", 1994.
- [7] S.R. Sanderson and J.M. Simmons, "Force Measurement in Impulse Facilities, Department of Mechanical Engineering ", University of Queensland, 2006
- [8] C.C. Nguen, S.S. Antrazi, Z.-L.Zhou, C.E. Cambell, Jr. "Analysis and Experimentation of a Stewart Platform-based Force/Torque Sensor", *International Journal of Robotics and Automation*, Vol. 7, No. 3, 1992, 133 - 141.

[9] D.R. Kerr, "Analysis, Properties, and Design of a Stewart-Platform Transducer", in Transaction of the ASME, Journal of Mechanisms, Transmissions, and Automation in Design", March, 1989, Vol. 111/25, pp. 25 - 28.
 [10] V. Chapsky, V. Portman, B-Z Sandler, 2007, Single-mass 6-DOF isotropic accelerometer with segmented PSD sensors, Sensors and Actuators: A physical, Vol. A135/2, pp. 558-569.
 [11] Liu, S.A., Tso, H.L., 2002, A novel six-component force sensor of good measurement isotropy and sensitivities, Sensors and Actuators: A physical, Vol. A100, pp. 223-230.
 [12] Z. Aliyazicioglu, Electrical and Computer Engineering Department, Cal Poly Pomona ECE307-8, ECE

Appendix 1. Mathematica-7 computation program.

```
"Removing all data";
Remove["Global`*"];
```



"Set of equations of static equilibrium of forces and moments"

```
M1 = {Px + N4 + N5 == 0, Py + N2 + N6 == 0, Pz + N1 + N3 == 0,
      Mx + N3 * b / 2 - N1 * b / 2 - N2 * c / 2 + N6 * c / 2 == 0,
      My + N3 * L + N1 * (L + a) - N5 * c / 2 + N4 * c / 2 == 0,
      Mz + N5 * b / 2 - N4 * b / 2 - N6 * L - N2 * (L + a) == 0};
```

```
MatrixForm[%]
```

$$\begin{pmatrix} N4 + N5 + Px == 0 \\ N2 + N6 + Py == 0 \\ N1 + N3 + Pz == 0 \\ -\frac{b N1}{2} - \frac{c N2}{2} + \frac{b N3}{2} + \frac{c N6}{2} + Mx == 0 \\ \frac{c N4}{2} - \frac{c N5}{2} + N3 L + N1 (a + L) + My == 0 \\ -\frac{b N4}{2} + \frac{b N5}{2} - N6 L - N2 (a + L) + Mz == 0 \end{pmatrix}$$

"Solving the system of equations"

SolvMatrix = Solve[M1, {N1, N2, N3, N4, N5, N6}]

$$\left\{ \left\{ \begin{array}{l} N3 \rightarrow -\frac{2 a Mx - 2 b My - 2 c Mz - a c Py - 2 c L Py + 3 a b Pz + 2 b L Pz}{4 a b}, \\ N1 \rightarrow -\frac{-2 a Mx + 2 b My + 2 c Mz + a c Py + 2 c L Py + a b Pz - 2 b L Pz}{4 a b}, \\ N4 \rightarrow -\frac{2 a Mx + 2 b My - 2 c Mz + 2 b c Px - a c Py - 2 c L Py - a b Pz - 2 b L Pz}{4 b c}, \\ N5 \rightarrow -\frac{-2 a Mx - 2 b My + 2 c Mz + 2 b c Px + a c Py + 2 c L Py + a b Pz + 2 b L Pz}{4 b c}, \\ N2 \rightarrow -\frac{-2 a Mx - 2 b My - 2 c Mz + a c Py - 2 c L Py + a b Pz + 2 b L Pz}{4 a c}, \\ N6 \rightarrow -\frac{2 a Mx + 2 b My + 2 c Mz + 3 a c Py + 2 c L Py - a b Pz - 2 b L Pz}{4 a c} \end{array} \right\} \right\}$$

"Conditions of the simulation";

condPx = {Py -> 0, Pz -> 0, Mx -> 0, My -> 0, Mz -> 0};

condPy = {Px -> 0, Pz -> 0, Mx -> 0, My -> 0, Mz -> 0};

condPz = {Py -> 0, Px -> 0, Mx -> 0, My -> 0, Mz -> 0};

condMx = {Py -> 0, Pz -> 0, Px -> 0, My -> 0, Mz -> 0};

condMy = {Py -> 0, Pz -> 0, Mx -> 0, Px -> 0, Mz -> 0};

condMz = {Py -> 0, Pz -> 0, Mx -> 0, My -> 0, Px -> 0};

"Geometric conditions; Regular, Central, Symmetric,
and L for central and symmetric configurations";

condGeomReg = {a -> 470, b -> 1050, c -> 1030, L -> 200};

condGeomSym = {a -> 1050, b -> 1050, c -> 1050};

condGeomCentr = {a -> 470, b -> 1050, c -> 1030};

condL = {L -> -a / 2};

"Numerical results";

RegPx = SolvMatrix / . condPx / . condGeomReg

$$\left\{ \left\{ N3 \rightarrow 0, N1 \rightarrow 0, N4 \rightarrow -\frac{Px}{2}, N5 \rightarrow -\frac{Px}{2}, N2 \rightarrow 0, N6 \rightarrow 0 \right\} \right\}$$

RegPy = SolvMatrix / . condPy / . condGeomReg

$$\left\{ \left\{ N3 \rightarrow \frac{2987 Py}{6580}, N1 \rightarrow -\frac{2987 Py}{6580}, N4 \rightarrow \frac{29 Py}{140}, N5 \rightarrow -\frac{29 Py}{140}, N2 \rightarrow -\frac{7 Py}{188}, N6 \rightarrow -\frac{181 Py}{188} \right\} \right\}$$

RegPz = SolvMatrix / . condPz / . condGeomReg

$$\left\{ \left\{ N3 \rightarrow -\frac{181 Pz}{188}, N1 \rightarrow -\frac{7 Pz}{188}, N4 \rightarrow \frac{87 Pz}{412}, N5 \rightarrow -\frac{87 Pz}{412}, N2 \rightarrow -\frac{9135 Pz}{19364}, N6 \rightarrow \frac{9135 Pz}{19364} \right\} \right\} \circ \frac{L Pz}{L Pz},$$

RegMx = SolvMatrix / . condMx / . condGeomReg

$$\left\{ \left\{ N3 \rightarrow -\frac{Mx}{2100}, N1 \rightarrow \frac{Mx}{2100}, N4 \rightarrow -\frac{47 Mx}{216300}, N5 \rightarrow \frac{47 Mx}{216300}, N2 \rightarrow \frac{Mx}{2060}, N6 \rightarrow -\frac{Mx}{2060} \right\} \right\}$$

RegMy = SolvMatrix / . condMy / . condGeomReg

$$\left\{ \left\{ N3 \rightarrow \frac{My}{940}, N1 \rightarrow -\frac{My}{940}, N4 \rightarrow -\frac{My}{2060}, N5 \rightarrow \frac{My}{2060}, N2 \rightarrow \frac{21 My}{19364}, N6 \rightarrow -\frac{21 My}{19364} \right\} \right\}$$

RegMz = SolvMatrix / . condMz / . condGeomReg

$$\left\{ \left\{ N3 \rightarrow \frac{103 Mz}{98700}, N1 \rightarrow -\frac{103 Mz}{98700}, N4 \rightarrow \frac{Mz}{2100}, N5 \rightarrow -\frac{Mz}{2100}, N2 \rightarrow \frac{Mz}{940}, N6 \rightarrow -\frac{Mz}{940} \right\} \right\}$$

CentrPx = SolvMatrix / . condPx / . condL / . condGeomCentr

$$\left\{ \left\{ N3 \rightarrow 0, N1 \rightarrow 0, N4 \rightarrow -\frac{Px}{2}, N5 \rightarrow -\frac{Px}{2}, N2 \rightarrow 0, N6 \rightarrow 0 \right\} \right\}$$

CentrPy = SolvMatrix / . condPy / . condL / . condGeomCentr

$$\left\{ \left\{ N3 \rightarrow 0, N1 \rightarrow 0, N4 \rightarrow 0, N5 \rightarrow 0, N2 \rightarrow -\frac{Py}{2}, N6 \rightarrow -\frac{Py}{2} \right\} \right\}$$

CentrPz = SolvMatrix / . condPz / . condL / . condGeomCentr

$$\left\{ \left\{ N3 \rightarrow -\frac{Pz}{2}, N1 \rightarrow -\frac{Pz}{2}, N4 \rightarrow 0, N5 \rightarrow 0, N2 \rightarrow 0, N6 \rightarrow 0 \right\} \right\}$$

CentrMx = SolvMatrix / . condMx / . condL / . condGeomCentr

$$\left\{ \left\{ N3 \rightarrow -\frac{Mx}{2100}, N1 \rightarrow \frac{Mx}{2100}, N4 \rightarrow -\frac{47 Mx}{216300}, N5 \rightarrow \frac{47 Mx}{216300}, N2 \rightarrow \frac{Mx}{2060}, N6 \rightarrow -\frac{Mx}{2060} \right\} \right\}$$

CentrMy = SolvMatrix / . condMy / . condL / . condGeomCentr

$$\left\{ \left\{ N3 \rightarrow \frac{My}{940}, N1 \rightarrow -\frac{My}{940}, N4 \rightarrow -\frac{My}{2060}, N5 \rightarrow \frac{My}{2060}, N2 \rightarrow \frac{21 My}{19364}, N6 \rightarrow -\frac{21 My}{19364} \right\} \right\}$$

CentrMz = SolvMatrix / . condMz / . condL / . condGeomCentr

$$\left\{ \left\{ N3 \rightarrow \frac{103 Mz}{98700}, N1 \rightarrow -\frac{103 Mz}{98700}, N4 \rightarrow \frac{Mz}{2100}, N5 \rightarrow -\frac{Mz}{2100}, N2 \rightarrow \frac{Mz}{940}, N6 \rightarrow -\frac{Mz}{940} \right\} \right\}$$

```

SymPx = SolvMatrix /. condPx /. condL /. condGeomSym
{{N3 → 0, N1 → 0, N4 → - $\frac{Px}{2}$ , N5 → - $\frac{Px}{2}$ , N2 → 0, N6 → 0}}

SymPy = SolvMatrix /. condPy /. condL /. condGeomSym
{{N3 → 0, N1 → 0, N4 → 0, N5 → 0, N2 → - $\frac{Py}{2}$ , N6 → - $\frac{Py}{2}$ }}

SymPz = SolvMatrix /. condPz /. condL /. condGeomSym
{{N3 → - $\frac{Pz}{2}$ , N1 → - $\frac{Pz}{2}$ , N4 → 0, N5 → 0, N2 → 0, N6 → 0}}

SymMx = SolvMatrix /. condMx /. condL /. condGeomSym
{{N3 → - $\frac{Mx}{2100}$ , N1 →  $\frac{Mx}{2100}$ , N4 → - $\frac{Mx}{2100}$ , N5 →  $\frac{Mx}{2100}$ , N2 →  $\frac{Mx}{2100}$ , N6 → - $\frac{Mx}{2100}$ }}

SymMy = SolvMatrix /. condMy /. condL /. condGeomSym
{{N3 →  $\frac{My}{2100}$ , N1 → - $\frac{My}{2100}$ , N4 → - $\frac{My}{2100}$ , N5 →  $\frac{My}{2100}$ , N2 →  $\frac{My}{2100}$ , N6 → - $\frac{My}{2100}$ }}

SymMz = SolvMatrix /. condMz /. condL /. condGeomSym
{{N3 →  $\frac{Mz}{2100}$ , N1 → - $\frac{Mz}{2100}$ , N4 →  $\frac{Mz}{2100}$ , N5 → - $\frac{Mz}{2100}$ , N2 →  $\frac{Mz}{2100}$ , N6 → - $\frac{Mz}{2100}$ }}

RegPxNew = SolvMatrix /. condPx /. condGeomSym /. L → 200
{{N3 → 0, N1 → 0, N4 → - $\frac{Px}{2}$ , N5 → - $\frac{Px}{2}$ , N2 → 0, N6 → 0}}

RegPyNew = SolvMatrix /. condPy /. condGeomSym /. L → 200
{{N3 →  $\frac{29 Py}{84}$ , N1 → - $\frac{29 Py}{84}$ , N4 →  $\frac{29 Py}{84}$ , N5 → - $\frac{29 Py}{84}$ , N2 → - $\frac{13 Py}{84}$ , N6 → - $\frac{71 Py}{84}$ }}

RegPzNew = SolvMatrix /. condPz /. condGeomSym /. L → 200
{{N3 → - $\frac{71 Pz}{84}$ , N1 → - $\frac{13 Pz}{84}$ , N4 →  $\frac{29 Pz}{84}$ , N5 → - $\frac{29 Pz}{84}$ , N2 → - $\frac{29 Pz}{84}$ , N6 →  $\frac{29 Pz}{84}$ }}

RegMxNew = SolvMatrix /. condMx /. condGeomSym /. L → 200
{{N3 → - $\frac{Mx}{2100}$ , N1 →  $\frac{Mx}{2100}$ , N4 → - $\frac{Mx}{2100}$ , N5 →  $\frac{Mx}{2100}$ , N2 →  $\frac{Mx}{2100}$ , N6 → - $\frac{Mx}{2100}$ }}

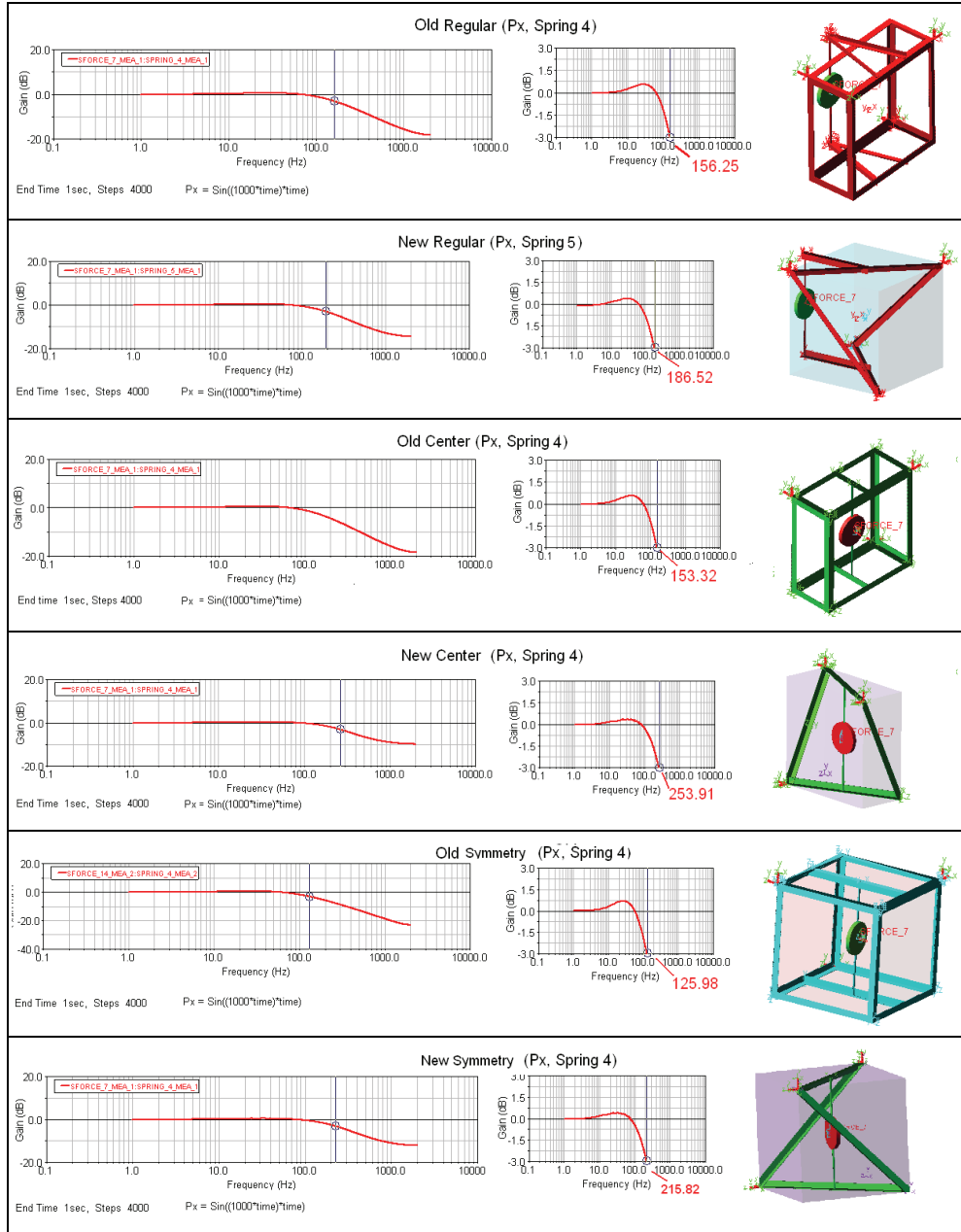
RegMyNew = SolvMatrix /. condMy /. condGeomSym /. L → 200
{{N3 →  $\frac{My}{2100}$ , N1 → - $\frac{My}{2100}$ , N4 → - $\frac{My}{2100}$ , N5 →  $\frac{My}{2100}$ , N2 →  $\frac{My}{2100}$ , N6 → - $\frac{My}{2100}$ }}

RegMzNew = SolvMatrix /. condMz /. condGeomSym /. L → 200
{{N3 →  $\frac{Mz}{2100}$ , N1 → - $\frac{Mz}{2100}$ , N4 →  $\frac{Mz}{2100}$ , N5 → - $\frac{Mz}{2100}$ , N2 →  $\frac{Mz}{2100}$ , N6 → - $\frac{Mz}{2100}$ }}

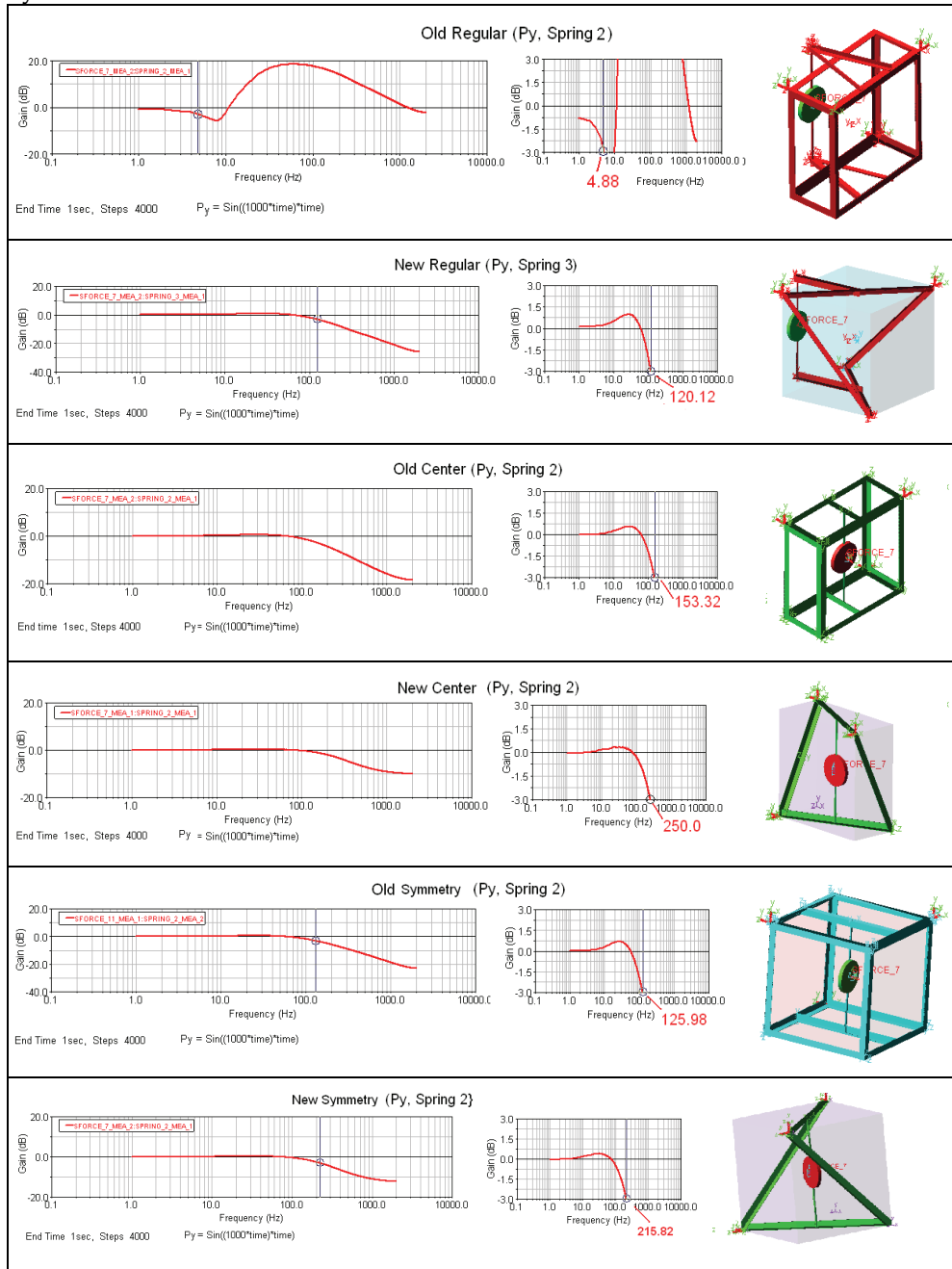
```

Appendix 2. Bode plots of the forces and torques acts on the pattern relative to spring forces.

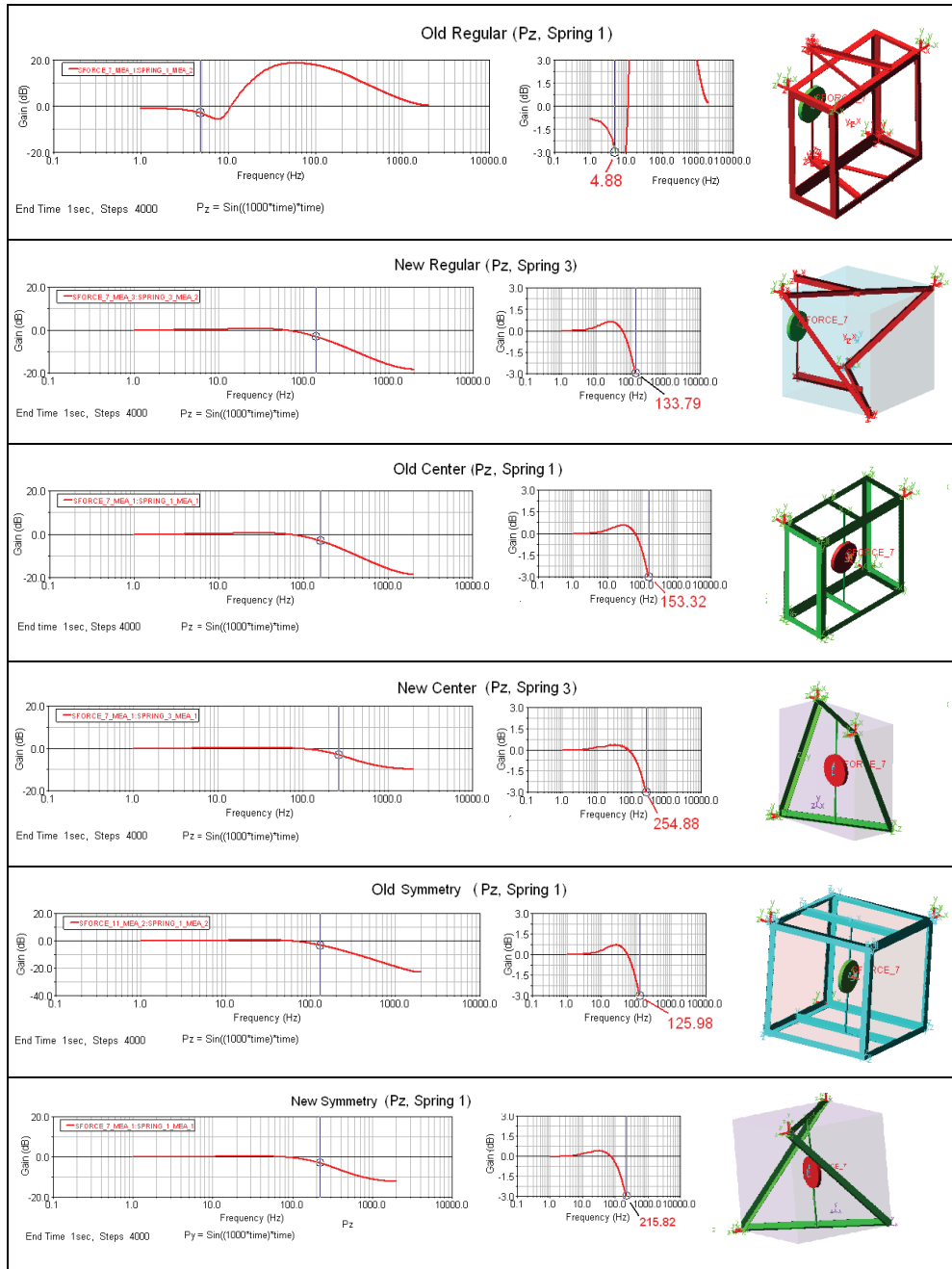
Px



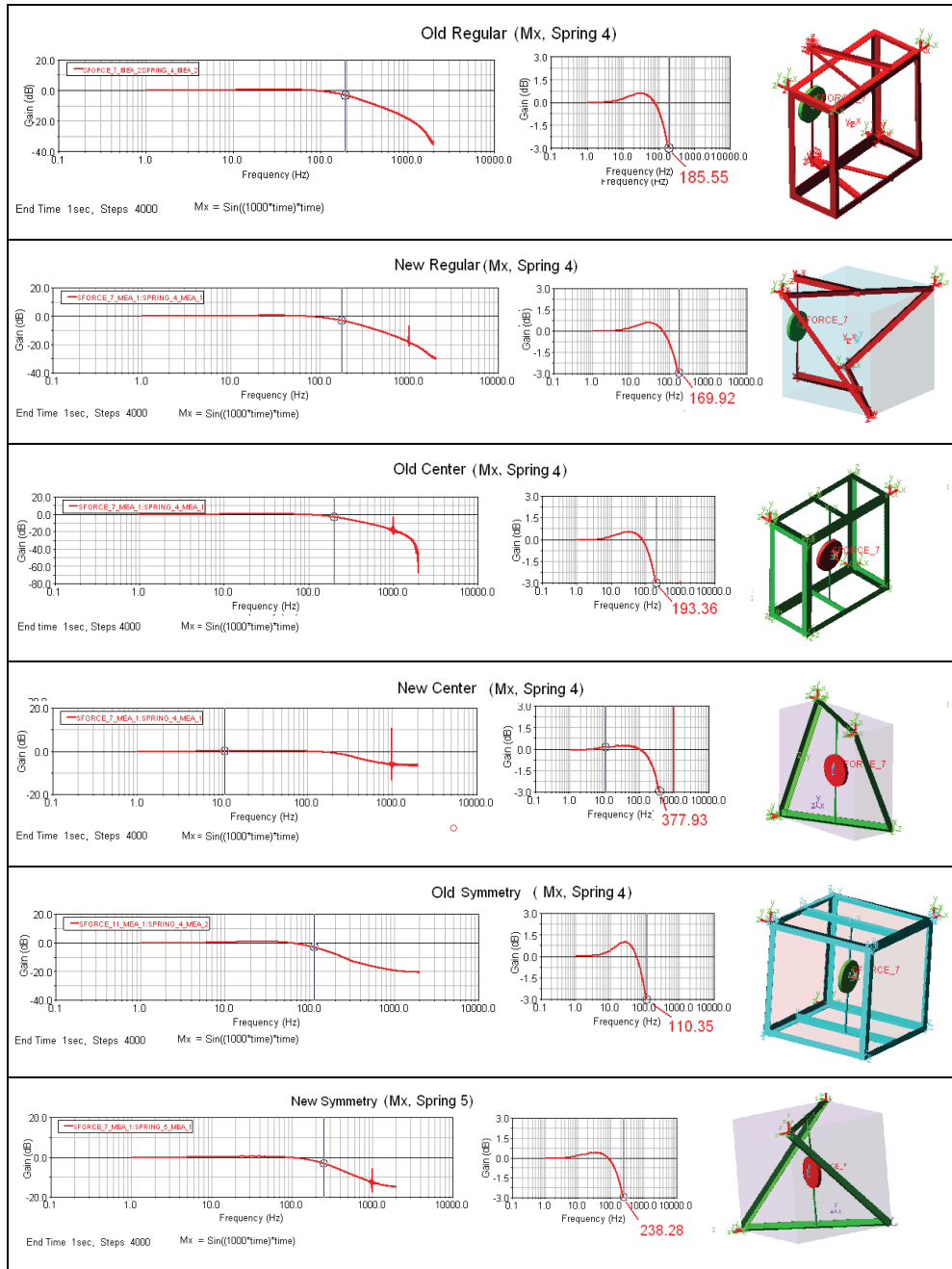
Py



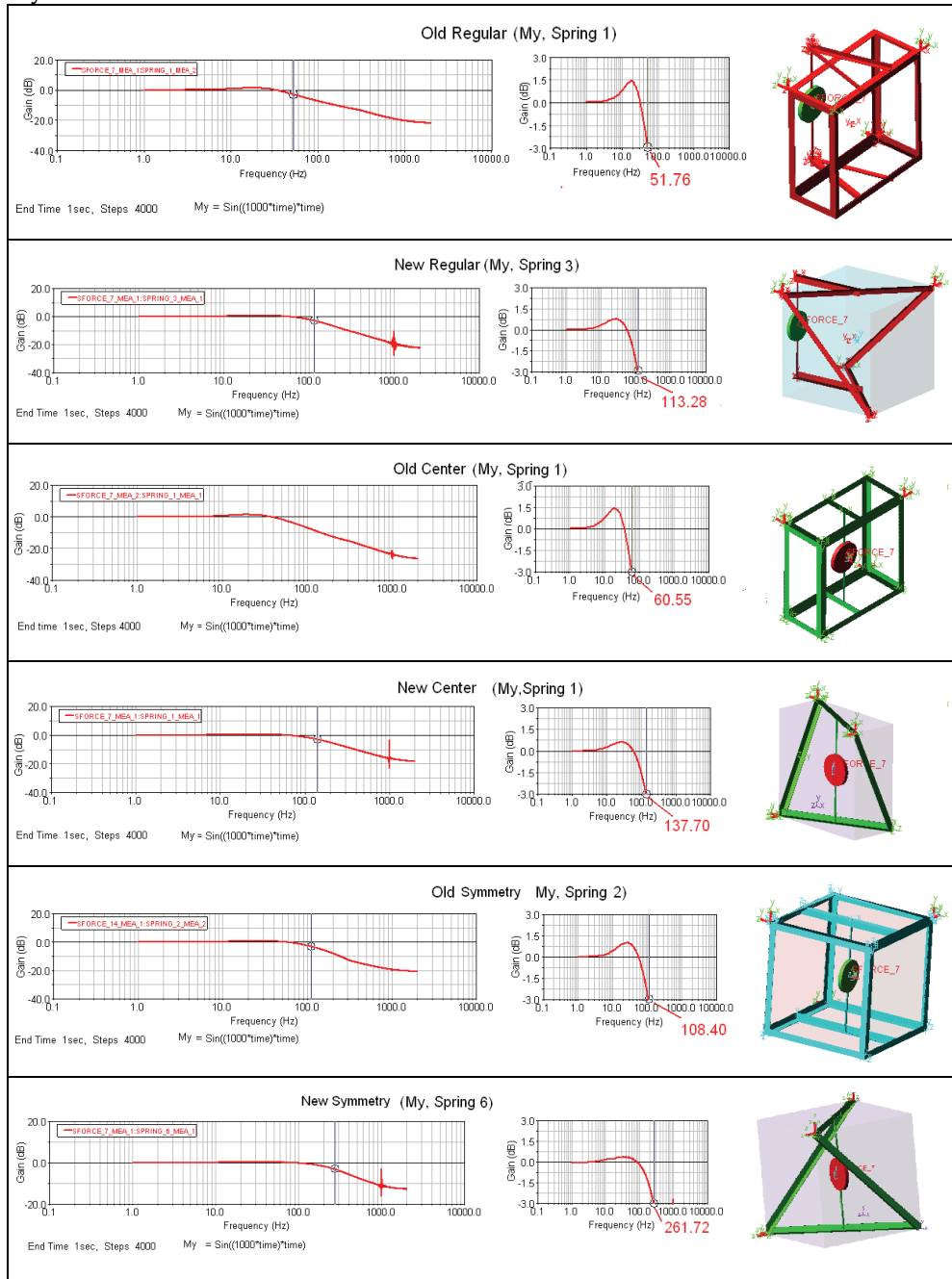
Pz



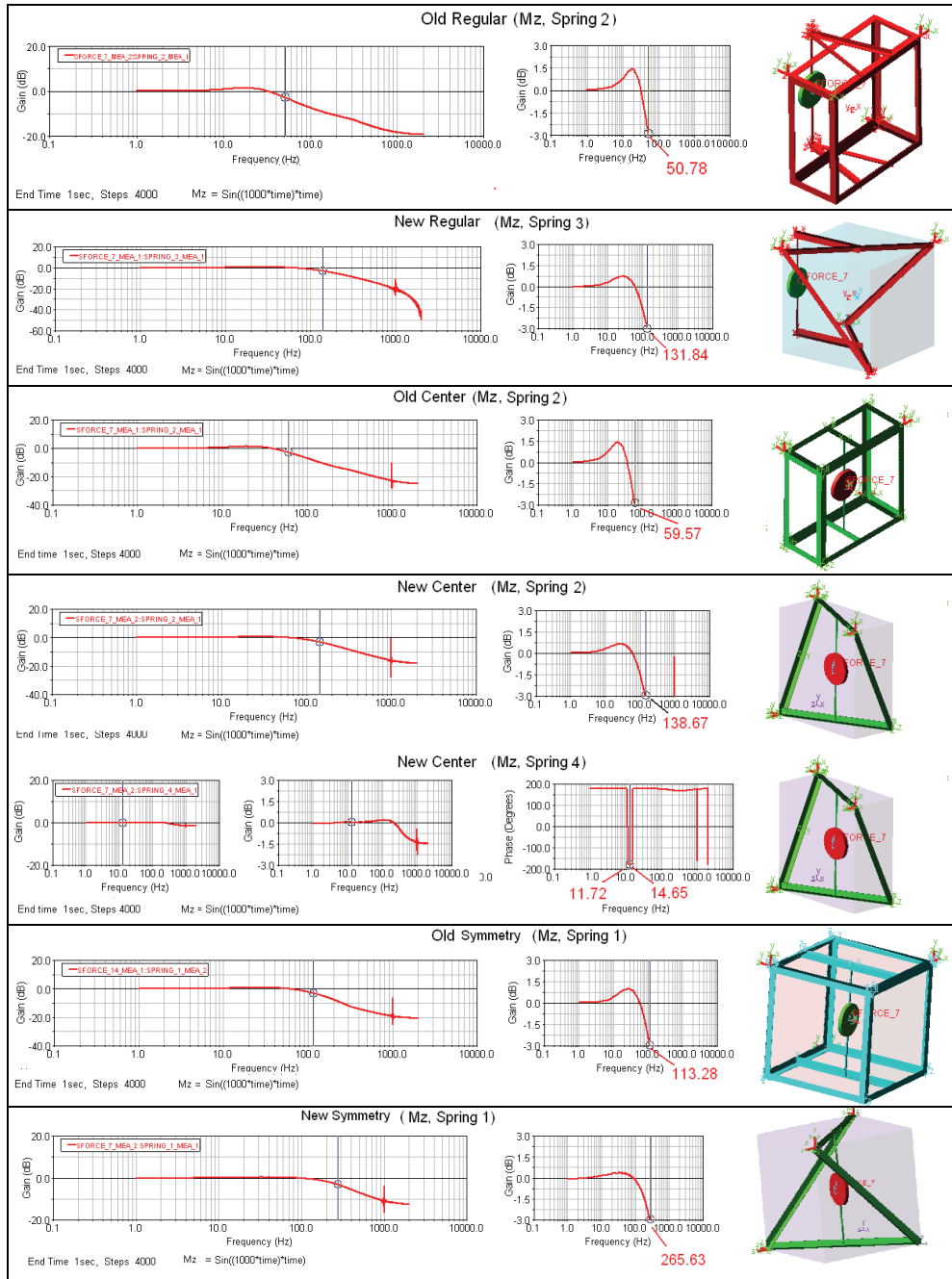
Mx



My



Mz



Stiffness Enhancement and Motion Control of a 6-DOF Wire-driven Parallel Manipulator with Redundant Actuations for Wind Tunnels

Xin Liu, Yuanying Qiu and Xuechao Duan
Xidian University
P.R.China

1. Introduction

As is well known, a wire-driven parallel manipulator is a manipulator whose end-effector is driven by a number of cables instead of rigid links. It shows several promising advantages over its rigid-link counterpart, such as simple light-weight mechanical structure, low moment inertia, large reachable workspace and high-speed motion. In the 1980s, the National Institute of Standards and Technology (NIST) in America invented a wire-driven parallel manipulator named RoboCrane for shipyards (Albus et al, 1993). So far, wire-driven parallel manipulators have been applied in load lifting, industrial machining, virtual reality and astronomic observation (Dekker et al, 2006; Ning et al, 2006; Ma & Diao, 2005). Because of the advantages and unique features of wires, wire-driven parallel manipulators have attracted a great attention in robotics literature. The first general classification was given by Ming and Higuchi (Ming and Higuchi, 1994). Based on the number of wires (m) and the number of degrees of freedom (n), wire-driven parallel manipulators were classified into three categories, i.e. the incompletely restrained positioning mechanisms ($m < n+1$), the completely restrained positioning mechanisms ($m = n+1$) and the redundantly restrained positioning mechanisms ($m > n+1$). Yamamoto *et al.* presented basic dynamics equations and a feedback control method based on exact linearization for the incompletely restrained positioning mechanisms (Yamamoto et al, 2004). Hithoshi *et al.* studied a robust PD control using adaptive compensation for translational wire-driven parallel manipulators of a completely restrained type (Hithoshi et al, 2007). Zi Bin *et al.* developed a fuzzy plus proportional-integral control method for the cable-cabin mechanism of 500m aperture spherical radio telescope (Zi et al, 2008). Yu Kun considered active stiffness control schemes as optimization problem with different criteria for redundantly restrained positioning mechanisms (Yu, 2008). In essence, a wire-driven parallel manipulator can be considered as a complex, time-varying, strong-coupled, multiple input and multiple output, and nonlinear system. Since the wires can only pull and not push on the platform, dynamics and control are key issues for high-precision motion of wire-driven parallel manipulators.

Wind tunnel tests of aircraft models are widely utilized to investigate the potential flight dynamics and aerodynamic characteristics of aircrafts at their early developing stage. Wire-driven parallel manipulators have been introduced to wind tunnels as flexible suspension systems of aircraft models in recent years (Liu et al, 2004). The posture of the scale model corresponding to the stream line of airflows can be adjusted by controlling the length of

wires to implement the six degree-of-freedom free flight motion. The aerodynamic forces exerted on the scale model can be calculated by measuring the tension of each wire. Comparing with traditional frame suspension systems, wire-driven parallel manipulators for wind tunnels have advantages in less aerodynamic interference and high precision of the test results. Preliminary achievements have been made in the Suspension ACTIVE pour Soufflerie (SACSO) project about the wire-driven parallel suspension system in low wind tunnels sponsored by Office National d'Études et de Recherches Aérospatiales (ONERA). The achievements include architecture design, workspace computation, force control and build-up of a prototype of the wire-driven parallel manipulator (Lafourcade, 2004). Zheng Yaqing et al. have developed some fundamental theoretical research work on workspace, wire tension distribution, stiffness, kinematics and control of the manipulators. Because of weak stiffness of wires, the aircraft model would deviate from the planned trajectory when it is in the streamline flow. The trajectory errors have significant effect on the force and moment measurement. Hence one challenging issue is to accurately implement the attitude control for wire-driven parallel manipulators in wind tunnels.

The flexible suspension system in wind tunnels proposed by Zheng, which can be viewed as a six degree-of-freedom eight wires driven parallel manipulator, is investigated in this paper (Zheng, 2004). In order to decrease the trajectory errors and improve the measurement precision, it is necessary to enhance stiffness of the flexible suspension system. In case of wire-driven parallel manipulators with redundant actuations, the stiffness of the manipulators have been researched by Yu (Yu, 2008) and Saeed Behzadipou (Behzadipour & Khajepour, 2006) respectively, based on the stiffness definition and the equivalent spring model. In this paper, an analytic expression of the stiffness of the flexible suspension system in wind tunnels is derived by using the differential transformation principle. In order to hurdle a low rigidity and poor positioning accuracy caused by the minimum wire tension solution, an optimal tension distribution method is applied for the enhancement of stiffness in lift, along-wind and pitching directions. The method resolves the uncertainty of wire tensions of the suspension system.

The motion control of the flexible suspension system in wind tunnels can be realized either in end-effector space or in joint space. The pose of the aircraft model must be measured in real time during the former control process. Measuring the pose of the aircraft model in wind tunnels is rather challenging, because the cross section of wind tunnels is limited and the existence of equipments disturbs air flows. Moreover, it is not desirable to obtain the pose of the aircraft model using direct kinematics, because of lots of time required by complicated calculation. Hence, a computed torque controller in joint space is employed for the flexible suspension system in wind tunnels. A dynamics compensation is introduced to a conventional proportional differential controller, so a modified proportional differential control strategy in the wire length coordinates is developed based on stiffness enhancement.

2. System description

Figure 1 shows the flexible suspension system driven by eight wires. Each wire is attached to the aircraft model at one end, and threads the pulleys mounted to the wind tunnel and winds around an actuated reel at the other end. The actuated reels allow the control of the pose of the aircraft model by controlling the length of their respective wires. The aerodynamic loads on the aircraft model can be calculated through measuring the wire tension by strain gages.



Fig. 1. The flexible suspension system for wind tunnel

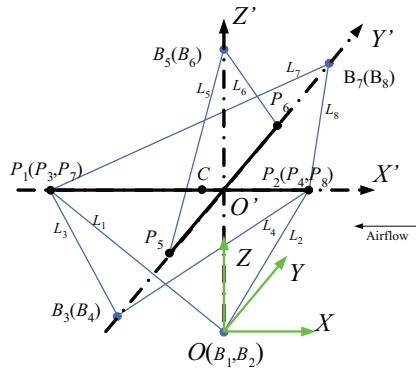


Fig. 2. Geometric definition of the suspension system

All geometric quantities are shown in Fig. 2. $OXYZ$ and $O'X'Y'Z'$ are coordinate frames attached to the wind tunnel and the aircraft model, respectively. C is the center of gravity of the aircraft model. The point where the i^{th} wire leaves the reel is denoted by B_i , and the connecting point on the aircraft model is denoted by P_i . The rotation matrix of the $O'X'Y'Z'$ with respect to $OXYZ$ is represented by

$$\begin{aligned}
 {}^oR_{o'} &= \text{rot}(z, \psi) \text{rot}(y, \beta) \text{rot}(x, \phi) \\
 &= \begin{bmatrix} \cos \psi \cos \beta & \cos \psi \sin \beta \sin \phi - \sin \psi \cos \phi & \cos \psi \sin \beta \cos \phi + \sin \psi \sin \phi \\ \sin \psi \cos \beta & \sin \psi \sin \beta \sin \phi + \cos \psi \cos \phi & \sin \psi \sin \beta \cos \phi - \cos \psi \sin \phi \\ -\sin \beta & \cos \beta \sin \phi & \cos \beta \cos \phi \end{bmatrix} \quad (1)
 \end{aligned}$$

where ϕ , β and ψ are the roll, pitch and yaw angles of the aircraft model respectively. The length of the i^{th} wire is expressed by

$$l_i = \| {}^oL_i \|_2 = \sqrt{({}^oB_i - {}^oP_o' - {}^oR_{o'} {}^oP_i)^T ({}^oB_i - {}^oP_o' - {}^oR_{o'} {}^oP_i)} \quad \text{for } i=1,2,\dots,8 \quad (2)$$

where ${}^oL_i = {}^oB_i - {}^oP_o - {}^oR_o, {}^oP_i$,

${}^oP_o = [{}^ox_o, {}^oy_o, {}^oz_o]^T$ is the position vector of the mobile frame's origin,

${}^oP_i = [{}^ox_{p_i}, {}^oy_{p_i}, {}^oz_{p_i}]^T$ is the position vector of point P_i in the mobile frame $O'X'Y'Z'$,

${}^oB_i = [{}^ox_{B_i}, {}^oy_{B_i}, {}^oz_{B_i}]^T$ is the position vector of point B_i in the fixed frame $OXYZ$.

Differentiating Eq.(2) with respect to time, and then assembling the eight resulting equations into matrix form, we obtain

$$\dot{l} = -J^T \dot{X} \quad (3)$$

where $l = [l_1 \ l_2 \ \dots \ l_8]^T$ is the wire-length vector,

$X = [{}^ox_o, {}^oy_o, {}^oz_o, \phi \ \beta \ \psi]^T$ is the posture vector of the aircraft model,

$J = \begin{bmatrix} {}^ou_1 & {}^ou_2 & \dots & {}^ou_8 \\ ({}^oR_o, {}^oP_1) \times {}^ou_1 & ({}^oR_o, {}^oP_2) \times {}^ou_2 & \dots & ({}^oR_o, {}^oP_8) \times {}^ou_8 \end{bmatrix} \in \mathbf{R}^{6 \times 8}$ is a pose-dependent matrix,

${}^ou_i = {}^oL_i / \|{}^oL_i\|_2$ is the unit vector along the i^{th} wire.

The equation of static equilibrium can be written as

$$JT + F = 0 \quad (4)$$

where $T = [t_1 \ t_2 \ \dots \ t_8]^T$ is the wire tension vector, $F = \begin{bmatrix} F_R \\ M_R \end{bmatrix}$ summarizes all other force and torques acting on the aircraft model.

3. Analytic stiffness

The influence of the wire tension on stiffness of the flexible suspension system is investigated, and an analytic expression of the stiffness is derived from the differential transformation principle. When an infinitesimal wrench ∂F is applied to the aircraft model, the posture of the aircraft model changes by an infinitesimal deflection ∂X . The Stiffness matrix K of the suspension system is

$$K = \frac{\partial F}{\partial X} = -\frac{\partial J}{\partial X} T - J \frac{\partial T}{\partial X} \quad (5)$$

For the first term in the equation (5), ∂J can be expressed by the product of an infinitesimal deflection ∂X and a three-dimensional matrix which excludes ∂X . Assuming the matrix H is equal to $\frac{\partial J}{\partial X}$, we obtain

$$\begin{cases} H = [H_1 \ H_2 \ \dots \ H_8] \in \mathbf{R}^{6 \times 6 \times 8} \\ H_i = \frac{1}{l_i} \begin{bmatrix} -I & {}^oP_i \times \\ [{}^oL_i \times] [({}^oR_o, {}^oP_i) \times] - [({}^oR_o, {}^oP_i) \times] [{}^oP_i \times] \end{bmatrix} \in \mathbf{R}^{6 \times 6} \end{cases} \quad (6)$$

where $(\) \times$ is the operator representing cross product.

As for the second term in the equation (5), we have

$$-J \frac{\partial \mathbf{T}}{\partial \mathbf{X}} = -J \frac{\partial \mathbf{T}}{\partial \mathbf{L}} \cdot \frac{\partial \mathbf{L}}{\partial \mathbf{X}} = k' J \text{diag}\left(\frac{1}{l_{0i}}\right) \mathbf{J}^T = k' J \text{diag}(l_i^{-1}(1 + k'^{-1}t_i)) \mathbf{J}^T \quad \text{for } i=1, \dots, 8 \quad (7)$$

where $k' = EA$,

E is Young's modulus of a wire,

A is the cross section area of a wire,

l_i is the currently measured length of the i^{th} wire,

l_{0i} is the original length of the i^{th} wire.

It is pointed out that the contribution of $k'^{-1}t_i$ to the stiffness of the suspension system can be neglected because it is much less than one. The stiffness of the suspension system consists of two parts, while the first one is mainly influenced by the wire tension and the other one depends on geometrical arrangement of the wires and posture of the aircraft model. Supposing the external wrench F acted on the aircraft model is known, the wire tension in equation (4) can be written as

$$\mathbf{T} = -\mathbf{J}^+ \mathbf{F} + \text{Null}(\mathbf{J}) \boldsymbol{\lambda} \quad (8)$$

where $\mathbf{J}^+ = \mathbf{J}^T (\mathbf{J} \mathbf{J}^T)^{-1} \in \mathbf{R}^{8 \times 6}$ is the Moore-Penrose inverse of matrix \mathbf{J} , $\text{Null}(\mathbf{J}) \in \mathbf{R}^{8 \times 2}$ is a matrix whose columns form a basis for the null-space of matrix \mathbf{J} , $\boldsymbol{\lambda} = [\lambda_1 \ \lambda_2]^T \in \mathbf{R}^{2 \times 1}$ is a column vector of two arbitrary real numbers.

The solution in equation (8) consists of two parts: the first one is the term $-\mathbf{J}^+ \mathbf{F}$, which represents the minimum-norm solution that minimizes the 2-norm $\|\mathbf{T}\|$. The second part $\text{Null}(\mathbf{J}) \boldsymbol{\lambda}$ is an arbitrary vector in the null-space of matrix \mathbf{J} and, affects the distribution of the wire tension without affecting the force and moment at the aircraft model. Equation (5) can be rewritten as

$$\mathbf{K} \approx \mathbf{H} (\mathbf{J}^+ \mathbf{F} - \text{Null}(\mathbf{J}) \boldsymbol{\lambda}) + k' J \text{diag}\left(\frac{1}{l_i}\right) \mathbf{J}^T \quad (9)$$

It is clearly seen that the wire tension can be changed by adjusting the two elements of the column vector $\boldsymbol{\lambda}$, and then the wire tension can make an impact on the stiffness of the system.

4. Dynamic models

4.1 Dynamic Model of the aircraft model

By using Newton-Euler's laws, the motion equations of the aircraft model can be written in the following form

$$\begin{cases} m \ddot{\mathbf{x}} + m \dot{\boldsymbol{\omega}} \times {}^o \mathbf{C} + m \boldsymbol{\omega} \times (\boldsymbol{\omega} \times {}^o \mathbf{C}) = \sum_{i=1}^8 {}^o \mathbf{u}_i t_i + m \mathbf{g} + \mathbf{F}_e \\ m {}^o \mathbf{C} \times \ddot{\mathbf{x}} + \mathbf{I} \dot{\boldsymbol{\omega}} + m (\boldsymbol{\omega} \times {}^o \mathbf{C}) \times \dot{\mathbf{x}} + \boldsymbol{\omega} \times (\mathbf{I} \boldsymbol{\omega}) = \sum_{i=1}^8 {}^o \mathbf{P}_i \times {}^o \mathbf{u}_i t_i + {}^o \mathbf{C} \times m \mathbf{g} + \mathbf{M}_e \end{cases} \quad (10)$$

where $\dot{\mathbf{x}} = [{}^o\dot{x}_o, {}^o\dot{y}_o, {}^o\dot{z}_o]^\top$ represents the linear velocity of the reference point O' of the aircraft model,

$\boldsymbol{\omega} = [\dot{\phi} \ \dot{\beta} \ \dot{\psi}]^\top$ is the angular velocity of the aircraft model,

m is the mass of the aircraft model,

$\mathbf{g} = [0 \ 0 \ g]^\top$ and scalar g is the gravity acceleration,

${}^o\mathbf{C} = {}^o\mathbf{R}_o, {}^o\mathbf{C}$ and ${}^o\mathbf{C}$ is position vector of the center of gravity of the aircraft model in the mobile frame $O'X'Y'Z'$,

$\mathbf{I} = {}^o\mathbf{R}_o, \mathbf{I}_o, {}^o\mathbf{R}_o^\top$ and $\mathbf{I}_o = \begin{bmatrix} I_{XX'} & -I_{XY'} & -I_{XZ'} \\ -I_{YX'} & I_{YY'} & -I_{YZ'} \\ -I_{ZX'} & -I_{ZY'} & I_{ZZ'} \end{bmatrix}$ is the inertia tensor of the aircraft model in

the mobile frame $O'X'Y'Z'$,

\mathbf{F}_e and \mathbf{M}_e are the force and moment exerted by aerodynamic load on the aircraft model.

Equation (10) can be re-written into a compact form as

$$\mathbf{M}(\mathbf{X})\ddot{\mathbf{X}} + \mathbf{N}(\mathbf{X}, \dot{\mathbf{X}})\dot{\mathbf{X}} = \mathbf{W}_e + \mathbf{W}_g + \mathbf{J}\mathbf{T} \quad (11)$$

where $\mathbf{M} = \begin{bmatrix} m\mathbf{I} & -m{}^o\mathbf{C} \times \\ m{}^o\mathbf{C} \times & \mathbf{I} \end{bmatrix}$ and $\mathbf{I} \in \mathbf{R}^{3 \times 3}$ is the identity matrix,

$\mathbf{N} = \begin{bmatrix} \boldsymbol{\theta} & -m(\boldsymbol{\omega} \times {}^o\mathbf{C}) \times \\ m(\boldsymbol{\omega} \times {}^o\mathbf{C}) \times & -\mathbf{I}\boldsymbol{\omega} \end{bmatrix}$ and $\boldsymbol{\theta} \in \mathbf{R}^{3 \times 3}$ is the zero matrix,

$\mathbf{W}_e = \begin{bmatrix} \mathbf{F}_e \\ \mathbf{M}_e \end{bmatrix}$ is the aerodynamic wrench acted on the aircraft model,

$\mathbf{W}_g = \begin{bmatrix} m\mathbf{g} \\ {}^o\mathbf{C} \times m\mathbf{g} \end{bmatrix}$ is the gravity wrench exerted on the reference point O' of the aircraft model,

$\dot{\mathbf{X}} = \begin{bmatrix} \dot{\mathbf{x}} \\ \boldsymbol{\omega} \end{bmatrix}$ is the velocity vector of the aircraft model.

4.2 Dynamic model of the drive units

A drive unit is composed of a motor, a gear reducer and a winch. The dynamic equation of the drive units is given as follows

$$\mathbf{A}\ddot{\boldsymbol{\theta}} + \mathbf{C}\dot{\boldsymbol{\theta}} + \mathbf{r}\mathbf{T} = \boldsymbol{\tau} \quad (12)$$

with $\mathbf{A} = \text{diag}(a_1, a_2, \dots, a_8)$, $a_i = a_{ai} + \frac{a_{wi}}{n^2}$,

$\mathbf{C} = \text{diag}(c_1, c_2, \dots, c_8)$, $c_i = c_{ai} + \frac{c_{wi}}{n}$,

$\mathbf{r} = \text{diag}(r_1, r_2, \dots, r_8)$, $r_i = \frac{r_{wi}}{n}$,

$\boldsymbol{\theta} = [\theta_1 \ \theta_2 \ \dots \ \theta_8]^\top$,

$$\boldsymbol{\tau} = [\tau_1 \ \tau_2 \ \cdots \ \tau_8]^T,$$

where a_{ai} , c_{ai} denote the moment of inertia and the viscous friction coefficient of the i^{th} motor,

a_{wi} , c_{wi} denote the moment of inertia and the viscous friction coefficient of the i^{th} reducer and winch,

r_{wi} is the radius of the i^{th} winch,

n is the reduced ratio of each gear reducer,

θ_i is the rotational angle of the i^{th} motor,

τ_i is the output torque of the i^{th} motor.

4.3 The elastic model of the wires

The relationship between the change of the wire length and the rotational angles of the motors is

$$\boldsymbol{\theta} = \mathbf{r}^{-1} \begin{Bmatrix} \left\| {}^o\mathbf{B}_1 \right\|_2 - \left\| {}^o\mathbf{B}_1 - {}^o\mathbf{P}_o - {}^o\mathbf{R}_o {}^o\mathbf{P}_1 \right\|_2 \\ \vdots \\ \left\| {}^o\mathbf{B}_8 \right\|_2 - \left\| {}^o\mathbf{B}_8 - {}^o\mathbf{P}_o - {}^o\mathbf{R}_o {}^o\mathbf{P}_8 \right\|_2 \end{Bmatrix} \quad (13)$$

Successive time derivatives of equation (13) yield

$$\dot{\boldsymbol{\theta}} = \frac{\partial \boldsymbol{\theta}}{\partial \mathbf{X}} \dot{\mathbf{X}} = \frac{\partial \boldsymbol{\theta}}{\partial \mathbf{l}} \frac{\partial \mathbf{l}}{\partial \mathbf{X}} \dot{\mathbf{X}} = \mathbf{r}^{-1} \mathbf{J}^T \dot{\mathbf{X}} \quad (14)$$

$$\ddot{\boldsymbol{\theta}} = \mathbf{r}^{-1} \dot{\mathbf{J}}^T \dot{\mathbf{X}} + \mathbf{r}^{-1} \mathbf{J}^T \ddot{\mathbf{X}} \quad (15)$$

The elasticity of the wires must be taken into account in order to increase motion control accuracy. The longitudinal deformation of a wire can be given by

$$\Delta l_i = \frac{l_i^l \theta_i}{EA} \quad (16)$$

Then the stiffness of a wire is $k_i = \frac{EA}{l_{0i}} = \frac{EA}{l_i(1 - \Delta l_i/l_i)}$. To summarize, Equations (11), (12), (13),

(14) and (15) represent the dynamic model of the suspension system in wind tunnel.

5. Control scheme

The dynamic model of the flexible suspension system in wind tunnels is a highly-coupled and nonlinear system, and the actuation redundancy makes the system over-restrained. In designing the control scheme, it is necessary to decouple and linearize the dynamic model. A computed torque controller in joint space is employed for the flexible suspension system in wind tunnels. Because the actuation redundancy introduces multiple wire tension solutions, an optimal tension distribution method is applied to obtain certain acceptable solutions. When the air flow passes through the aircraft model in wind tunnel tests, a wind pressure will be exerted on the aircraft model. According to the aerodynamic theory, drag

force in along-wind direction, lift force in crosswind direction and pitching moment are applied on the model under the condition that the wind load is symmetrical. The wind load make the model fail to keep the desired position and orientation. Thus, it is challenging to obtain the accurate mapping relation between the measured value of the aerodynamics and the position and orientation of the craft model. Consequently, it is desired to enhance the stiffness in the three directions by commanding the wire tensions. Further more, by introducing the dynamical compensation on the basis of conventional PD control, the revised feedforward PD control law based on the stiffness enhancement principles. As shown in Fig. 3, the control law consisting of inverse dynamics feedforward and feedback loop is employed to control the driving torque of the actuators.

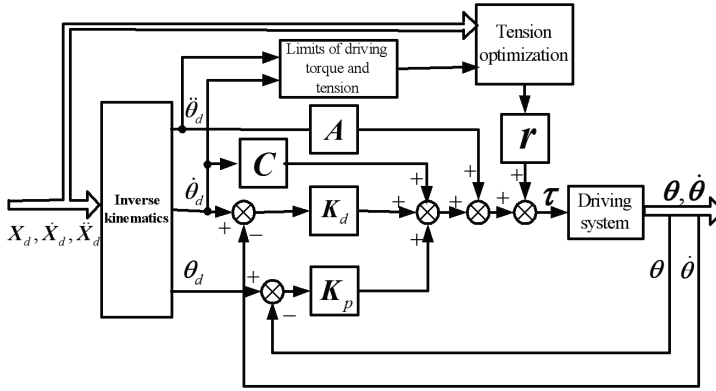


Fig. 3. Control scheme for wire-driven parallel support system for wind tunnels

The revised PD feedforward control law is

$$\tau = A\ddot{\theta}_d + C\dot{\theta}_d + rT_d + K_p(\theta_d - \theta) + K_d(\dot{\theta}_d - \dot{\theta}) \quad (17)$$

where, K_p, K_d are feedback gain matrices. T_d is the desired tension. Error $e = \theta - \theta_d$. If the desired angular velocity $\dot{\theta}_d$, angular acceleration $\ddot{\theta}_d$ and tension T_d are all boundary values, Eq.(17) can make e and \dot{e} exponentially converge to the closed sphere of radius r_i . Provided the desired trajectory X_d of the aircraft model, the desired angle, angular velocity and angular acceleration of the driving motors can be solved for by using inverse kinematics and the elastic deformation Eq.(16).

$$T_d = \bar{T}_d + \text{Null}(J)\lambda \quad (18)$$

$$\bar{T}_d = J^+(M(X_d)\ddot{X}_d + N(X_d, \dot{X}_d)\dot{X}_d - W_g) \quad (19)$$

where \bar{T}_d is the minimal norm solution. Null is the null space vector. The restrictions for single wire and the torque of the motors are $\tau_{\max} \geq \tau_i \geq \tau_{\min}$, where t_{\max} is the maximum permissive tension of the wire, and t_{\min} is the minimum tension of the wire in case of the pseudo drag. τ_{\max} and τ_{\min} are the maximum and minimum output torque, respectively. Further, we can obtain

$$\boldsymbol{\varphi} \geq \mathbf{T} \geq \boldsymbol{\eta} \quad (20)$$

where, $\varphi_i = \min\{t_{\max}, (\tau_{\max} - a_i \ddot{\theta}_{id} - c_i \dot{\theta}_{id})/r_i\}$, $\eta_i = \max\{t_{\min}, (\tau_{\min} - a_i \ddot{\theta}_{id} - c_i \dot{\theta}_{id})/r_i\}$,

$$\boldsymbol{\varphi} = [\varphi_1 \ \cdots \ \varphi_8]^T, \quad \boldsymbol{\eta} = [\eta_1 \ \cdots \ \eta_8]^T.$$

For redundant driving system, an optimization is needed to solve for the tensions of the wires. Generally, the tension minimization principle is used in the optimization (Müller, 2005). That is to say $\mathbf{T}_d^T \mathbf{W} \mathbf{T}_d$ and \mathbf{W} are the summing weights factor matrices. However, since this parallel robot is applied in wind tunnel, the aircraft model tends to deviate from desired position and orientation and results in experimental errors. Consequently, in order to obtain more precise experimental data, it is necessary to enhance the stiffness by adjusting wire tension. Taking account of constrains of the motor output and wire material properties, the objective of the optimization is to maximize the stiffness weight-sum in the three principal directions of forces or torques.

$$\begin{aligned} \text{find } \boldsymbol{\lambda} &= [\lambda_1 \ \lambda_2]^T \\ \text{max } & \text{sum}(K_{XX}^{g_1}, K_{ZZ}^{g_2}, K_{\beta\beta}^{g_3}) \\ \text{s.t. } & \boldsymbol{\varphi}(\dot{\boldsymbol{\theta}}_d, \ddot{\boldsymbol{\theta}}_d) - \bar{\mathbf{T}}_d \geq \text{Null}(\mathbf{J})\boldsymbol{\lambda} \geq \boldsymbol{\eta}(\dot{\boldsymbol{\theta}}_d, \ddot{\boldsymbol{\theta}}_d) - \bar{\mathbf{T}}_d \end{aligned} \quad (21)$$

Given the desired trajectory of the aircraft model \mathbf{X}_d , $\bar{\mathbf{T}}_d$, $\boldsymbol{\varphi}(\dot{\boldsymbol{\theta}}_d, \ddot{\boldsymbol{\theta}}_d)$ and $\boldsymbol{\eta}(\dot{\boldsymbol{\theta}}_d, \ddot{\boldsymbol{\theta}}_d)$ can be solved from Eq. (19) and (20). The translational stiffness in X direction is $K_{XX} = \mathbf{K}_{1,1} =$

$$k \sum_{i=1}^8 \frac{u_{i,1}^2}{l_i} + \sum_{i=1}^8 -\frac{1}{l_i} (\bar{\mathbf{T}}_{d,i} + \lambda_1 \text{Null}(\mathbf{J})_{i,1} + \lambda_2 \text{Null}(\mathbf{J})_{i,2}). \quad \text{That in Z direction is}$$

$$K_{ZZ} = \mathbf{K}_{3,3} = k \sum_{i=1}^8 \frac{u_{i,3}^2}{l_i} + \sum_{i=1}^8 -\frac{1}{l_i} (\bar{\mathbf{T}}_{d,i} + \lambda_1 \text{Null}(\mathbf{J})_{i,1} + \lambda_2 \text{Null}(\mathbf{J})_{i,2}). \quad \text{The stiffness in the pitching}$$

$$\text{direction is } K_{\beta\beta} = \mathbf{K}_{5,5} = \sum_{i=1}^8 \frac{[({}^o\mathbf{L}_i \times [({}^o\mathbf{R}_o, {}^o\mathbf{P}_i) \times] - [({}^o\mathbf{R}_o, {}^o\mathbf{P}_i) \times] [{}^o\mathbf{P}_i \times])_{2,2} (\bar{\mathbf{T}}_{d,i} + \lambda_1 \text{Null}(\mathbf{J})_{i,1}$$

$$+ \lambda_2 \text{Null}(\mathbf{J})_{i,2}) + k \sum_{i=1}^8 \frac{({}^o\mathbf{P}_i \times {}^o\mathbf{u}_i)_2^2}{l_i}. \quad \text{The subscript indicates the row element of a vector or the}$$

element of a matrix. For the dimensionally generalized K_{XX} , K_{ZZ} and $K_{\beta\beta}$, the objective function is derived by weighting sum. And the weight sum factors g_1 , g_2 and g_3 are determined according to the desired trajectory and index of the experiment. The optimization objective is the linear function of λ_1 and λ_2 , while the constraint function constitutes two-dimensional convex set of λ_1 and λ_2 .

For this kind of linear program problem, the simplex search method is generally employed to solve the solution. But the solving course is very time consuming. To improve the computation speed, a new algorithm is designed as follow.

Step 1: Determining the initial solution. There are sixteen linear inequality constrains in Eq.(21). Any three can be picked out and converted into equality constrains. Then the three line equation related to λ_1 and λ_2 from the geometry point of view is obtained. The three intersection points of the three lines can be solved. Then whether the three intersection points

satisfy the rest thirteen inequalities is checked. If so, the three intersection points generate the initial solution by forming a convex combination. If not, another selection is needed.

Step 2: Determining the searching direction. Taking the initial solution obtained in Step 1 as the start point. Along the gradient and negative gradient direction of the objective function forward search step are conducted, respectively. Then the new two candidates are evaluated with respect to the objective function. The direction relating to the better candidate is taken as the searching direction. So, this optimization becomes a one dimensional optimization.

Step 3: Along the searching direction search is conducted forward with larger step until exceeds the feasible region. Then the dichotomy is used between the outer and inner points of the feasible region until the optimal point on the boundary of the feasible region is obtained.

Step 4: In order to maintain the continuity of the wire tension, a judgment of the tension vector is conducted. In which, whether the tension T_i of the current position and orientation and T_{i-1} of the previous position and orientation satisfy $\|T_i - T_{i-1}\|_{\infty} \leq \varepsilon$ is judged, where ε is the threshold. If it is satisfied, the optimal solution is obtained. If it is not satisfied, starting with the current solution, along with the positive searching direction the optimization is moved back to the feasible region and the inferior solution is obtained. And the optimization goes to Step 1.

6. Simulated results

In order to validate the proposed algorithm in this research, simulations aiming at the revised PD feedforward controller based on the stiffness enhancement are conducted. Moreover, a comparison between that of a revised PD controller based on tension minimization is carried out.

The position of the joints and pulley of the robot is shown in Table 1. The wire is chosen from reference (Zheng, 2004), which is made of extra strong polyethylene fibre. The diameter $A = 1\text{mm}$ and the Young's modulus is $E = 120\text{GPa}$. The unit stiffness of the wire is $k' = 94247\text{N}$. The maximum elastic tension is $t_{\max} = 1200\text{N}$. The preset minimum pretension is $t_{\min} = 10\text{N}$. The rating output torque of the motors is $\tau_{\max} = 15.8\text{N}\cdot\text{m}$, $\tau_{\min} = -15.8\text{N}\cdot\text{m}$. The equivalent moment of inertia on the shaft of the motors is $7.52 \times 10^{-4}\text{kg}\cdot\text{m}^2$. The equivalent viscosity coefficient on the shaft of the motors is $1.88 \times 10^{-4}\text{N}\cdot\text{m}\cdot\text{s}$. The radius of the wrench is $r_{wi} = 0.04\text{m}$. The ratio of the reducer is 4:1. The scale model is the 1/18 wooden aircraft model referred to in (Liu et al, 2005). The aircraft has a length of 713mm and wing width of 510mm. The height is 107mm and the weight is 10.5N. In the local frame, the inertial tensor is

$$I_o = \begin{bmatrix} 1.0726 \times 10^{-2} & 0 & -1.8748 \times 10^{-9} \\ 0 & 2.8409 \times 10^{-2} & 1.578 \times 10^{-4} \\ -1.8748 \times 10^{-9} & 1.578 \times 10^{-4} & 3.8985 \times 10^{-2} \end{bmatrix} \text{kg}\cdot\text{m}^2$$

In the experiment, the stable wind with the velocity of 30m/s is applied. Considering the real-time measured data, the equivalent of load force of the wind is generated in MATLAB. The position of the aircraft is ${}^oP_o = (0 \ 0 \ 420)^T \text{mm}$ and its pitch angle varies according to the

following parameter. The desired angle trajectory is $\beta_d = \pi/30 - \omega_\beta t$ and angular velocity is $\omega_\beta = \pi/45$ rad/s, $0 \leq t \leq 4$ s. In order to achieve the precision of the positioning and pitching, the weight factor is $g_1 = 0.3$, $g_2 = 0.3$ and $g_3 = 0.4$. The simulation is conducted employing the fourth order Runge-Kutta method. The sampling time is 0.01s. The PD parameters are determined by both extension critical proportion and manual adjusting method. $K_p = \text{diag}(10,10,5.5,5.5,5.5,5.5,5.5,5.5)$, $K_d = \text{diag}(0.25,0.25,0.15,0.15, 0.15,0.15,0.15,0.15)$.

Indication	Coordinates(in mm)
${}^oP_1({}^oP_3, {}^oP_7)$	$(-438 \ 0 \ 0)^T$
${}^oP_2({}^oP_4, {}^oP_8)$	$(275 \ 0 \ 0)^T$
oP_5	$(0 \ -255 \ 0)^T$
oP_6	$(0 \ 255 \ 0)^T$
oC	$(-25 \ 0 \ 0)^T$
${}^oB_1({}^oB_2)$	$(0 \ 0 \ 0)^T$
${}^oB_3({}^oB_4)$	$(0 \ -605 \ 420)^T$
${}^oB_5({}^oB_6)$	$(0 \ 0 \ 840)^T$
${}^oB_7({}^oB_8)$	$(0 \ 605 \ 420)^T$

Table 1. Location of the joints and pulleys

Figs. 4 and 5 show the wire tension based on the stiffness optimization principle and the wind load variation in three directions in the process of adjusting the orientation of the model. Figs 6 and 7 show the wire tension based on the minimum tension principle and the variation of the stiffness in three directions. Fig 8 shows the actual variation curve of the pitch angle in the cases of the two principles. Fig 9 makes a comparison of the positioning error of the aircraft model in X and Z directions.

As the figures show, the wire tension with the stiffness optimization principle varies evenly. The pitching stiffness $K_{\beta\beta}$ ranges from 8300 to 8700 Nm/rad. The pitch angle error is less than 0.039 rad, and its RMS is 0.0157 rad. The positioning error in X direction is less than 0.0111m, and its RMS is 0.0057m. The positioning error is less than 0.013m, and its RMS is 0.0041m.

Under the condition of minimum wire tension principle, the wire tension is small and varies evenly. The pitching stiffness ranges from 7600 to 8000 Nm/rad. The pitching angle error is less than 0.0619 rad, and its RMS is 0.0229rad. The positioning error in X direction is less than 0.0185m, and its RMS is 0.0076m. The positioning error in Z direction is less than 0.0178m and the RMS is 0.005m.

Though the wire tension based on optimal stiffness principle tends to be large, compared with that of minimum tension principle the pitching stiffness increases from about 7600-8000 Nm/rad to about 8300 - 8700Nm/rad. The RMS of the pitch angle error decreases by 31.44%. The RMS of the positioning error in X direction decreases by 25%, and that in Z direction decreases by 18. The control precision has been improved drastically.

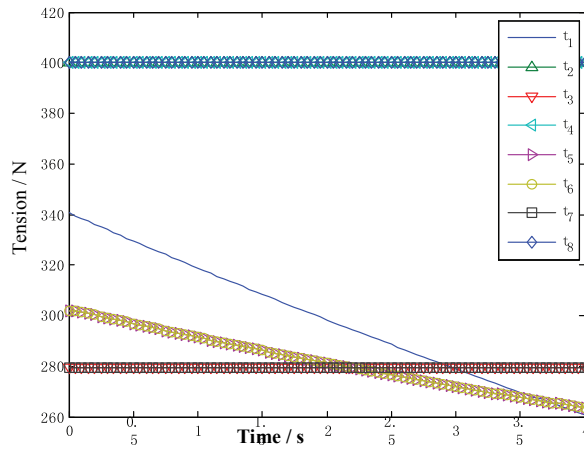


Fig. 4. Optimum tension distribution based on the stiffness enhancement criteria

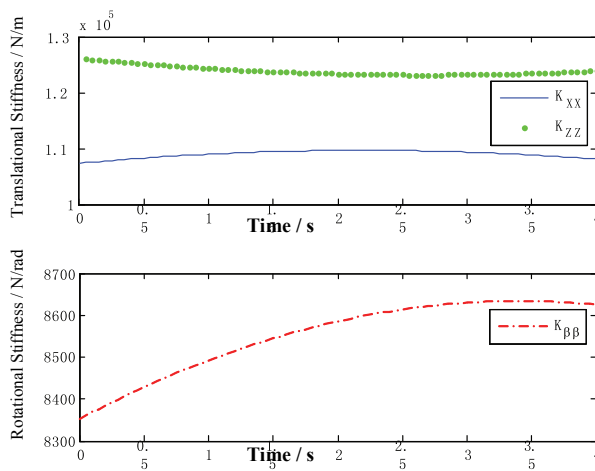


Fig. 5. Stiffness values obtained by the stiffness enhancement criteria

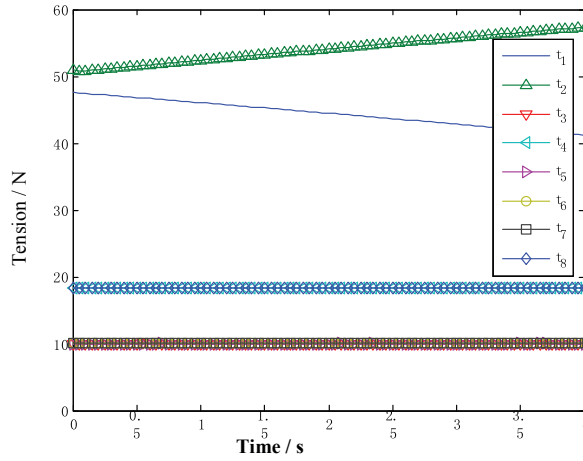


Fig. 6. Optimum tension distribution based on the minimum tension criteria

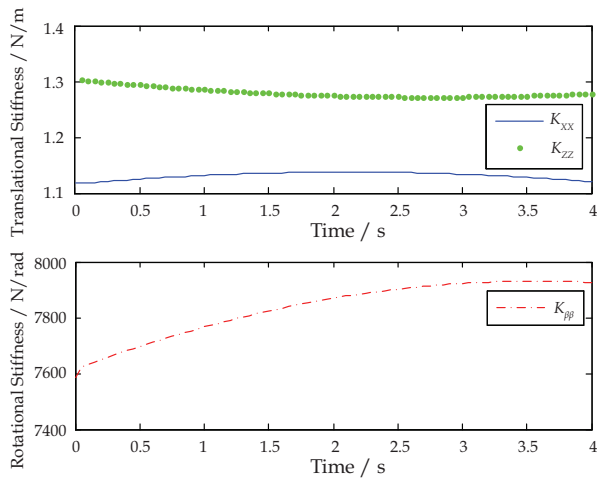


Fig. 7. Stiffness values obtained by the minimum tension criteria

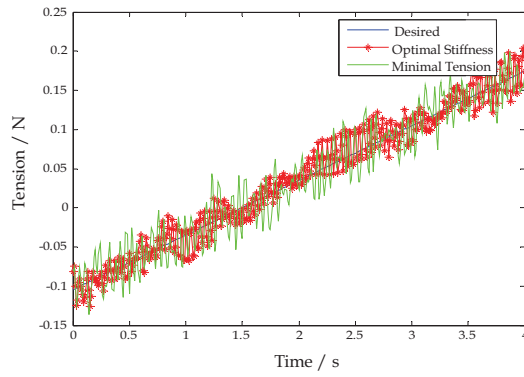


Fig. 8. Pitch angle vs time

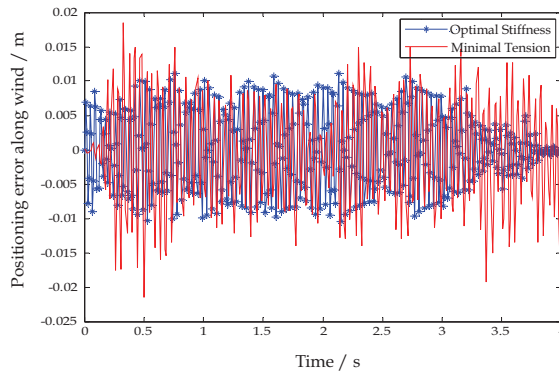


Fig. 9. Position error of the aircraft model at along-wind direction

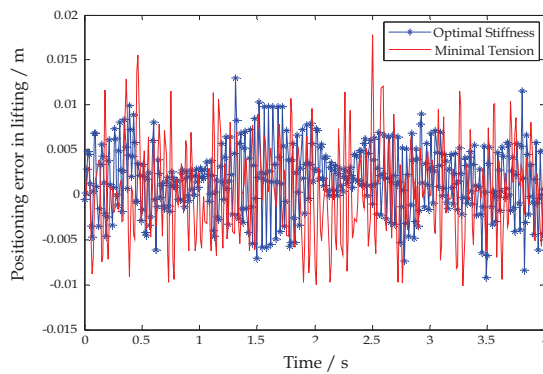


Fig. 10. Pitch angle vs time

7. Conclusions

Firstly, the stiffness of the six-degree-of-freedom redundant wire driven parallel manipulator is dealt with in this paper. The analytical expression of the stiffness is developed, in which the stiffness consists of two parts. The former part is related to the wire tension, while the latter one depends mainly on both the geometry distribution of the wires and the orientation of the end-effector.

Secondly, the dynamical models of the aircraft and the driving system are deduced, respectively. Considering the motor output and wire material properties, the wire tension optimization is conducted in order to improve the stiffness in three principal directions. This method solves the indefinite problem of the wires tension introduced by the redundancy.

Thirdly, aiming at the nonlinearity, strong coupling and air current loaded environment of the wire driven system, the revised PD feed forward controller in joint space based on stiffness enhancement principle is developed. Compared with the revised PD feed forward controller based on minimum wire tension principle, the control scheme proposed in this paper improves the dynamical positioning precision of the aircraft.

8. Acknowledgment

Grateful acknowledgment is made to Prof. Liu Xiongwei and Dr. Zheng Yaqing. The authors would like to appreciate the Editor, Associate Editors, and the reviewers for their valuable comments and suggestions.

9. References

- Albus, J.; Bostelman, R. & Dagalakis, N. (1993). The NIST robocrane. *Journal of Robotic Systems*, vol. 10, no. 5, pp. 709-724,
- Behzadipour, S. & Khajepour, A. (2006). Stiffness of cable-based parallel manipulators with application to stability analysis. *Journal of Mechanical Design*, vol. 128, no. 1, pp. 303-310.
- Chen, Q.; Wang, Y. & Chen, H. (2003). Comparative research of trajectory tracking performance of robotic manipulator based on PD control scheme. *Control and Decision*, vol. 18, no. 1, pp. 53-57.
- Dekker, R.; Khajepour, A. & Behzadipour, S. (2006). Design and testing of an ultra-high-speed cable robot. *International Journal of Robotics and Automation*, vol. 21, no. 1, pp. 25-33.
- Duan, B.Y. (1999). A new design project of the line feed structure for large spherical radio telescope and its nonlinear dynamic analysis. *Mechatronics*, vol. 9, no. 1, pp. 53-64.
- Hithoshi, K.; Toshiaki, Y. & Fumiaki, T. et al. (2007). Robust PD control using adaptive compensation for completely restrained parallel-wire driven robots: translational systems using the minimum number of wires under zero-gravity condition. *IEEE Transactions on Robotics*, vol. 23, no. 4, pp. 803-812, 2007.
- Lafourcade, P.; Llibre, M. & Reboulet, C. (2002). Design of a parallel wire-driven manipulator for wind tunnels. *Proceedings of the workshop on Fundamental Issues and Future Research Directions for Parallel Mechanisms and Manipulators*. pp. 187-194. , October 2002, Quebec City, Quebec, Canada,

- Lafourcade, P. (2004). Etude de manipulateurs parallel cables, conception d'une suspension active pour souffleria, Dissertation of ENSAE.
- Liu, X.; Zheng Y. & Lin, Q. (2004). Overview of wire-driven parallel kinematic manipulators for aircraft wind tunnels. *Acta Aeronautica et Astronautica Sinica*, vol. 25, no. 4, pp. 393-400.
- Liu, X. Qi Y. &, Agyemang, B. et al (2006). Design wire-driven parallel suspension system for wind tunnel based virtual flight testing. *Proceedings of the 7th International Conference on Frontiers of Design and Manufacturing*, pp. 7-12, Guangzhou, China, June 2006.
- Ma, O. & Diao, X. (2005). Dynamics analysis of a cable-driven parallel manipulator for hardware-in-the-loop dynamic simulation. *Proceedings of the 2005 IEEE/ASME International Conference on Advanced Intelligent Mechatronics*. pp. 837-842 , July 2005, Monterey, California, USA
- Ming, A. & Higuchi, T. (1994). Study on multiple degree of freedom positioning mechanisms using wires. Part 1: concept, design and control. *International Journal of the Japan society for Precision Engineering*, vol. 28, no. 2, pp. 131-138.
- Müller, A. (2005). Internal preload control of redundantly actuated parallel manipulators-its application to backlash avoiding control. *IEEE Transactions on Robotics*, vol. 21, no. 4, pp. 668-677.
- Ning, K.; Zhao, M. & Liu, J. (2006). A new wire-driven three degree-of-freedom parallel manipulator. *Journal of Manufacturing Science and Engineering*, vol. 128, no. 3, pp. 816-819.
- Yamamoto, M.; Yanai, N. & Mohri, A. (2004). Trajectory control of incompletely restrained parallel-wire-suspended mechanism based on inverse dynamics. *IEEE Transactions on Robotics*, vol. 20, no. 5, pp. 840-850.
- Yu, K. (2008). Simultaneous trajectory tracking and stiffness control of cable driven parallel manipulator. Dissertation of State University of New York.
- Zheng, Y. (2004). Research on key theoretical issues of wire-driven parallel kinematic manipulators and the application to wind tunnel support systems. Dissertation of Huaqiao University.
- Zheng Y.; Lin, Q. & Liu, X. (2005). Design methodology of wire-driven parallel support systems in the low speed wind tunnels and attitude control scheme of the scale model, *Acta Aeronautica et Astronautica Sinica*, vol. 26, no. 6, pp. 774-778.
- Zi, B.; Duan, B. Y. & Du, J. L. et al. (2008). Dynamic modeling and active control of a cable-suspended parallel robot. *Mechatronics*, vol. 18, no. 1, pp. 1-12.

Rebuilding and Analysis of a SCIROCCO PWT Test on a Large TPS Demonstrator

Sara Di Benedetto, Giuseppe C. Rufolo, Marco Marini and Eduardo Trifoni
*CIRA, Italian Aerospace Research Centre
Italy*

1. Introduction

In September 2007, a Plasma Wind Tunnel (PWT) Test was performed in the CIRA SCIROCCO facility on the FLPP Snecma Propulsion Solide (SPS) Thermal Protection System (TPS) demonstrator (Barreteau et al., 2008). Aim of the test was to verify, in a space qualifying environment, the behaviour of a large assembly constituted by Ceramic Matrix Composite (CMC) shingles, one curved and two flat panels, the same elements which will be part of the next ESA Intermediate Experimental Vehicle (IXV) thermal protection system. The focus of this chapter is the description of the CFD activities carried out in order to realize and support the plasma wind tunnel test, both in the phase of test definition and for the post test analysis.

During the pre-test CFD activity the test condition, previously defined by a simplified two dimensional methodology (Rufolo et al., 2008), has been verified by means of three dimensional simulations, and the final PWT test condition has been defined. Then, the post-test CFD rebuilding activity has allowed the analysis of results and the comparison with experimental measurements.

In addition, an assessment of the uncertainty level related to the satisfaction of the test requirements, in terms of heat flux and pressure to be realized over the test article, has been provided by analyzing the sources of error linked to both design and testing phases.

2. Test requirements

The test article is an assembly of CMC TPS elements: two flat panels located at 45 degrees with respect to the plasma flow and a curved panel which constitutes the model leading edge.

The test article configuration and its dimensions are represented in Fig. 1. Each portion of TPS to be tested (in white in figure) is separated by the other ones by a gap (1.5 mm in depth and 3 mm in width), in such a way to form a “T-gap” configuration.

The initial test design phase had been carried out in order to answer to the following customer requirements:

- cold-wall ($T_w=300$ K), fully catalytic heat flux of $320 \text{ kW/m}^2 \pm 10\%$ at the beginning of the flat panels;
- constant wall pressure of 25 mbar_a maintained during the test on the two flat panels surface.

Moreover, the test article leading edge (curved panel) should not have been submitted, during the test, to a heat flux exceeding the value of 700 kW/m^2 .

At the end of the test design activity (Rufolo et al., 2008), the PWT operating condition allowing the complete fulfilment of above requirements had resulted to be, in terms of facility reservoir conditions, $P_0=5.2 \text{ bar}_a$ and $H_0=16.7 \text{ MJ/kg}$, realized with the SCIROCCO conical nozzle D, characterised by a 1.15 m nozzle exit diameter, and with the model stagnation point located 0.35 m downstream of the nozzle exit section.

The achievement of the desired operating condition (P_0 , H_0) in test chamber is assured by the measurements of stagnation heat flux and pressure on a water cooled copper probe. The stagnation values corresponding to the reservoir conditions above, and determined by CFD during the test design phase, were: $P_s=36.15 \text{ mbar}_a$ and $Q_s=2070 \text{ kW/m}^2$.

A complete description of the SCIROCCO facility is given in the following section.

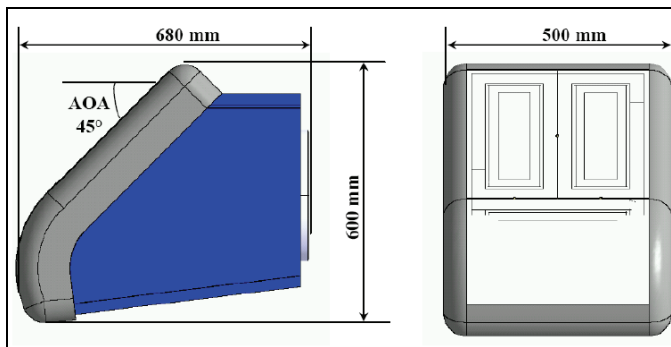


Fig. 1. Test article geometry

3. SCIROCCO plasma wind tunnel

The CIRA SCIROCCO Plasma Wind Tunnel (Marini et al., 2002 and De Filippis et al., 2003) is devoted to aerothermodynamic tests on components of aerospace vehicles; its primary mission is to simulate the thermo-fluid-dynamic conditions suffered by full scale Thermal Protection System (TPS) of space vehicles re-entering the Earth atmosphere.

SCIROCCO is a large size facility (see Fig.2), whose hypersonic jet impacts the test article with a diameter size up to 2 m and reaches Mach number values up to 11. The jet is then collected by a long diffuser (50 m) and cooled by an heat exchanger. Seventy MW electrical power is used to heat the compressed air that expands along a converging-diverging conical nozzle. Four different nozzle exit diameters are available: 0.9, 1.15, 1.35 and 1.95 m, respectively named C, D, E and F.

The overall performance of SCIROCCO in terms of reservoir conditions is the following: total pressure (P_0) varies from 1 to 17 bar and total enthalpy (H_0) varies from 2.5 to 45 MJ/kg. Enthalpy values between 2.5 and 10 MJ/kg are obtained using a plenum chamber between the arc heater column exit and the nozzle inlet converging part, which allows transverse injection of high pressure ambient air to reduce the flow total enthalpy.

The energetic heart of the facility is the segmented constricted arc heater, a column with a maximum length of 5.5 m and a bore diameter of 0.11 m. At the extremities of this column there are the cathode and the anode between which the electrical arc is generated. A power



Fig. 2. SCIROCCO Plasma Wind Tunnel aerial view

supply feeds the electrical DC power to the electrodes for the discharge. A compressed air supply distributes dry compressed air to the various segments of the arc heater column, being able to supply a mass flow rate ranging from 0.1 to 3.5 kg/s, heated up to 10000 K. The last important subsystem of SCIROCCO is the vacuum system, which generates the vacuum conditions in test chamber required by each test. The system consists of ejectors that make use of high pressure water steam as motor fluid (28.5 bar_g and 250 °C). Facility theoretical performance map in terms of reservoir conditions produced by the arc heater is shown in Fig. 3.

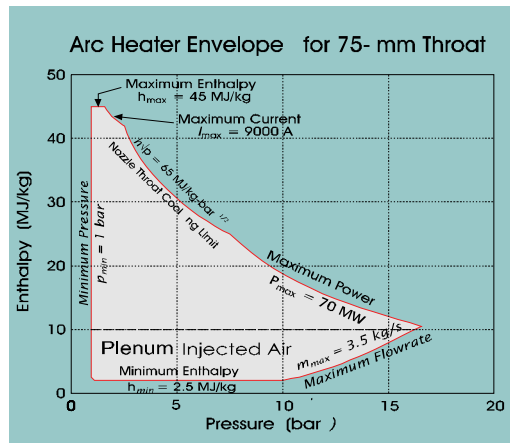


Fig. 3. Arc heater theoretical performance map

The achievement of the desired operating conditions (P_0 , H_0) in test chamber before the insertion of the model is assured by the measurements of stagnation pressure (P_s) and stagnation heat flux (Q_s) radial profiles on a 100mm-diameter hemi-spherical calibration probe, made of copper and water cooled, at a section 0.375 m downstream of the conical nozzle exit section, by means of high precision pressure transducers and Gardon-Gage heat flux sensors, respectively. Facility regulations (mass flow, current) are tuned in order to measure on the calibration probe a certain couple of values (P_s , Q_s) which corresponds to the desired set point in terms of the couple (P_0 , H_0).

4. Numerical methodology

4.1 Numerical tool

All the three-dimensional numerical computations presented in this chapter have been performed by using the CIRA CFD code H3NS.

H3NS is a structured multi-block finite volume solver that allows for the treatment of a wide range of compressible fluid dynamic problems, and has been widely validated in the past (Ranuzzi & Borreca, 2006), (Di Clemente, 2008).

It solves the full Navier-Stokes equations for a real gas in thermal and chemical non-equilibrium conditions. The governing equations, written in conservation form, are discretized by using a finite volume technique with a centred formulation; the inviscid fluxes are computed by means of a Flux Difference Splitting (FDS) Riemann solver, with a second order ENO reconstruction of interface values, whereas viscous fluxes are calculated by central differencing, i.e. computing the gradients of flow variables at cell interfaces by means of the Gauss theorem. Time integration is performed with an explicit Euler forward algorithm and a Local Time Stepping formulation, coupled with a point-implicit evaluation of chemistry and vibrational source terms.

In the case of thermo-chemical non equilibrium flows the fluid is treated as a mixture of perfect gases. The chemical model for air is due to Park (Park, 1989) and it is characterized by 17 reactions between the five species (O, N, NO, O₂, N₂), neglecting the presence of inert gas or water in the air. The energy exchange between vibrational and translational modes is modeled with the classical Landau-Teller non-equilibrium equation, with relaxation times taken from the Millikan-White theory (Millikan & White, 1963) modified by Park (Park & Lee, 1993). The viscosity of the single species is evaluated by a fit of collision integrals calculated by Yun and Mason (Yun & Mason, 1962); the thermal conductivity is calculated by means of the Eucken law; the viscosity and thermal conductivity of the gas mixture are then calculated with the semi-empirical Wilke's formulae. The diffusion of the multi-component gas is computed through a sum rule of the binary diffusivities of each couple of species (Kee et al., 1983). Transport coefficients, assuming ideal gas, are derived from Sutherland's law.

Several models for the treatment of finite rate catalysis are implemented both considering a constant recombination coefficient and *ad hoc* developed model for TPS materials (e.g. Di Benedetto & Bruno, 2010).

4.2 Three-dimensional computational grid

The three-dimensional computational grid around the test article has been generated by means of the commercial software ANSYS ICEMCFD®.

Grid, composed of hexahedral elements, has been generated for half model using a multiblock approach, and has been stretched normally to wall surfaces in order to properly predict the different boundary layers developing around the geometric configuration. The topology of the grid has been created in order to accurately define all the geometric details of test article and obtained by using a certain number of O-grids (Fig. 4) for the block decomposition.

The computational grid on the full test article is shown in Fig. 5, while an enlargement of top frame is depicted in Fig. 6.

Within the main O-grid containing the body, two O-grids have been generated around the curved and flat panel, respectively; in this way it is possible to keep down the overall number of grid points still preserving a good discretization of the gaps (see Fig. 7).

It must be underlined that these gaps have been modelled with sharp edges (a measure of local curvature radii was not available), therefore results in terms of heat flux peaks are conservative.

Moreover, the bow shock wave surface has been properly fitted. In order to minimize the numerical instabilities that propagate from the shock wave towards the stagnation region (the “carbuncle” phenomenon), it is important to align as much as possible the grid lines to the shock.

Grid characteristics are listed in Tab. 1, Δn_{min} being the minimum spacing normal to the wall at the stagnation point and AR the corresponding aspect ratio. Three grid levels have been adopted, in order to assure grid convergence of results, as it will be shown in Section 5.2.

Grid Level	Cells	Δn_{min}	AR
<i>coarse</i>	32468	$7 \cdot 10^{-6}$ m	2500
<i>medium</i>	259744	$2 \cdot 10^{-6}$ m	4050
<i>fine</i>	2077952	$1 \cdot 10^{-6}$ m	4410

Table 1. Computational grid characteristics

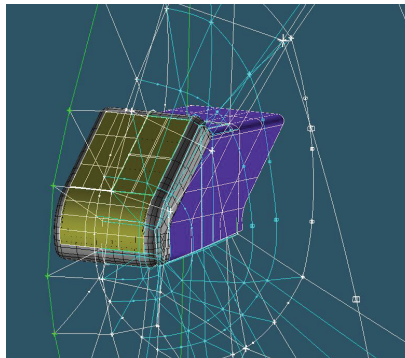


Fig. 4. Block decomposition

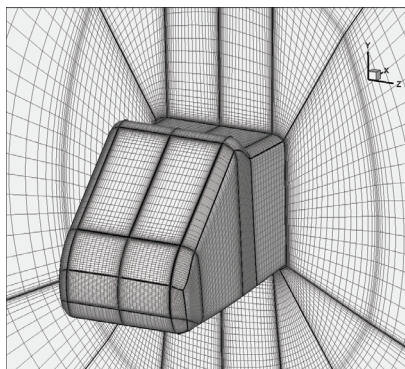


Fig. 5. Three dimensional computational grid

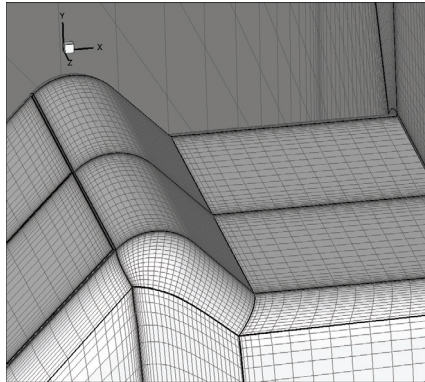


Fig. 6. Detail of the top frame

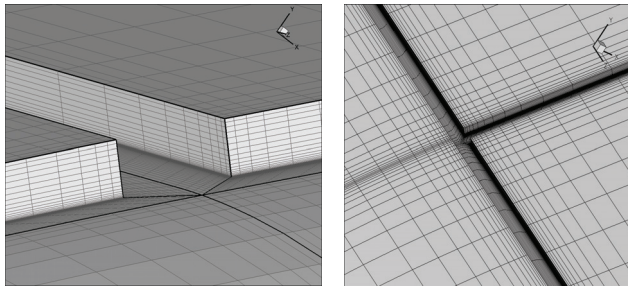


Fig. 7. Gap between panels and frame (left) and T gap (right)

5. Pre Test CFD activity

In this section CFD three dimensional results of the flow field computed around the test article are shown and deeply analyzed for the PWT condition selected during the test design phase (Rufolo et al., 2008), i.e. $\dot{P}_s=36.15 \text{ mbar}_a$ and $Q_s=2070 \text{ kW/m}^2$. Subsequently, grid convergence of results will be shown in Section 5.2, and an assessment of the uncertainty level linked to both design and testing phases will be presented in Section 5.3.

5.1 Three-dimensional results and test requirements verification

Three-dimensional computations on the full test article configuration have been performed with the aim at verifying the test requirements fulfilment with the PWT condition defined. Moreover, information about flow features (presence of vortex structures, separation and reattachment lines, overheatings induced by the gaps, etc.) and spanwise effects will be given in the following, in order to exactly account for the overheatings predicted on the lateral parts of the CMC panels.

The computation has been performed for half model and in the hypothesis of cold ($T_w=300 \text{ K}$) and fully catalytic wall, as requested by SPS at the end of the test design phase.

Mach number and pressure contour maps are shown in Fig. 8. The shape of the bow shock around the model is clearly predicted as well as the stagnation pressure region (on the curved panel), the constant pressure region on the model flat panel and the strong

expansions occurring in correspondence of the roundings, either on the top frame either on the lateral fairings.

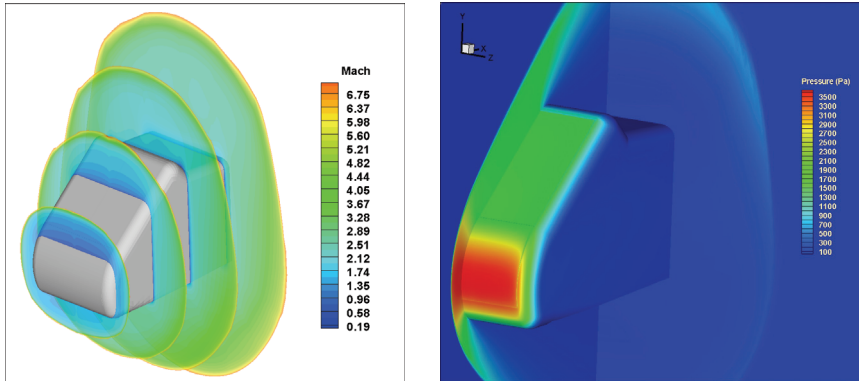


Fig. 8. Mach number around the model (left) and pressure contour map (right)

The first verification has concerned with the possibility of wind tunnel blockage occurrence due to the large size and bluntness of the FLPP-SPS model. As shown in Fig. 9, where the computed two-dimensional and three-dimensional bow shock shapes in the model centre plane are reported, evident finite span effects are present for this test article which make the bow shock closer to the TPS demonstrator with respect to the design solution.

The reason is the spanwise flow induced by the strong transversal pressure gradient, due to the 45 deg inclination of the panels with respect to the free stream.

Fig. 10 shows the model with its bow shock wave inside the test chamber and in front of the diffuser entrance, at the position of 0.35 m downstream of the nozzle exit section. It is evident that the bow shock wave is fully swallowed by the diffuser pick-up.

This occurrence constitutes a necessary condition to be verified in order to exclude the risk of wind tunnel blockage.

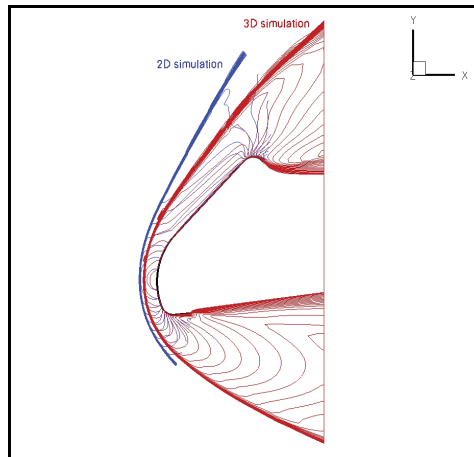


Fig. 9. Bow shock in the symmetry plane

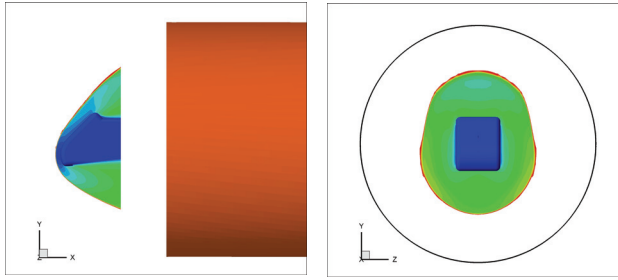


Fig. 10. Side (left) and front (right) view of the model with its bow shock ahead the diffuser entrance

Fig. 11 shows the heat flux distribution predicted on the full model together with the skin-friction lines pattern (the solution on half model has been mirrored with respect to the symmetry plane).

The stagnation line on the curved panel and the local maximum values of heat flux (less than 1 MW/m^2) at the roundings of the lateral fairings of the curved panel can be clearly observed in the same figure, as well as the strong three-dimensionality of the flow over this model, that also affects the region close to the symmetry plane, where test requirements have been defined and matched in the test design activity (Rufolo et al., 2008).

An enlargement of the model top frame is reported in Fig. 12, where the skin friction lines are coloured depending on the local shear stress value. The local maxima of shear stress are predicted at the shoulder of the top frame and at the roundings of the lateral fairings, as expected, due to the turning of the flow with associated boundary layer thinning.

A large separated area (with negative values of shear stress) is clearly visible on the top frame caused by the local shock wave boundary layer interaction, with a nearly straight separation line and a highly distorted attachment line; the extent of the separated flow area increases at the extremities due to the inlet of the flow turning around the model.

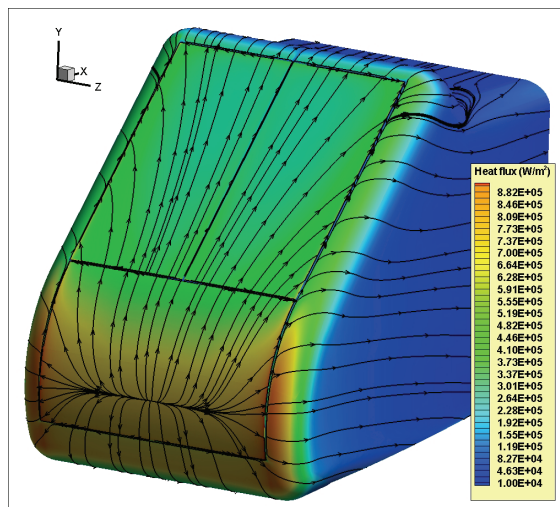


Fig. 11. Heat flux contour map with skin-friction lines

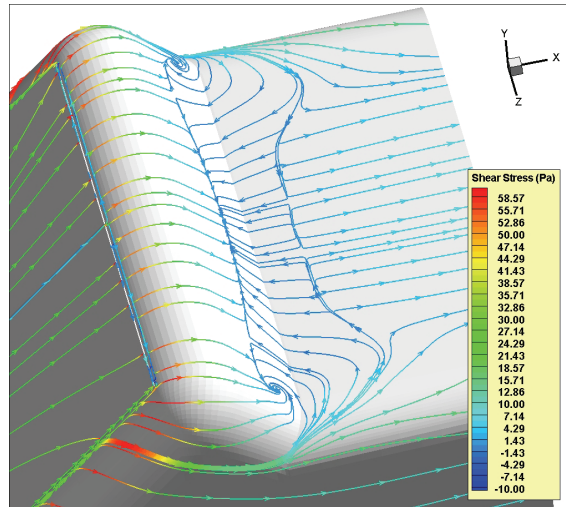


Fig. 12. Enlargement of the model top frame; skin-friction lines coloured by the shear stress

The lower frame heat flux contour map and the related skin friction lines are reported in Fig. 13, showing a nearly two-dimensional recirculation induced by the presence of the step, with maximum heat flux values ranging from 45 kW/m² in the central lower frame area to 90 kW/m² at the edges, where flow recirculation disappears due to the particular transversal shape of the model bottom part.

The flow inside the longitudinal gap existing between the two flat panels, and inside the transversal gap between the full span curved panel and the two flat panels (T-gap structure), is described in detail from Fig. 14 to Fig. 16. A flow recirculation is predicted inside the longitudinal gap (see Fig. 14), with a complex vortex pattern in the “T-gap” region (see Fig. 15). The vortex flow inside the transversal gap is characterized by a strong spanwise velocity component, that increases moving towards the edge, a inner vortex at the base of the panel and an attachment line at the front edge of the panel, where very high heat flux values (~1 MW/m²) are predicted in a very small region.

Fig. 16 describes the exit of the transversal gap flow into the external flow developing on the lateral fairing. The interaction of the two streams causes a rapid turning of the transversal gap flow with the formation of a local saddle point. It should be also underlined the presence of a inner vortex developing parallel to the junction between the flat panel and the lateral fairing, and the presence of an attachment line (the same already seen in Fig. 15) at the front edge of the flat panel, which corresponds to a region of high heat flux, with a maximum in the top corner of about 1.6 MW/m² but localized in a very small region (0.0002 m depth).

In order to verify test requirements in terms of heat flux and pressure at the beginning of the flat panel, and to properly evaluate spanwise and viscous effects, the longitudinal and transversal distributions along the slices indicated in Fig. 17 have been analyzed.

Results in terms of heat flux are reported in Fig. 18 and Fig. 19, showing transversal and longitudinal distributions, respectively, these latter ones compared to the two-dimensional results of test design activity (Rufolo et al., 2008).

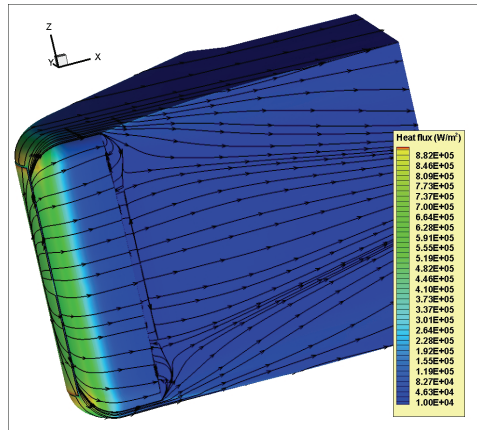


Fig. 13. Heat flux contour map with skin-friction lines; model bottom frame

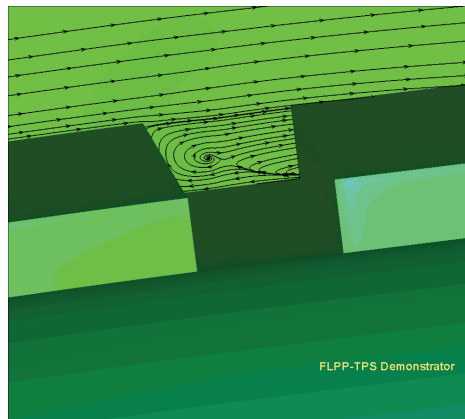


Fig. 14. Re-circulating region; longitudinal gap

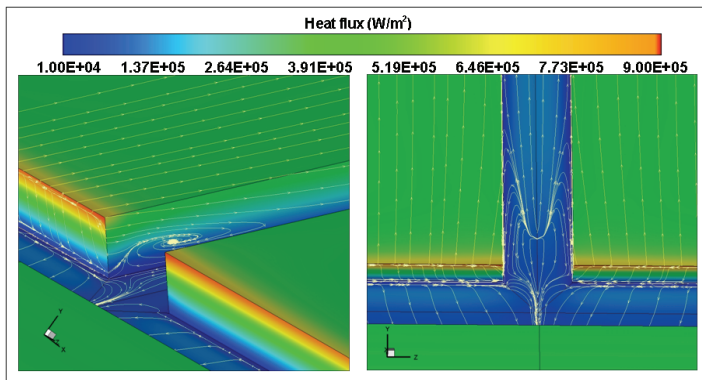


Fig. 15. T-gap; heat flux contour map with skin-friction lines

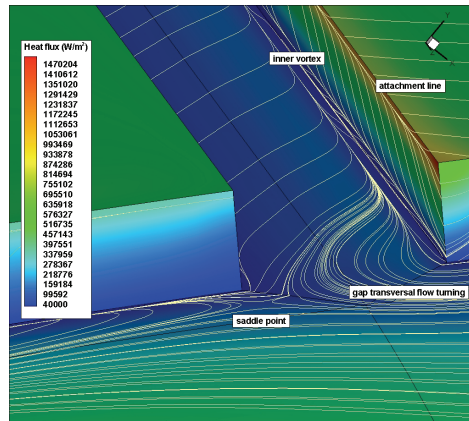


Fig. 16. Exit of transversal gap flow. Heat flux contour map and skin-friction lines

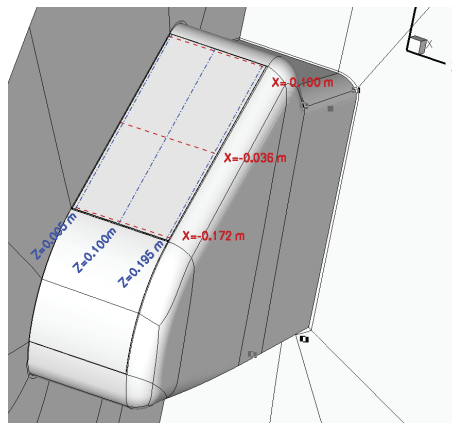


Fig. 17. Longitudinal and transversal slices

The increase of heat flux predicted on the flat panel is due either to spanwise effects either to the presence of gaps (longitudinal and transversal) and steps (lateral side), as clearly shown in Fig. 18. At the flat panel leading edge three-dimensional CFD simulation yields a 28% increase (450 kW/m^2) of predicted heat flux, both 5mm from the centreplane ($Z=0.005\text{m}$) and 5mm from the lateral edge ($Z=0.195\text{m}$), and it is nearly 350 kW/m^2 in-between. Downstream along the panel the predicted heat flux is closer to the test requirement, while localized high heat flux peaks are present in correspondence of gaps and steps.

Transversal and longitudinal wall pressure distributions are shown in Fig. 20 and Fig. 21, respectively. Pressure is not affected by spanwise effects from the qualitative point of view (the transversal distributions remain two-dimensional for most of the half panel span), but a quantitative reduction of 17% of maximum pressure on the flat panel centreplane is predicted (2070 Pa instead of 2500 Pa).

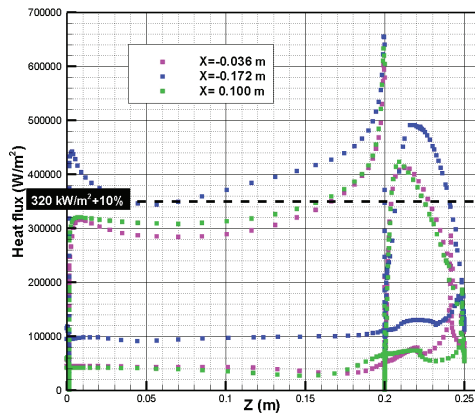


Fig. 18. Transversal heat flux distributions

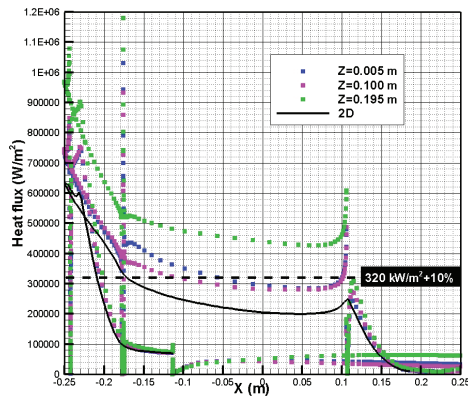


Fig. 19. Longitudinal heat flux distributions; comparison with 2D distribution

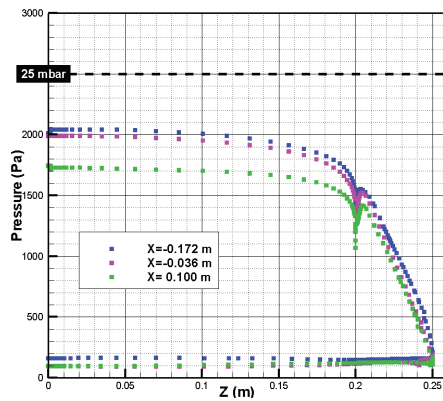


Fig. 20. Transversal wall pressure distributions

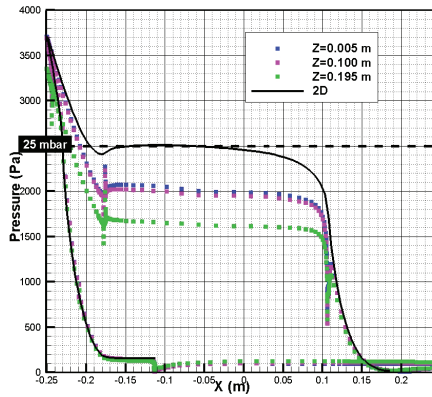


Fig. 21. Longitudinal wall pressure distributions; comparison with 2D distribution

5.2 Grid convergence of results

Grid convergence study is the most common and reliable technique for the quantification of numerical uncertainty (Roache, 1998) related to spatial discretization. It has been carried out for the three-dimensional pre-test computation by using the different grid levels indicated in Tab. 1.

Temporal convergence of the solutions has been obtained on all the grid levels.

Grid convergence of results has been evaluated in correspondence of the same points used in the design phase for monitoring the test requirements matching, i.e. the beginning of flat panel for the heat flux and the point of maximum value for the pressure on the flat panel, both taken at the centreline. In the three-dimensional case, these control points have been selected in the spanwise direction in order to be close to the symmetry plane, but sufficiently far from the region affected by the presence of the longitudinal gap; their coordinates are reported in Tab. 2.

Q^* and P^* indicate the values of heat flux and pressure in the selected points.

z=0.07 m	
x (for Q evaluation)	x (for P evaluation)
-0.172 m	-0.156 m

Table 2. Coordinates of the points selected for the grid convergence study

GRID	N	$N^{-1/3}$	$Q^*(W/m^2)$	$P^*(Pa)$
<i>coarse</i>	32468	0.0313	132675.69	1959.30
<i>medium</i>	259744	0.0157	335118.84	2024.86
<i>fine</i>	2077952	0.0078	349148.53	2044.60
Rich.Extrap.	inf.	0	353825.09	2051.19

Table 3. Q^* and P^* values at the selected points for the three grid levels and Richardson Extrapolation

The computed Q^* and P^* values are reported in Tab. 3 for the three grid levels, together with the Richardson Extrapolation value. This latter is an estimation of the “continuum value” (i.e., the value at zero grid spacing), obtained from a series of discrete values, and it is defined in the following way:

$$f_{h=0} \cong f_1 + \frac{f_1 - f_2}{r^p - 1} \quad (1)$$

where: $f_{h=0}$ is the value at zero grid spacing; f_1 and f_2 are the values computed on two grids, f_1 being the finer one; p is the order of the solution ($p=2$ for this case); r is the grid refinement ratio:

$$r = \sqrt[3]{\frac{N_1}{N_2}} \quad (2)$$

N_1 and N_2 being the numbers of cells of the grids 1 and 2, respectively. In the following, N will be used to indicate the total number of cells of a grid level, while $(1/N)^{-1/3}$ is a parameter that represents adequately the grid resolution.

The difference between the values f_1 and $f_{h=0}$ is one of the error estimators. The actual fractional error is defined as:

$$A_1 = \frac{f_1 - f_{h=0}}{f_{h=0}} \quad (3)$$

Another error estimator, the relative error, is based on the difference between f_1 and f_2 :

$$\varepsilon = \frac{f_2 - f_1}{f_1} \quad (4)$$

This quantity has to be corrected to take into account r and p . The estimated fractional error for f_1 is therefore defined as:

$$E_1 = \frac{\varepsilon}{r^p - 1} \quad (5)$$

Although E_1 is based on a rational theory, it is not a bound on the error. On the contrary the Grid Convergence Index (GCI) provides an error band, i.e. a tolerance on the accuracy of the solution (Roache, 1998). The GCI on the fine grid is then defined as:

$$GCI_{fine} = \frac{F_S |\varepsilon|}{(r^p - 1)} \quad (6)$$

where F_S is a safety factor, that is recommended to be 3.0 when comparing the results of two grids, and 1.25 for comparison of three grids (being this latter our case). The above defined error estimators have been all calculated, and are reported in Tab. 4 for Q^* and P^* .

The values of heat flux (Q^*) and pressure (P^*) are reported in Fig. 22 for the three grid levels in function of the grid resolution (i.e. the parameter $(1/N)^{-1/3}$) and compared with the value corresponding to zero grid spacing (computed by means of the Richardson extrapolation).

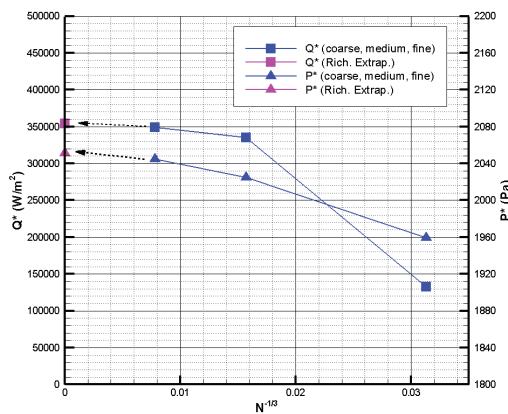
Error Indices	$Q^*(W/m^2)$	$P^*(Pa)$
<i>eps</i>	0.0402	0.0097
<i>E1</i>	0.0134	0.0032
GCI	0.0167	0.0040
<i>A1</i>	-0.0132	-0.0032

Table 4. Grid error indices

These plots confirm the right trend of solution grid convergence both for heat flux and pressure. In fact, the difference existing between the results of the coarse grid level and the medium one decreases if comparing the medium level with the fine one, and the trend of solution is towards the Richardson extrapolated value.

As a consequence, the Grid Convergence Index provides a level of confidence of the solution, therefore it can be concluded that (see Tab. 4):

- the error committed on the heat flux value with the finer grid level should be lower than 1.67 %;
- the error committed on the pressure value with the finer grid level should be lower than 0.40 %.

Fig. 22. Grid convergence estimation for heat flux (Q^*) and pressure (P^*) at the selected points

5.3 Estimation of uncertainties

An assessment of the uncertainty level related to test requirements fulfilment in terms of heat flux and pressure to be realized over the test-article is provided in this subsection, both for test design and test execution phases (Rufolo et al., 2008). The high complexity of involved phenomena together with the heterogeneous character of the different error sources make it impossible to give a rigorous definition and quantification of the error, but only a simplified estimation can be pursued.

Fig. 23 reports the entire process of numerical test design and test execution: during the design phase, starting from test requirements, a CFD aided activity is carried out in order to derive the proper settings for the heat flux (Q_s) and pressure (P_s) over the PWT calibration probe; in the testing phase the facility driving parameters (mass flow and arc current) are tuned in order to get the desired couple (Q_s , P_s) over the calibration probe, then the test is executed and with

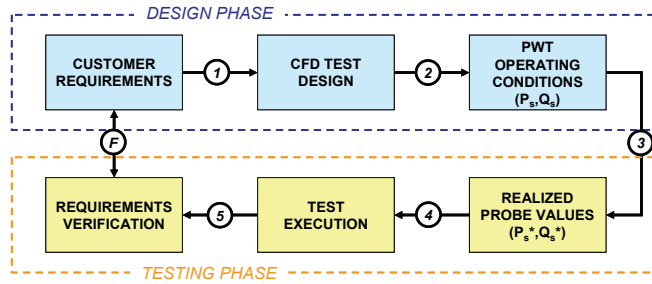


Fig. 23. Numerical test design and test execution chain

the post-test analysis it is finally possible to verify the matching of the requirements. Obviously, an error ε_i is linked to each phase of the above described chain, and all of them contribute in determining the difference between the original requirements and their actual realization. It has to be said that in the present case the requirements were expressed in terms of heat flux and pressure for a fully catalytic and isothermal cold wall, and this is clearly a not realistic hypothesis for the kind of material and type of test to be conducted.

Moreover, during the test no heat flux direct measurements have been provided, and only an indirect derivation from temperature measurements can be obtained assuming radiative equilibrium at the wall (i.e. neglecting conduction into the material). In order to fully exploit measurements it is needed to associate correct values of catalytic recombination and emissivity coefficients, but these data have not been available during the project.

For these reasons, being unfeasible to characterize the complete error chain, only the following components of the error chain will be described hereinafter (Rufolo et al., 2008):

- how the test requirement is translated by means of CFD into PWT conditions (ε_2 in Fig. 23);
- how the error in the experimental realization of the set point propagates on the requirements over the test-article (ε_3 in Fig. 23).

The evaluation of the error ε_3 propagation is made by substituting the facility with its numerical modelling.

The numerical setting of PWT operating conditions comes out from an iterative process in which the facility driving conditions (H_0, P_0) are tuned in order to match the requirements in terms of heat flux and pressure over the model to be tested (Di Benedetto et al., 2007). The error related to this process is definitively negligible, in the sense that it is always possible to find a couple (H_0, P_0) that allows to numerically satisfy the requirements whichever is the accuracy prescribed. At the end of this process, when the correct couple (H_0, P_0) has been found, the simulation of the flow field around the calibration probe is carried out in order to find out the couple (Q_s, P_s) that will be used for the test execution (Di Benedetto et al., 2007). The process that translates the reservoir condition (H_0, P_0) in local parameters (Q_s, P_s) by means of a numerical modelling is affected by an error, above defined as ε_2 .

By following the classical taxonomy adopted for CFD (AIAA, 1998) it is possible to recognize the following three error components for ε_2 :

- the Modelling Error (Chemical processes, fluid properties, Initial and Boundary conditions, Geometry representation, Turbulence Model);
- the Discretization Error (Grid independence, algorithm error);
- the Iteration Error (Convergence criterion).

The modelling error is by far the most complex source of uncertainty to estimate. The common practice (AIAA, 1998) relies on the validation of the numerical code with respect to experimental measurements obtained for simple test cases. Unfortunately, the experimental measurement it is affected by an error that, especially in the case of heat flux measurements for aerothermodynamic tests, can make void the validation process.

As reported in (Ranuzzi & Borreca, 2006) a series of comparisons with existing literature experiments were carried out during the development and validation phase of the H3NS CFD code. In particular, it was decided to refer to the Hyperboloid Flare Test Case carried out at the F4 blow-down arc heated high enthalpy facility of the ONERA in order to find out an error level applicable to the present case (Rufolo et al., 2008). The freestream Mach number is 8.7, the total enthalpy is about 13 MJ/Kg, the wall is considered isothermal at a temperature of 300 K and fully catalytic. Trying to find out an estimation of the modelling error related to the phenomenon we are interested in (heat flux and pressure along the test-article flat panel), it is possible to extract the average percentage error for the measurement stations located in the mid part of the hyperboloid and ahead of the flare. In this way an error of about 4% for heat flux and 3% for pressure is obtained.

Another possibility for estimating the modelling error, in absence of affordable experimental results, is to carry out a sensitivity analysis with respect, for instance, to chemical model and/or transport properties model. With respect to the transport properties model, results obtained for the hyperboloid flare show no significant effect on pressure, while for heat flux the maximum deviation is about 3.1%. As for the chemical models, a dedicated analysis has been carried out both for the PWT calibration probe and for the SPS test-article. The four different chemical models implemented in H3NS (Ranuzzi & Borreca, 2006) have been tested: Kang-Dunn (Dunn & Kang, 1997), Park 1990 (Park, 1990), Park-Rakich (Rakich et al., 1983) and Park 1993 (Park & Lee, 1993), this latter being the chemical model used for all the simulations performed in the present activity. Regarding the stagnation point of the calibration probe, the largest deviation occurs for the Kang-Dunn model (2.63% for heat flux and 0.97% for pressure). For what concerns the SPS test-article simulation, the percentage deviations of heat flux at the beginning of the flat panel and of maximum pressure over the flat panel obtained with Kang-Dunn model with respect to the Park 1993 results are respectively 0.38% and 3.13%.

For what concerns the discretization error, the results of the grid convergence analysis of the three-dimensional simulation of the FLPP-SPS test-article, reported in Section 5.2, show that, with respect to an ideal zero-spacing grid, an error of 1.67% on the heat flux at the beginning of the flat panel and of 0.40% on the maximum pressure on the panel is committed.

For what concerns the iteration error, it has to be said that, even if we are interested in achieving the steady state solution of the Navier-Stokes equations, when the flow field to be resolved contains features characterized by intrinsic unsteadiness (e.g. recirculation bubble, vortex shedding, shock wave instability), the residue of the equations does not decrease towards the machine precision. Despite the presence of these unsteadiness, the quantities of interest in our case, as the heat flux and the pressure over the flat panel, reached a steady state value so that the iteration error can be neglected.

Trying to summarize, Tab. 5 reports the identified uncertainties (intended as estimation of the errors). The last column of the table reports the "overall error" obtained adding all the components.

Concerning the error ε_3 , it is needed to estimate how the experimental uncertainty on the measurements of heat flux and pressure over the calibration probe translates in uncertainty

Modeling error						
	Discretization	Iteration	Validation	Chem Model Sensitivity	Transport Model Sensitivity	Overall Error
$\varepsilon_2(Q)$	1.7%	~0	4.0%	2.6%	3.1%	11.5%
$\varepsilon_2(P)$	0.4%	~0	3.0%	3.1%	~0	6.5%

Table 5. Summary of identified error components

of the requirements over the test article. This can be done only by adopting the CFD tool as transfer function. The error associated to the heat flux measurement of the calibration probe is ± 90 kW/m², while the one associated to the stagnation pressure measurement is ± 1.1 mbar (Marini et al., 2002). Starting from the values realized during the test, four couples (Q_s , P_s) have been identified by adding and subtracting their own error both to Q_s and P_s ; the corresponding values are reported in the first two columns of Tab. 6. For each couple, the facility driving conditions (H_0 , P_0) have been found by following the iterative process already described (Di Benedetto et al., 2007) (columns three and four of Tab. 6), and then two-dimensional simulations of both probe and model (i.e. test article) have been carried out for each condition. The percentage errors referred to the nominal values are reported in Tab. 6 for each of the four conditions.

	PROBE EXP				PROBE CFD				MODEL CFD			
	Ps [mbar]	Qs [kW/m2]	P0 [bar]	H0 [MJ/kg]	Ps [mbar]	err%	Qs [kW/m2]	err%	POINT #4 Ps [mbar]	err%	POINT #1 Qs [kW/m2]	err%
(p_{req}, q_{req})	34.2594	2121.82	4.90	17.40	34.26		2121.82		23.84		338.66	
$[p_{req}, q_{req} + err(q)]$	34.2594	2211.82	4.88	18.03	34.25	0.02%	2211.56	4.23%	23.82	0.08%	353.02	4.24%
$[p_{req}, q_{req} - err(q)]$	34.2594	2031.82	4.93	16.81	34.26	0.01%	2030.47	4.31%	23.84	0.02%	325.32	3.94%
$[p_{req} + err(p), q_{req}]$	35.3594	2121.82	5.07	17.18	35.35	3.17%	2122.05	0.01%	24.58	3.12%	339.47	0.24%
$[p_{req} - err(p), q_{req}]$	33.1594	2121.82	4.73	17.64	33.18	3.14%	2125.11	0.16%	23.09	3.14%	338.39	-0.08%

Table 6. Influence of calibration probe measurements uncertainty on test article requirements

Regarding the model, the errors were evaluated with respect to the beginning of the flat panel for the heat flux (Point #1 in Tab. 6) and to the maximum value over the flat panel for the pressure (Point #4 in Tab. 6). It can be seen that in the worst case the difference between the errors on the probe and on the model are limited to 0.37% for the heat flux and 0.05% for the pressure. So it can be stated that, within the approximation related with the numerical process, the experimental uncertainties on the point settings is identically transferred to test article requirements.

In conclusion, the analysis reported above has been aimed at deriving an estimation of the errors ε_2 and ε_3 . Obviously, the analysis cannot be considered exhaustive and especially for the CFD related error only a very simplified indication has been provided. As a matter of fact, the two errors ε_2 , ε_3 can be considered fully independent.

At worst, for the present case the estimated overall errors are about 15% on heat flux and 9.5% on pressure.

6. Rebuilding CFD activity

The FLPP-SPS TPS demonstrator plasma wind tunnel test was successfully performed on September 20th, 2007 simulating a 15 min re-entry trajectory in three steps characterized by

increasing total enthalpy level in test chamber, i.e. increasing continuously wall heat flux (Trifoni et al., 2007).

The test condition, which the CFD three-dimensional analysis described in the previous section refers to, corresponds to the second test step, defined as the “nominal” one. This latter condition has been rebuilt after the test by exploiting the calibration probe heat flux and pressure available measurements.

A different hypothesis about the temperature wall condition has been made, in order to simulate a more realistic condition with respect to the hypothesis of cold wall of the pre-test CFD simulation. In particular, radiative wall temperature has been computed assuming the equilibrium between the convective and the radiative heat fluxes. The emissivity coefficient has been provided by SPS ($\epsilon=0.8$), while the hypothesis of fully catalytic surface has been maintained also in the test rebuilding CFD simulation, as also indicated by SPS.

In Fig. 24 the CAD model (left) is compared with the model as built (right), in which there is no step in the bottom part. However, this difference in the test article configuration should involve discrepancies only on the regions closer to the bottom part of the model, therefore no influence is expected on the flat and curved panels.

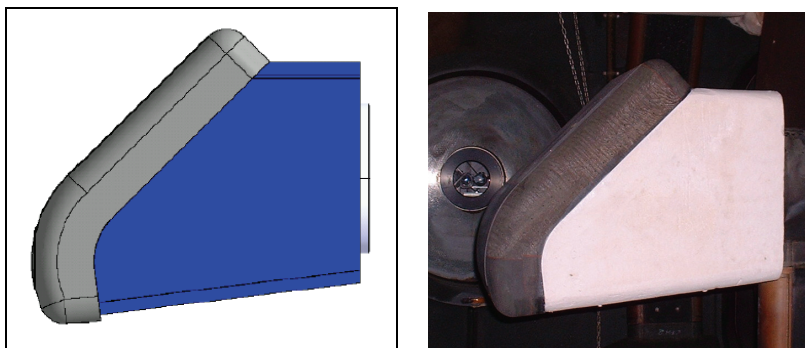


Fig. 24. CAD model (left) and model as built (right)

6.1 Operating condition assessment

The pre-test three-dimensional CFD simulation has been carried out in the PWT operating condition resulting from the previous CFD test design activity (Rufolo et al., 2008), whose results are reported in Tab. 7.

Design Test Chamber Conditions	P_0 (bar _a)	H_0 (MJ/kg)
	5.20	16.70
Calibration Probe Stagnation Point (CFD)	P_s (mbar _a)	Q_s (kW/m ²)
	36.15	2070

Table 7. PWT test design operating condition

This condition has been compared, in terms of heat flux and pressure on the PWT hemispherical calibration probe, with that actually measured during the second step (the “nominal” one) of the test. These latter values are reported in Tab. 8, together with their error bars (Trifoni et al., 2007).

In order to reproduce in the rebuilding CFD simulation the same condition realized in test chamber during the test in terms of total pressure and total enthalpy, the iterative procedure described in (Rufolo et al., 2008) and (Di Benedetto et al., 2007) has been applied, this time having as requirements the values measured on the calibration probe.

Calibration Probe Stagnation Point (Measured)	P_s (mbar _a)	Q_s (kW/m ²)
	34.20±1.1	2120±90

Table 8. Values at the calibration probe stagnation point measured during the test

Finally, the PWT operating condition obtained for the rebuilding CFD activity is summarized in Tab. 9.

Rebuilding Test Chamber Conditions	P_0 (bar _a)	H_0 (MJ/kg)
	4.90	17.40
Calibration Probe Stagnation Point (CFD)	P_s (mbar _a)	Q_s (kW/m ²)
	34.25	2121

Table 9. PWT test rebuilding operating condition

6.2 Three-dimensional results

The three-dimensional CFD rebuilding simulation has been performed in the PWT “nominal” test condition of Tab. 9. The more realistic radiative equilibrium wall condition, with surface emissivity $\epsilon=0.8$, has been imposed instead of the cold wall. In order to qualitatively evaluate the actual catalysis of the CMC panels through comparison with temperature measurements, both fully catalytic (FC) and non catalytic (NC) wall conditions have been considered.

Heat flux distribution together with the skin-friction lines pattern on the test article is shown in Fig. 25: heat flux on the stagnation line is about 600 kW/m² for FC case, and it decreases to 200 kW/m² for NC one. Temperature contour maps are shown in Fig. 26: in the FC case the local maximum values of temperature are around 2000 K on the stagnation line and about 2200 K on the roundings of lateral fairings of the curved panel. On the flat panels the predicted temperature ranges from about 1500 K (in the single panel central area) to about 1800 K at the panel lateral edges. Temperature levels of about 1000 K are predicted on the lateral sides of the test article. These values are quite strongly reduced with the NC assumption (about 500 K on the stagnation line), due to a combined effect of the high energy content of the flow and the large bluntness of the test article.

The analysis which follows refers to FC condition results only, this in order to make possible a comparison with the pre-test numerical findings. An enlargement of the model top frame with skin-friction lines coloured by shear stress value is reported in Fig. 27 (left) and compared with the distribution obtained in the pre-test simulation (right). The phenomenology and the shear stress distribution are very similar to those predicted in the pre-test activity, while a slightly larger separated area is observed as a consequence of the changed wall temperature condition. In fact, a higher surface temperature implies a boundary layer thickening (in particular of the subsonic region), in this way increasing the upstream and downstream pressure disturbance propagation. As a consequence of the

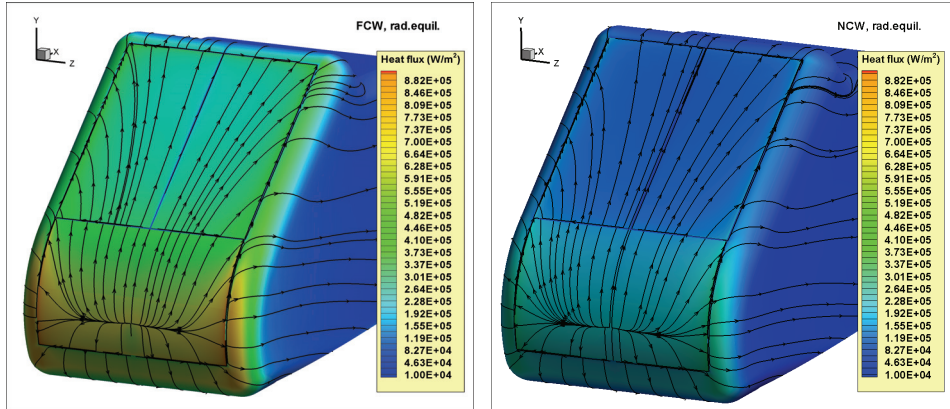


Fig. 25. Heat Flux contour map with skin-friction lines; FC (left), NC (right)

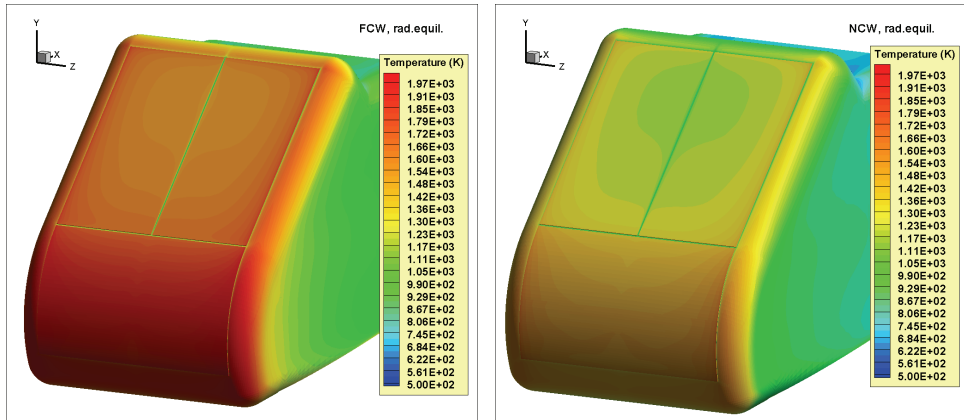


Fig. 26. Temperature contour map; FC (left), NC (right)

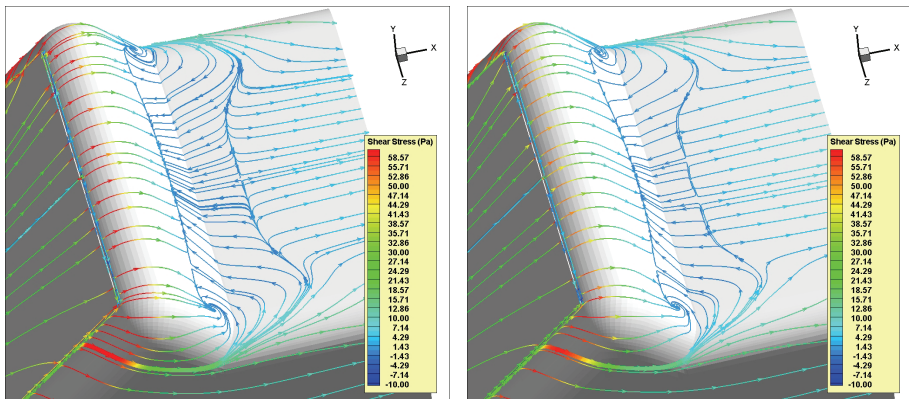


Fig. 27. Enlargement of the model top frame; skin-friction coloured by the shear stress; rebuilding (radiative equilibrium, left), pre-test (cold wall, right)

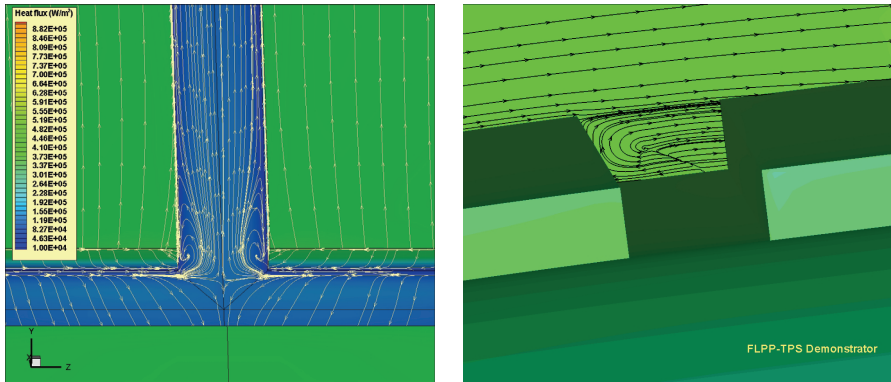


Fig. 28. T-gap heat flux contour map with skin-friction lines (left) and longitudinal gap recirculation (right)

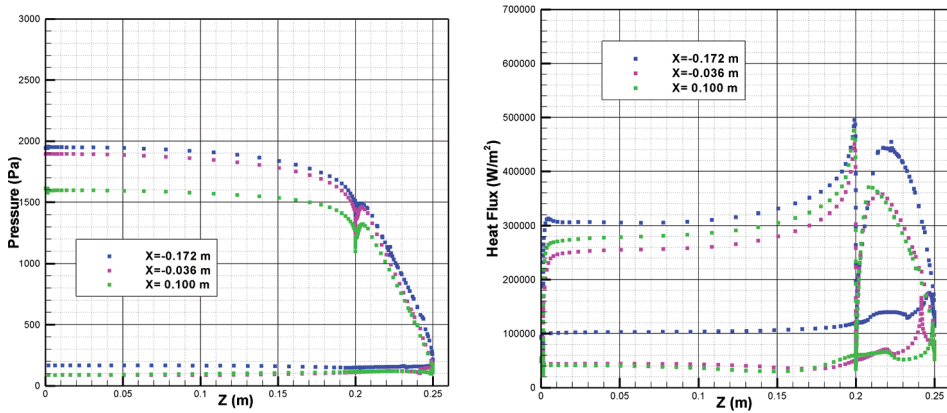


Fig. 29. Transversal pressure (left) and heat flux (right) distributions

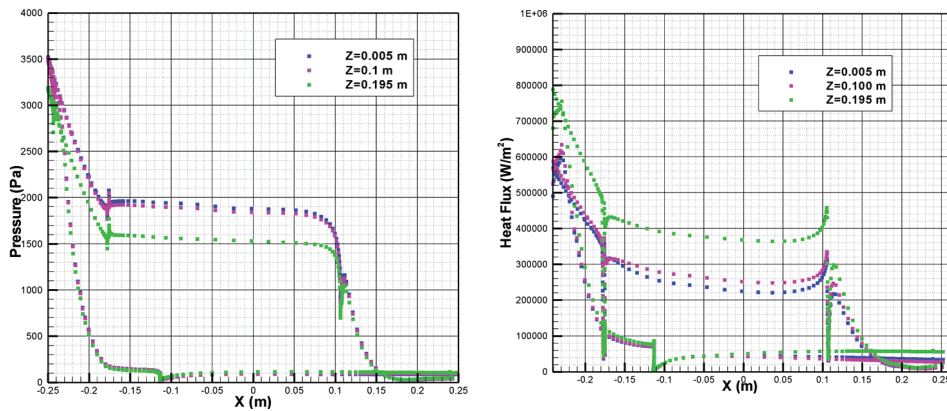


Fig. 30. Longitudinal pressure (left) and heat flux (right) distributions

increased temperature, an extension of the regions submitted to higher shear stress is observed, although the overall structure of the flow seems unchanged.

The flow inside the T-gap is described in Fig. 28. The interaction between the transversal stream and the longitudinal one realizes in a saddle point and in two lateral vortices, but with a different flow pattern with respect to the pre-test simulation due to the effects of the surface temperature wall condition (see Fig. 14 and Fig. 15). The vortex flow inside the transversal gap is again characterized by a strong spanwise velocity component that increases moving towards the edge, a inner vortex at the base of the panel and an attachment line at the front edge of the panel. As expected, the region of high heat flux at the front edge of the flat panel, and in particular at the top corner, is largely reduced.

Pressure and heat flux distributions in transversal and longitudinal directions are shown, respectively, in Fig. 29 and Fig. 30. The main flow features, already described in Section 5.1 (see from Fig. 18 to Fig. 21), are all confirmed by the present test CFD rebuilding, although quantitative levels are different due either to the realization of a slightly different “nominal” condition, with respect to that analyzed during the pre-test CFD activity, either to the different surface thermal boundary condition.

At the flat panel leading edge, CFD rebuilding simulation yields a heat flux of about 440 kW/m² 5mm from the lateral edge ($Z=0.195\text{m}$), and it is slightly larger than 300 kW/m² for the rest of the panel (Fig. 29-right). Downstream along the panel heat flux remains around 300 kW/m² apart from the lateral edge, affected by the presence of the step, where 400 kW/m² all along the panel are predicted (Fig. 30-right).

Transversal and longitudinal pressure distributions over the model are reported in Fig. 29-left and Fig. 30-left respectively; pressure is not significantly affected by spanwise effects, apart from the more lateral section $Z=0.195\text{ m}$ where a strong flow expansion occurs: transversal distributions remain two-dimensional for most of the half panel span, as well as the longitudinal ones are flat enough for 80% of the panel length.

7. CFD/Experiments comparison

In this section some of the experimental data collected during the FLPP-SPS demonstrator test in the SCIROCCO PWT (Trifoni et al., 2007) are compared to the results of the numerical rebuilding described in Section 6.

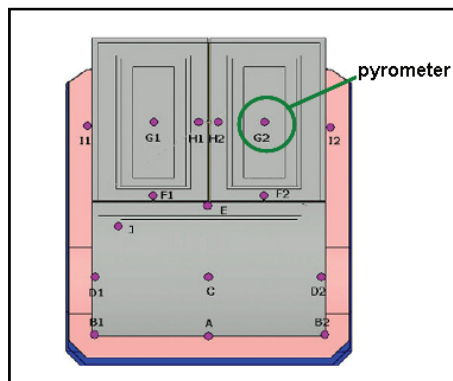


Fig. 31. Test article instrumentation

During the test, eleven B-type thermocouples have measured the back wall temperatures of the CMC panels. Among these, those located on the flat panels which have correctly worked (F2-1, G2-1, H2-1, H1-1, see Fig. 31) have been selected to perform comparisons with CFD temperature distributions. Moreover, a dual colour pyrometer (range: 1000-3000 °C) has been pointed to G2-1 thermocouple location and two IR thermo-cameras ($\epsilon=0.8$, range: 600-2500°C) have been used to monitor the test article during the test both from the top (flat panels) and from the lateral front (curved panel area).

In Fig. 32 temperature measured by thermocouples is compared with CFD distributions along the two sections, indicated as slices in the figure, where thermocouples are located.

As expected, measured temperatures lie more or less in the middle between the non catalytic (NC) and the fully catalytic (FC) distributions. In addition, it has to be said that the surface temperatures can be estimated to be about 50 °C higher than the measured back wall ones.

In Fig. 33, the same kind of comparison is reported for the temperature measured by the dual colour pyrometer. A lower emissivity value of 0.68, which is a combination of the real emissivity value of the material and all the experimental uncertainty factors, allows to match pyrometer and thermal camera readings, as reported in Tab. 10 (experimental emissivity evaluation). Therefore, also the CFD temperatures in Fig. 33 have been properly scaled (to the emissivity value of $\epsilon_{exp}=0.68$) in the post-processing phase, in such a way to make the comparison meaningful and to reproduce as much as possible the actual wall conditions.

An attempt to derive an estimation of the CMC panels catalytic recombination coefficient has been done by combining the experimental results to a CFD-based correlation. Namely, by means of CFD two-dimensional computations with finite rate catalysis values at the wall, a function that relates the heat flux at a certain point of the flat panel with the recombination

T pyrometer	T thermocamera	ϵ_{exp}
1500 K	1360 k	0.68

Table 10. Experimental emissivity evaluation

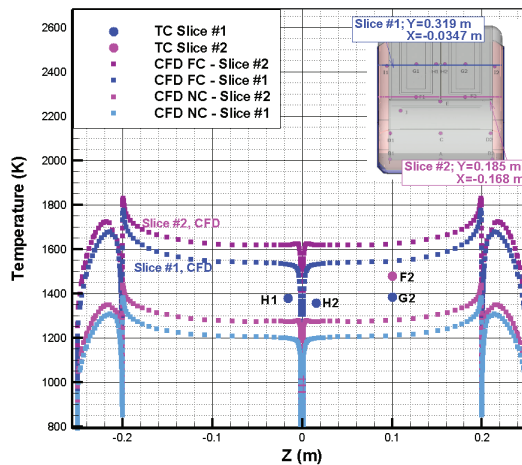


Fig. 32. Comparison between temperature CFD distributions and thermocouples measurements

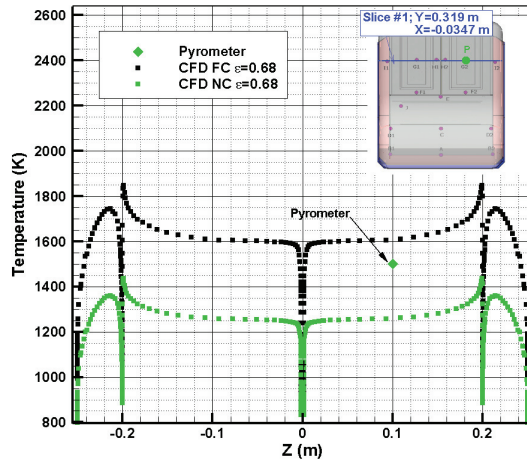


Fig. 33. Comparison between temperature CFD distributions and pyrometer measurement

coefficient γ has been derived. By crossing this function with the radiative heat flux corresponding to the pyrometer reading, a value for γ of about 0.008 has been obtained. It has to be remarked that this value only represents a rough estimation and it includes all the numerical and experimental errors.

Finally, some qualitative comparisons of the bow shock wave shape are shown from Fig. 34 to Fig. 36, where the predicted flow field in the shock layer region has been overlapped to the images taken by the two video cameras during the test. In Fig. 34 and Fig. 35, the shock section extracted from CFD computation and the predicted temperature field in the shock region have been superimposed on a view from the top camera. The comparison shows that both shock shape and stand off distance predicted in the stagnation region well reproduce the actual ones. In Fig. 36 the predicted atomic nitrogen mass fraction is overlapped to a view from the side camera, showing a good agreement of predicted and actual shock shape around the entire model, and a significant presence of atomic nitrogen (N) around most of the curved panel.

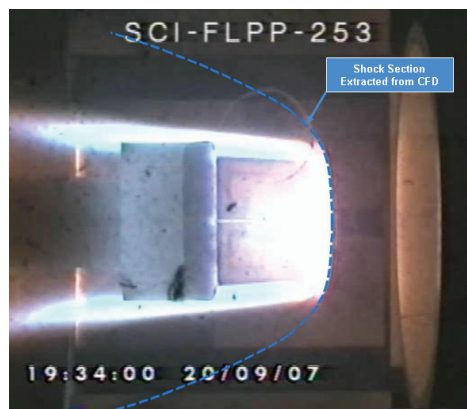


Fig. 34. Top view of the model during test. Comparison of predicted and actual shock shape



Fig. 35. Top view of the model during test. Comparison with predicted temperature contours

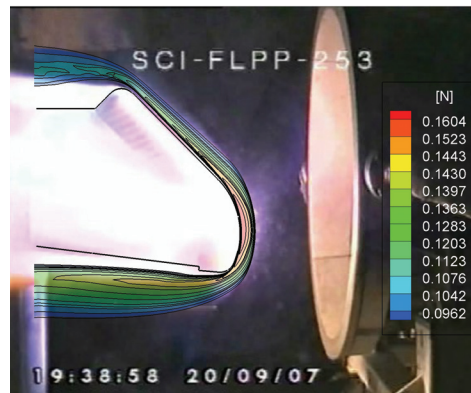


Fig. 36. Side view of the model during test. Comparison with predicted nitrogen concentration

8. Conclusions

This chapter has described the three-dimensional CFD activities carried out to support the SCIROCCO plasma wind tunnel test performed on the FLPP-SPS TPS demonstrator designed and manufactured by Snecma Propulsion Solide.

After a CFD pre-test activity, during which the test point previously designed by a simplified two-dimensional methodology has been verified and the final PWT test condition frozen, the post-test phase has regarded the plasma test CFD rebuilding.

The FLPP-SPS PWT test was performed with full success on September 20th, 2007 simulating a 15 minutes re-entry trajectory in three steps characterized by increasing total enthalpy levels in test chamber. The test condition which the present CFD three-dimensional analysis refers to corresponds to the second "nominal" step.

This latter condition has been rebuilt by exploiting the calibration probe heat flux and pressure available measurements, and by applying the same iterative procedure used

during the test design phase, this time having as requirements the values measured on the calibration probe. Moreover, in order to perform more realistic simulations, radiative equilibrium has been imposed at the wall, whereas to qualitatively evaluate the actual CMC panels catalysis both FC and NC conditions have been considered.

Similar flow features have been predicted both in the pre-test phase and the post-test rebuilding phase, and some meaningful comparison between CFD rebuilding results and experimental findings have allowed to assess the full capability of the present CFD-based methodology to design and properly rebuild a plasma wind tunnel test, with its own accuracy bounds. In addition, an approach to determine the uncertainties related to both design and testing phases, with respect to the satisfaction of test requirements, has been presented.

Finally, a rough estimation of the catalyticity of the CMC panels under realistic re-entry conditions has been obtained by crossing experimental measurements and CFD results.

An important step for future applications like the present should be to rebuild plasma wind tunnel tests accounting for the actual catalytic behaviour of the different parts of the test article. Of course, to do this the proper experimental characterization of the involved materials in terms of recombination coefficients as functions of temperature and pressure is needed. Then, once having re-tuned the CFD methodology, the approach could be directly applied starting from the pre-test design phase.

9. Acknowledgements

This work has been fully supported by SPS in the frame of FLPP Materials & Structures Technological Activities, Period 1, Phase 1, coordinated by NGL Consortium and supervised by the European Space Agency.

A special thank goes to the whole CIRA Plasma Wind Tunnel Team that made possible the FLPP-SPS test campaign.

10. References

- Barreteau, R., Foucault, A., Parenteau, J.M., Pichon, T. (2008). Development and Test of a Large-Scale CMC TPS Demonstrator, *2nd International ARA DAYS*, AA-3-2008-4, 21-23 October, 2008, Arcachon, France.
- Rufolo, G., Di Benedetto, S., Marini M. (2008) Theoretical-Numerical Design of a Plasma Wind Tunnel Test for a Large TPS Demonstrator, *6th European Symposium on Aerothermodynamics for Space Vehicles*, paper s17_5, Versailles, France, November 2008.
- Marini, M., De Filippis, F., Del Vecchio, A., Borrelli, S., Caristia S. (2002) CIRA 70-MW Plasma Wind Tunnel: A Comparison of Measured and Computed Exit Nozzle Flow Profiles, *Euromech-440 Conference*, 16-19 September 2002, France, Marseilles.
- De Filippis, F. et al. (2003) The Scirocco PWT Facility Calibration Activities, *3rd International Symposium Atmospheric Reentry Vehicle and Systems*, March 2003, Arcachon, France.
- Ranuzzi, G., & Borreca, S. (2006) CLAE Project. H3NS: Code Development and Validation, *Internal Report CIRA-CF-06-1017*, September 2006.
- Di Clemente, M. (2008) Numerical studies for the realization of aerodynamic systems for guide and control of re-entry vehicles, *Ph.D. Dissertation*, Mechanics and Aeronautics Dept., La Sapienza Univ., Rome.

- Park, C. (1989) A Review of Reaction Rates in High Temperature Air, *AIAA Paper 89-1740*, June 1989.
- Millikan, R.C., White, D.R. (1963) Systematic of Vibrational Relaxation, *Journal of Chemical Physics*, Vol. 39, No. 12, pp. 3209-3213.
- Park, C., Lee, S. H. (1993) Validation of Multi-Temperature Nozzle Flow Code NOZNT, *AIAA Paper 93-2862*.
- Yun, K. S., Mason, E. A. (1962) Collision Integrals for the Transport Properties of Dissociating Air at High Temperatures, *Physics of Fluids*, Vol. 5, No. 4, 1962, pp. 380-386.
- Kee, R. J., Warnatz, J., Miller, J. A. (1983) A Fortran Computer Code Package for the Evaluation of Gas-Phase Viscosities, Conductivities and Diffusion Coefficients, *Sandia Rept. SAND83-8209*, March 1983.
- Di Benedetto, S., Bruno, C. (2010) A Novel Semi-Empirical Model for Finite Rate Catalysis with Application to PM1000 Material, *Journal of Thermophysics and Heat Transfer*, Vol. 24, No. 1, January-March 2010, pp. 50-59.
- Roache, P.J. (1998) *Verification and Validation in Computational Science and Engineering*, Hermosa Publishers, Albuquerque.
- AIAA (1998) *Guide for the Verification and Validation of Computational Fluid Dynamics Simulations*, G-077-1998, January 14, 1998.
- Dunn, M.G., Kang, S.W. (1973) Theoretical and experimental studies of reentry plasma. *Technical Report NASA CR 2232*, NASA.
- Park, C. (1990) *Nonequilibrium Hypersonic Aerothermodynamics*, Wiley Interscience.
- Rakich, J.V., Bailey, H.E., Park, C. (1983) Computation of nonequilibrium, supersonic three-dimensional inviscid flow over blunt-nosed bodies, *AIAA Journal* Vol. 21, June 1983, pp. 834-841, ISSN 0001-1452.
- Trifoni, E. et al. (2007) DD[3] - PWT Test Report, *Internal Report CIRA-TR-07-0230*, November 2007.
- Di Benedetto, S., Di Clemente, M., Marini, M. (2007) Plasma Wind Tunnel Test Design Methodologies for Re-entry Vehicle Components, *2nd European Conference for Aerospace Sciences (EUCASS)*, paper N. 228, 1-6 July 2007, Brussels, Belgium.

Part 2

Applications of Wind Tunnels Testing

Flow Visualization and Proper Orthogonal Decomposition of Aeroelastic Phenomena

Thomas Andrianne, Norizham Abdul Razak and Grigorios Dimitriadis
*Aerospace and Mechanical Engineering Department, Faculty of Applied Sciences,
 University of Liège
 Belgium*

1. Introduction

The modal decomposition of unsteady flowfields was proposed in the 1990s by several authors, e.g. Hall (1994) or Dowell et al. (1998). Proper Orthogonal Decomposition (POD) is one method that can be used in order to perform this modal decomposition; it became popular for aerodynamics research in the 2000s, starting with Tang et al. (2001), although it was first proposed for use in fluid dynamics in the 1960s by Lumley (1967).

The basic principle of POD is the creation of a mathematical model of an unsteady flow that decouples the spatial from the temporal variations. A 2D flowfield described by the horizontal velocity $u(x, y, t)$ and the vertical flow velocity $v(x, y, t)$ can thus be expressed as

$$\begin{aligned} u(x, y, t) &= \bar{u}(x, y) + u'(x, y, t) = \bar{u}(x, y) + \sum_{i=1}^M q_i(t) \phi_{u,i}(x, y) \\ v(x, y, t) &= \bar{v}(x, y) + v'(x, y, t) = \bar{v}(x, y) + \sum_{i=1}^M q_i(t) \phi_{v,i}(x, y) \end{aligned} \quad (1)$$

where $\bar{u}(x, y)$ and $\bar{v}(x, y)$ are obtained by time averaging the flowfield over M time instances, while $u'(x, y, t)$ and $v'(x, y, t)$ are time-dependent fluctuations from the mean. These fluctuations are decomposed using M mode shapes $\phi_{u,i}(x, y)$, $\phi_{v,i}(x, y)$ and M generalized coordinates $q_i(t)$. For a reduced order model, the number of modes, $N \ll M$, is to be chosen as a compromise between model simplicity and model accuracy. The principle of the POD technique is to extract the most energetic modes that capture most of the unsteady flow energy. The POD technique has been used to decompose several types of aerodynamic flows, such as the flow behind a disk (Tutkun et al., 2008), the flow past a delta wing (Cipolla et al., 1998), the unsteady flow impinging on an aircraft tail behind a delta wing (Kim et al., 2005), the unsteady flow around a F-16 fighter configuration (Lie & Farhat, 2007) and others.

It should be noted that there are two types of POD research being carried out at the moment. The first concerns the decomposition of flowfields observed in experiments in order to better understand the flow mechanisms and physics underlying these flows. The second type of research concerns the Reduced Order Modelling of unsteady Computational Fluid Dynamic (CFD) simulations or even, CFD/CSD (Computational Structural Dynamics) simulations,

in order to produce simplified but representative models that can be used in practical applications such as aircraft design.

The work of interest here is the of first type, i.e. the experimental work. It is usually combined with high-speed Particle Image Velocimetry (PIV) measurements, although there are examples of other instrumentation being used, such as hot wire rakes (Tutkun et al., 2008). The limitation of all research works published on the subject is that the models around which the flowfield is measured are always static or rotating at constant velocity. Additionally, only one source of flow unsteadiness is ever considered.

The objective of the present work is to expand the methodology of the application of POD to experimental flowfields. There are two aspects to this expansion:

1. Allow the models to oscillate. The source of the unsteadiness will then be the movement of the model, as well as any unsteadiness due to flow separation.
2. Study the interaction between the different sources of unsteadiness. In particular observe how the modes generated by one source of unsteadiness interact with the modes generated by the other. Determine if it is possible to separate the structural from the aerodynamic sources of unsteadiness.

2. Basics of Proper Orthogonal flow decomposition

Observation of an unsteady flow by PIV will, in general, yield M snapshots of a 2D section of the flowfield at times t_1, \dots, t_M . These snapshots will usually feature information on the $u(x, y, t)$ and $v(x, y, t)$ velocity vectors although other information can also be obtained (e.g. vorticity). The velocity vectors will be available on a spatial grid of size $n_y \times n_x$, i.e. there will be n_y gridpoints in the y direction with spacing δy and n_x in the x direction with spacing δx . Therefore, $u(x, y, t)$ and $v(x, y, t)$, will be available in discrete form, i.e. in the form of $n_y \times n_x \times M$ real arrays.

The time-averaged flow is represented by $(\bar{u}(x, y), \bar{v}(x, y))$, where

$$\bar{u}(x, y) = \frac{1}{M} \sum_{i=1}^M u(x, y, t_i)$$

$$\bar{v}(x, y) = \frac{1}{M} \sum_{i=1}^M v(x, y, t_i)$$

and the unsteady velocity components are obtained simply from

$$u'(x, y, t) = u(x, y, t) - \bar{u}(x, y)$$

$$v'(x, y, t) = v(x, y, t) - \bar{v}(x, y) \quad (2)$$

The Proper Orthogonal Decomposition procedure is then applied on the data matrix \mathbf{C} , the auto-correlation matrix of the total energy in the flow at every instance in time. For a continuous flow,

$$C(t_1, t_2) = \frac{1}{M} \int \int (u'(x, y, t_1)u'(x, y, t_2) + v'(x, y, t_1)v'(x, y, t_2)) dx dy \quad (3)$$

For a discrete flow, the integrals become summations. Using trapezoidal integration,

$$C_{i,j} = \frac{1}{M} \sum_{k=1}^{n_y-1} (G_{i,j,k} + G_{i,j,k+1}) \delta y / 2 \quad (4)$$

where $C_{i,j}$ is the element in the i th line and j th column of \mathbf{C} , $G_{i,j,k} = \sum_{l=1}^{n_x-1} (F_{i,j,k,l} + F_{i,j,k,l+1}) \delta x / 2$, $F_{i,j,k,l} = (u'_{k,l,i} u'_{k,l,j} + v'_{k,l,i} v'_{k,l,j})$ and the notation $u'_{k,l,i}$ is shorthand for $u'(x_k, y_l, t_i)$. Higher order integration schemes can also be used. The Proper Orthogonal Decomposition process requires the solution of the eigenvalue problem

$$\mathbf{C}\mathbf{A} = \lambda\mathbf{A} \quad (5)$$

where \mathbf{A} are the matrix of eigenvectors of the \mathbf{C} matrix and λ are its eigenvalues. If the eigenvectors are normalized in the form $\mathbf{a}_i / \sqrt{\lambda_i M}$, where \mathbf{a}_i is the i th column of \mathbf{A} , then they will form an orthonormal basis. The mode shapes $\phi_{u,i}$ and $\phi_{v,i}$ can be constructed from

$$\begin{aligned} \phi_{u,i}(x, y) &= \frac{1}{\sqrt{\lambda_i M}} \sum_{m=1}^M u'(x, y, t_m) a_{m,i} \\ \phi_{v,i}(x, y) &= \frac{1}{\sqrt{\lambda_i M}} \sum_{m=1}^M v'(x, y, t_m) a_{m,i} \end{aligned} \quad (6)$$

where $a_{m,i}$ is the m th element of the i th eigenvector of \mathbf{C} . The mode shapes are only functions of space but can be used to describe the unsteady flowfield when combined with the generalized coordinates $q_i(t)$, which can be obtained from

$$q_i(t) = \int \int (u'(x, y, t) \phi_{u,i}(x, y) + v'(x, y, t) \phi_{v,i}(x, y)) dx dy \quad (7)$$

or from the discrete version of this equation.

There are M eigenvalues and hence M sets of mode shapes and generalized coordinates. However, the aim of POD is to create a reduced order model, using only the first N modes that contain most of the fluctuating flow energy. To this end, the quantity $\lambda_i / \sum_{i=1}^M \lambda_i$ can be inspected, assuming that λ_i is ordered from highest to lowest eigenvalue. Kim et al. (2005) note that it should be $\sum_{i=1}^M \lambda_i = 1$, however this depends on the scaling used by the eigenvalue estimator, so looking at the ratio $\lambda_i / \sum_{i=1}^M \lambda_i$ is safer. If the first N eigenvalues are chosen, that have ratios higher than, say, 10% then a N mode model will be created.

Finally, the N -mode approximation of the complete velocity field can be reconstructed from the N retained modes using equation 1

$$\begin{aligned} u^*(x, y, t) &= \bar{u}(x, y) + \sum_{i=1}^N q_i(t) \phi_{u,i}(x, y) \\ v^*(x, y, t) &= \bar{v}(x, y) + \sum_{i=1}^N q_i(t) \phi_{v,i}(x, y) \end{aligned}$$

The POD procedure described above will be applied (with some modifications) to experimentally observed unsteady flows behind a circular cylinder at conditions both near to and far from resonance.

3. Experimental setup

The experiments were carried out in the multi-disciplinary low speed wind tunnel of the University of Liège. The Aeronautical test section of the wind tunnel was used, which measures $2\text{m} \times 1.5\text{m} \times 5\text{m}$ (width \times height \times length) and has a maximum airspeed of 60m/s .

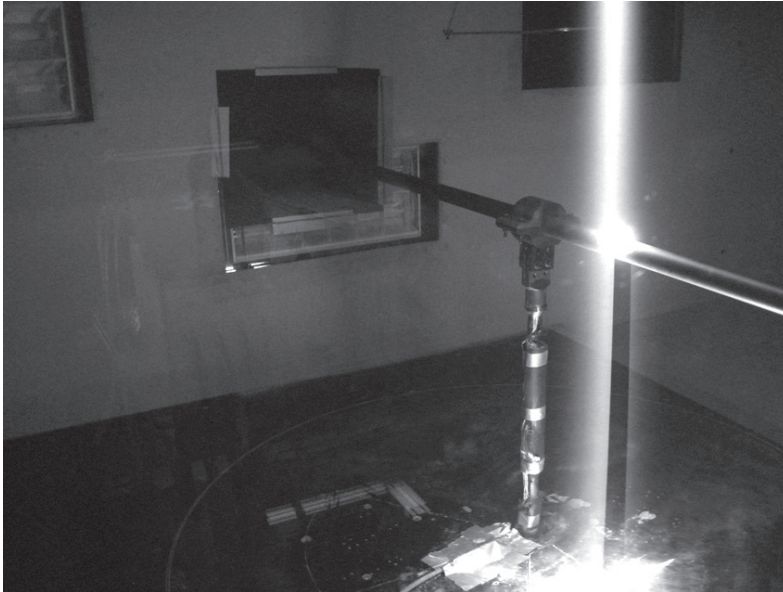


Fig. 1. Laser sheet illuminating 2D section of flow around a cylinder

A circular cylinder of 36mm diameter and 1.32m span was placed in the wind tunnel, supported by its mid-span point near the middle of the test section. The cylinder was made of aluminium tube and painted matt black. The cylinder is rigidly supported but is flexible itself. Its first symmetric bending mode has a frequency of around 70Hz. Therefore, it is expected that when the frequency of the Von Karman vortex street behind the cylinder matches the first bending frequency, the free ends of the cylinder will oscillate quite visibly. Away from resonance, the cylinder will be static. This setup is ideal for the purposes of the present investigation, as it allows the examination of the unsteady flow behind both a static and a vibrating object.

4. PIV system setup

The PIV system used for these experiments consists of the following components:

1. A Litron LDY301-PIV Q-switched laser system. It is a dual power, dual cavity laser with a wavelength of 527nm, switching at 1000Hz. The two laser beams contain $2 \times 10\text{mJ}$ of energy.
2. Optical modules for producing a laser sheet.
3. A Phantom V9.1 camera with a maximum resolution of 1600×1200 pixels at a frequency of 1KHz and 6GB of internal memory buffer.

4. A timer box for synchronizing the laser with the camera.
5. A seeding generator with 3 bar back pressure suitable for PIV particle generation.
6. Dantec Dynamics Studio PIV data acquisition and analysis software.
7. A high specification Personal Computer.

In practice, the system is capable of capturing PIV data in a window of around $13 \times 11\text{cm}$ at a frequency of 1000Hz.

The laser sheet was placed on the side of the cylinder nearest to the working section's observation window and aligned with the airflow, so as to illuminate a 2D section of flow around the cylinder. The laser sheet position can be seen in figure 1. Notice that the centre of the laser sheet lies aft of the cylinder. The very sharp shadow under the cylinder is also worth noting.

4.1 PIV results

Figure 2 shows a snapshot of the illuminated particles around the cylinder. It can be seen that the laser illuminates the aft upper section of the cylinder itself (white arc) as well as seeded particles on the upper surface of the cylinder and in the wake. Evidently, there are no illuminated particles in the shaded area under the cylinder.

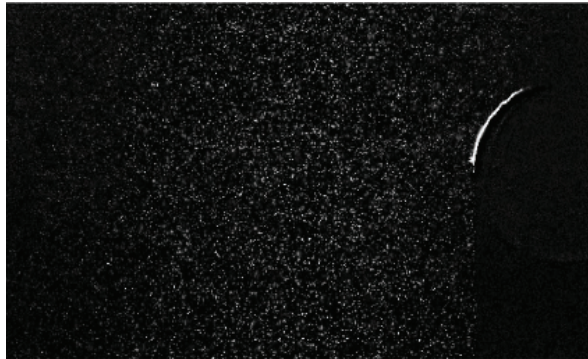


Fig. 2. Illuminated particles around the cylinder

The PIV system takes two such snapshots at a very short time interval, typically $1 - 1000\mu\text{s}$. A region of interest (ROI) is defined in the snapshots. This ROI is further divided into subregions (e.g. 64×64 pixels). The motion of the particles inside each subregion of the first snapshot is correlated to the second snapshot. The aim of the analysis is to decide where each subregion of photo 1 has moved to on photo 2. Thus, a velocity vector is placed in the centre of each subregion, representing the global motion of the particles inside the latter. The entire process is carried out by means of the Dynamics Studio PIV software and requires calibration data consisting of the free stream airspeed or a characteristic length, in this case the cylinder diameter.

The end result of the PIV data reduction process is a velocity vector field calculated at each instance in time for which the visualization took place, as shown in figure 3. The image correlation process can sometimes lead to the calculation of bad vectors (outliers); these are detected and replaced by averages of all the neighboring vectors.

PIV visualizations for the circular cylinder were carried out at airspeeds from 10 to 20m/s, at a sampling frequency of 1000Hz and sampling times from 0.1s to 4s. The recovered unsteady

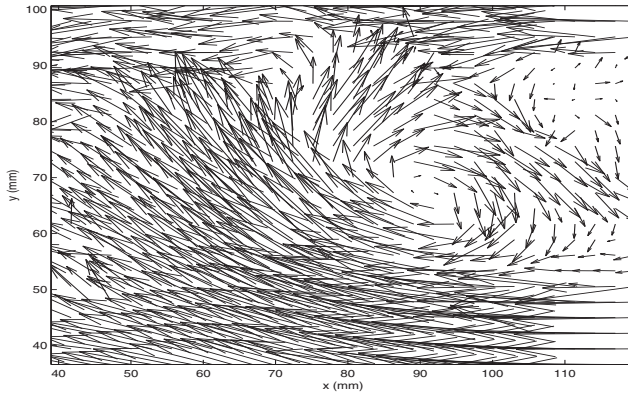


Fig. 3. Computed velocity vectors for a sample snapshot

vector fields had a resolution of 24 gridpoints in the y -direction and 41 in the x -direction. Therefore, the sizes of the u and v matrices ranged from $24 \times 41 \times 100$ to $24 \times 41 \times 4000$.

4.1.1 Flow frequency variation with airspeed

In order to verify that the PIV system and POD decomposition analysis are performing correctly, a large number of PIV measurements were carried out at airspeeds between 4m/s and 26m/s. The flow frequencies recovered by the POD method for all these measurements were then compared to the theoretical frequencies, assuming that the cylinder has a Strouhal number of 0.2. This comparison can be seen in figure 4, where the experimentally estimated frequencies are plotted as stars with error bars and the theoretical frequency is plotted as a dashed sloped line. The error bars represent the frequency increment, equal to the sampling frequency divided by the number of time measurements M and is equal to 2.02Hz.

Figure 4 shows that the frequencies estimated from the decomposed PIV measurements are in good agreement with the theoretical predictions. It can be concluded that both the instrumentation and the POD analysis were correctly operated. The two dotted lines in the figure represent the airspeed limits at which significant cylinder vibration amplitudes were observed. Indeed, resonance phenomena were observed at airspeeds between 13.5m/s and 18m/s, corresponding to vortex shedding frequencies of 70-105Hz. The lock-in phenomenon, whereby the flow frequency adapts itself to the structure's natural frequency throughout the resonance airspeed range, is not evident in this data. The reason for this absence of lock-in is that the measurements used for constructing figure 4 were taken close to the cylinder's midpoint, as seen in figure 1. At this location the amplitudes of the vertical vibration are small and have no impact on the shedding process. The frequency of the latter follows the linear Strouhal relation.

4.2 POD analysis

At the end of the PIV data treatment, a set of $u(x, y, t)$ and $v(x, y, t)$ matrices were obtained for each tested airspeed. These matrices were then analyzed using the POD procedure described in section 2. Sample results from three airspeeds are presented and discussed in this section. These are labeled as:

- Test 1: Free stream airspeed of 18.8m/s, sampling frequency of 1000Hz, sampling time of 0.298s, PIV laser sheet at 0.2m from the cylinder's midpoint.

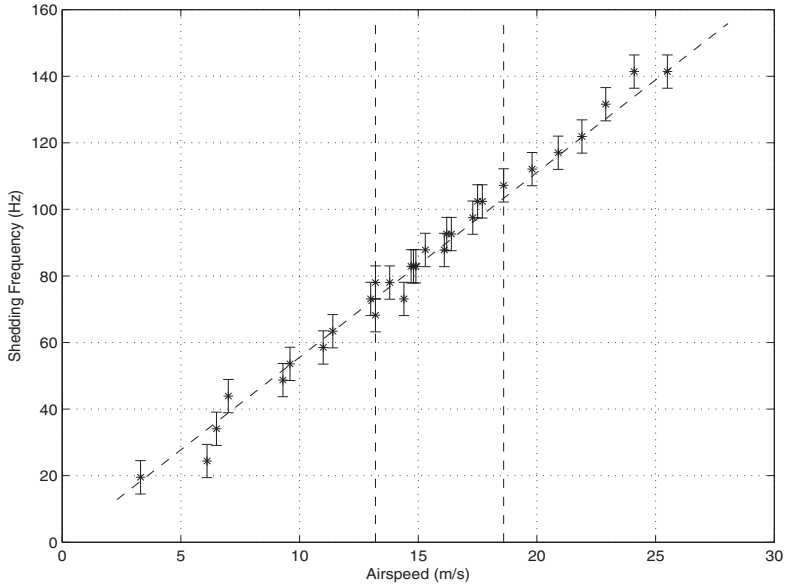


Fig. 4. Comparison of estimated frequencies to theoretical frequencies

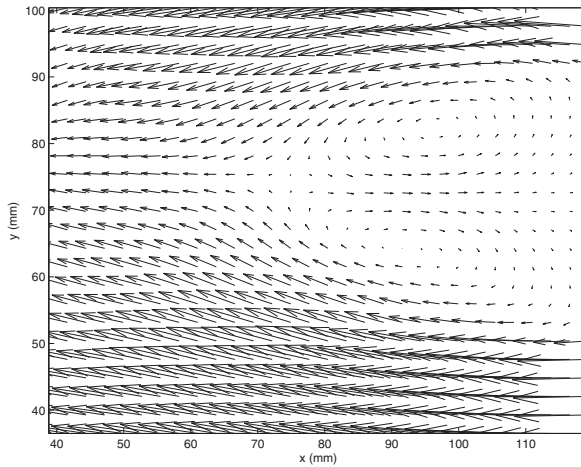


Fig. 5. Mean flow vectors for test 1

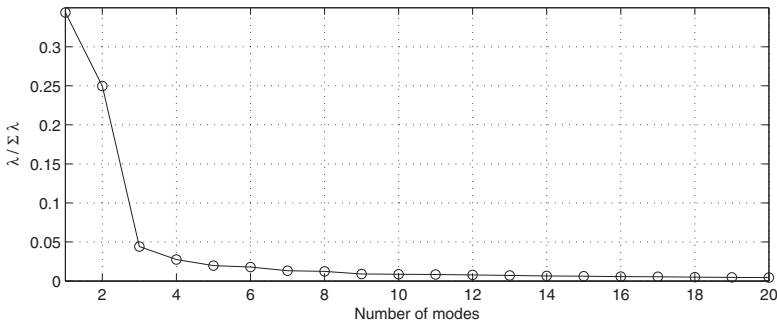


Fig. 6. Eigenvalue ratios for the first 20 eigenvalues for test 1

- Test 2: Free stream airspeed of 13m/s, sampling frequency of 1000Hz, sampling time of 0.099s, PIV laser sheet at 0.2m from the cylinder's midpoint.
- Test 3: Free stream airspeed of 13.9m/s, sampling frequency of 1000Hz, sampling time of 0.099s, PIV laser sheet at 0.2m from the cylinder's midpoint.
- Test 4: Free stream airspeed of 14.8m/s, sampling frequency of 1000Hz, sampling time of 0.099s, PIV laser sheet at 0.4m from the cylinder's midpoint

The Reynolds numbers for the three tests range from 40,000 to 55,000, which puts the flowfield in the 'transitional in the shear layer' category. In other words, the boundary layer on the cylinder's surface is expected to be laminar. After separation, there is periodic ejection of vortices in the wake, as in the case of laminar vortex shedding, but the shear layer causing this ejection is transitional, giving rise to small turbulent eddies.

Test 1 is used as the reference test, as it lies very far from aero-structural resonance and, therefore, there is negligible cylinder movement. Test 4 lies right on resonance and the cylinder vibrates significantly at the PIV measurement position. For all the tests, the first step in the POD procedure was to define the region of interest, so as not to include in the POD calculations the velocity vectors under the cylinder, which are not observable. The region of interest was therefore limited to a point just downstream of the cylinder.

4.2.1 Test 1

The next step in the POD procedure for Test 1 was to calculate the mean flow. This calculation involved the time averaging of the $u(x, y, t)$ and $v(x, y, t)$ matrices, leading to the mean flow shown in figure 5. It can be seen that the mean flow is essentially an area of slow, recirculating flow, located just behind the cylinder. In other words, it can be seen as the steady wake, to which an unsteady wake is superimposed.

Once the mean flow was subtracted from $u(x, y, t)$ and $v(x, y, t)$ the unsteady vector fields $u'(x, y, t)$ and $v'(x, y, t)$ were obtained and Proper Orthogonal Decomposition was applied. The eigenvalue ratios $\lambda_i / \sum_{i=1}^M \lambda_i$ obtained for the first 20 modes are shown in figure 6. It can be seen that only the first two eigenvalues have significant contributions to the total energy in the unsteady flow, of 35% and 25% respectively. All higher eigenvalues have contributions of less than 5% and can therefore be neglected.

The mode shapes associated to the two retained eigenvalues are shown in figure 7, plotted as filled contour plots. Subfigure 7(a) plots the values of $\phi_u(x, y)$ (left) and $\phi_v(x, y)$ (right) for mode 1 as a filled contour plot, black signifying a low value and white signifying a high

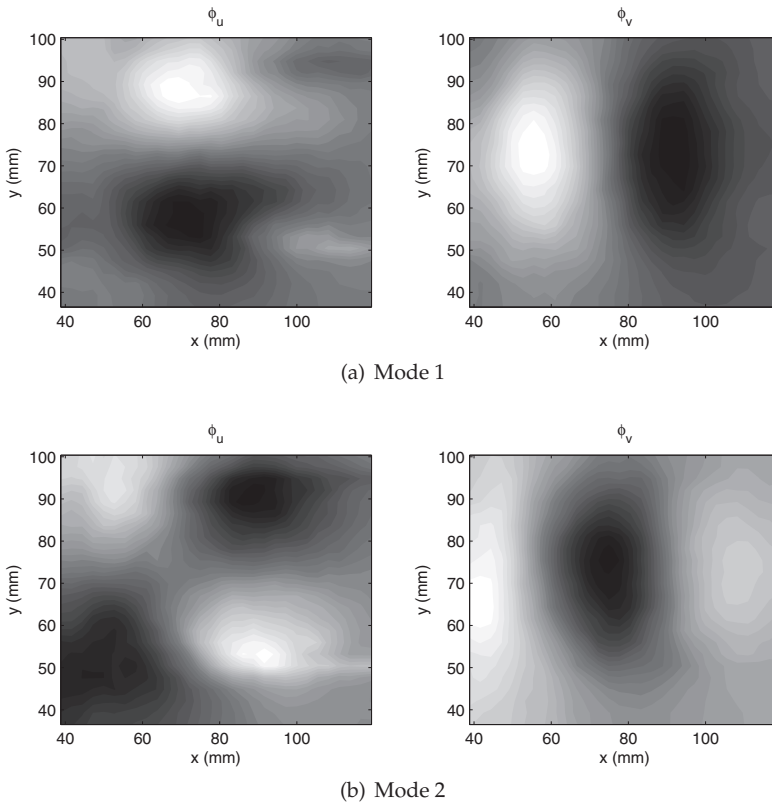


Fig. 7. The first two mode shapes for test 1

value. Subfigure 7(b) depicts the same information for mode 2. The horizontal distance between a maximum and a minimum grows from 30mm to 40mm with distance downstream. The vertical distance increases with downstream distance from 30mm to 46mm. If the mode shapes are assumed to be periodic, i.e. repeatable further downstream, then the two modes are separated by 1/4 of a period. It should be noted that the distances between maxima and minima are not constant because the measurement is just behind the cylinder, where there are large variations in the mean flow, as seen in figure 5. It is likely that the distances between maxima and minima are stabilized further downstream.

Figure 8 shows the variation in time of the two retained generalized coordinates. It can be seen that the two generalized coordinates have the same fundamental frequency of 107.5Hz. Furthermore, they are both subjected to a beating phenomenon, with the response amplitudes dropping momentarily at around 0.12s and again at around 0.3s. This beating demonstrates that the flow is quasi-periodic, with significant variations in amplitude occurring momentarily. This quasi-periodic nature is justified by the fact that the flow is transitional in the shear layer and there are small turbulent eddies absorbing some of the flow energy.

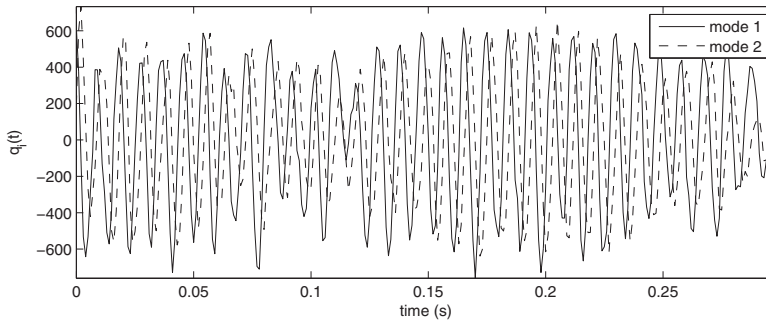


Fig. 8. Variation in time of the two retained generalized coordinates, Test 1

In fact, the two mode shapes of figure 7 are the dominant modes and can be viewed as ‘laminar’ modes. The modes that have been neglected can be viewed as ‘turbulent’ modes, which contain little energy over the complete time history but can momentarily absorb energy from the dominant modes. This is exactly what happens in the case of this test. At time indices of 0.12s and 0.3s, the response amplitude of modes 1 and 2 drops significantly; simultaneously the response amplitude of mode 3 increases visibly, as shown in figure 9(a), which plots the variation of generalized coordinate $q_3(t)$ with time. It can be clearly seen that the maxima of this mode occur at 0.12s and 0.3s.

The mode shape for mode 3 can be seen in figure 9(b). It is clear that this mode shape is significantly noisier than the mode shapes of the first two modes, shown in figure 7. This noisiness is consistent with the hypothesis that mode 3 represents turbulent flow energy. It should be mentioned that higher modes do not demonstrate any clear increases in amplitude at 0.12s and 0.3s. Therefore, a complete model of the flow of Test 1 will contain:

- two modes if only the laminar flow is of interest
- three modes if it is desired to account for some of the energy momentarily lost by the laminar modes

4.2.2 Test 2

Test 2 is similar to Test 1 in the sense that resonance is not occurring yet; however, the condition is much closer to resonance than Test 1 and the amplitude of vibration of the cylinder is small but noticeable. Under these circumstances, the effect of evaluating a mean flow and subtracting it from the total vector field must be revised. In effect, as the mean flow is the steady wake behind the cylinder, if the cylinder oscillates by a significant amount, then the concept of a steady wake is no longer valid and the mean flow should not be evaluated. In other words, while it is still possible to calculate values for \bar{u} and \bar{v} over the entire time history, these values will not be the same over a different time history. In essence, the movement of the cylinder is an excitation force that is applied to the fluid; it will respond at the excitation frequency and at higher harmonics but there will be no response component with zero frequency.

Nevertheless, if the amplitude of oscillation is very small, then evaluating and subtracting the mean flow will not cause big errors in the POD procedure. For Test 2, the POD method was applied twice, the first time after subtracting the mean flow and the second after subtracting only the wind tunnel free stream, U . In other words, in the first application the POD analysis

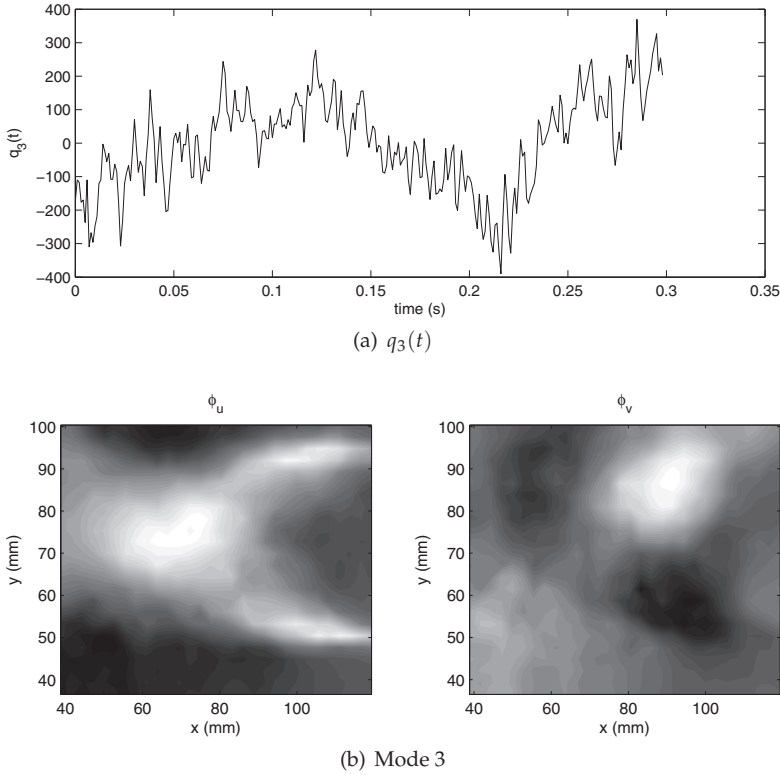


Fig. 9. The third mode for test 1

was carried out on u' and v' using equations 3 to 7 while in the second it was carried out on $u - U$ and v , such that

$$C(t_1, t_2) = \frac{1}{M} \int \int ((u(x, y, t_1) - U)(u(x, y, t_2) - U) + v(x, y, t_1)v(x, y, t_2)) dx dy \quad (8)$$

with

$$\begin{aligned} \phi_{u,i}(x, y) &= \frac{1}{\sqrt{\lambda_i M}} \sum_{m=1}^M (u(x, y, t_m) - U) a_{m,i} \\ \phi_{v,i}(x, y) &= \frac{1}{\sqrt{\lambda_i M}} \sum_{m=1}^M v(x, y, t_m) a_{m,i} \end{aligned} \quad (9)$$

and

$$q_i(t) = \int \int ((u(x, y, t) - U)\phi_{u,i}(x, y) + v(x, y, t)\phi_{v,i}(x, y)) dx dy \quad (10)$$

For the first application, the number of retained modes was 2, i.e. only the laminar unsteady flow modes were found to be significant; the resulting mode shapes were qualitatively similar to those obtained for Test 1 (figure 7). For the second application, the number of

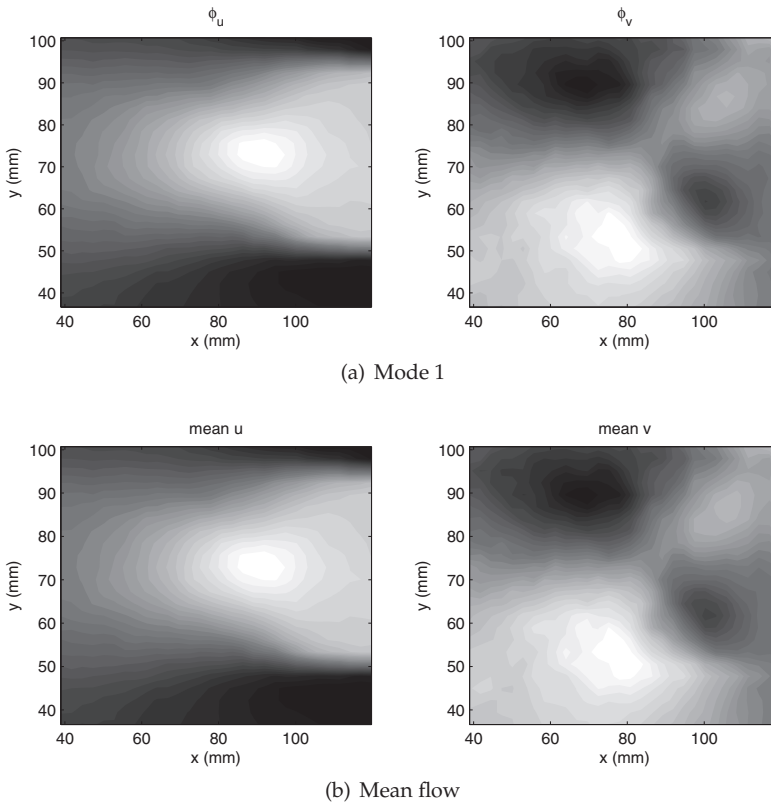


Fig. 10. The first mode shape for test 2 (top) compared to the mean flow (bottom)

retained modes was 3. The first mode represented the mean flow while the other two modes represented the laminar unsteady flow and were very similar to the modes of the first application and, consequently, of figure 7. It is interesting to compare the mean flow subtracted from the data in the first application to the first mode obtained from the second application. Figure 10 shows contour plots of the first mode $\phi_{u,1}$ and $\phi_{u,2}$ evaluated from the application of POD to $u - U$ and v (top two plots) and of the mean flow components \bar{u} and \bar{v} (bottom plots). It can be seen that the two sets of contour plots are very similar. Therefore, the POD procedure described by equations 8 to 10 will calculate the mean flow as the most energetic mode.

This is quite an interesting result because it suggests that there is no need to subtract the mean flow. If there is a steady component to the flow, then it will be identified automatically as the first mode. If there is no steady component, then equations 8 to 10 should be used anyway. Figure 11 shows the time response of the three resulting generalized coordinates. It can be seen that the generalized coordinate of the first mode is nearly constant with a value of around 600, while the coordinates of the other two modes oscillate around zero. It is clear that the POD procedure can differentiate between steady and unsteady responses.

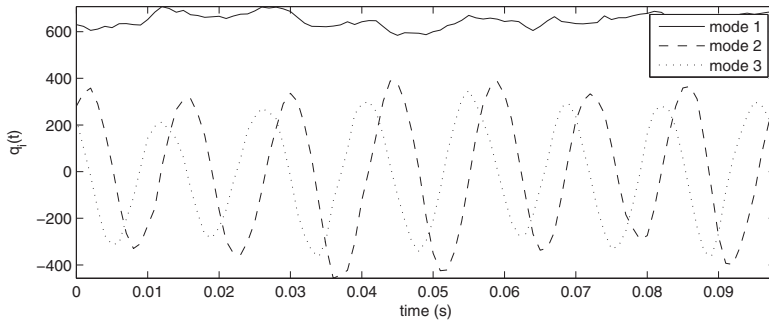


Fig. 11. Variation in time of the three retained generalized coordinates, Test 2

4.2.3 Test 3

For Test 3 the POD procedure was carried out only using equations 8 to 10. As mentioned before, Test 3 gave rise to significant amplitudes of cylinder vibration as the flow frequency was very close to a natural frequency of the cylinder. Again, three modes were retained, one representing a mean flow and two representing the laminar oscillating flow.

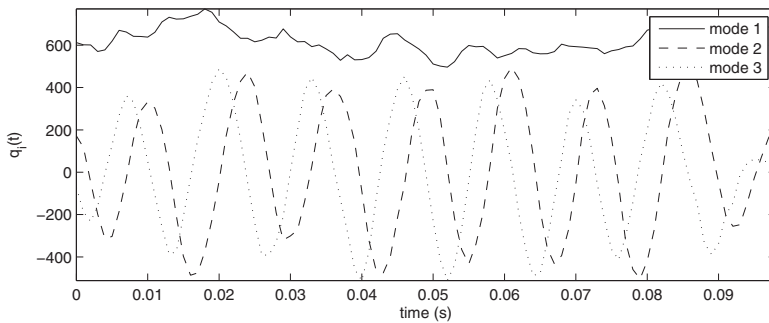


Fig. 12. Variation in time of the three retained generalized coordinates, Test 3

The response amplitudes of the three generalized coordinates were significantly higher than in the case of Test 2, as seen in figure 12. Even the generalized coordinate of mode 1 is far more unsteady, although its variation in time is not periodic. This aperiodic variation suggests that there is a component of the cylinder vibration in the flow data but it is of the same order as the turbulent disturbances and/or experimental error. This was indeed the case, as the measurement point was close to the cylinder's midpoint (see figure 1), therefore the local vibration amplitude was small, of the order of less than 1mm.

4.2.4 Test 4

The final test was carried out at a slightly higher airspeed but, crucially, the PIV laser sheet was positioned at a span-wise point further from the cylinder's midpoint than for the other three tests. At this particular span-wise position, the cylinder was vibrating significantly, with an amplitude of nearly 2mm and a frequency of 70.5Hz.

The POD procedure was again applied using equations 8 to 10, i.e. without subtracting the mean flow. The resulting mode shapes were similar to those obtained during Test 3. The

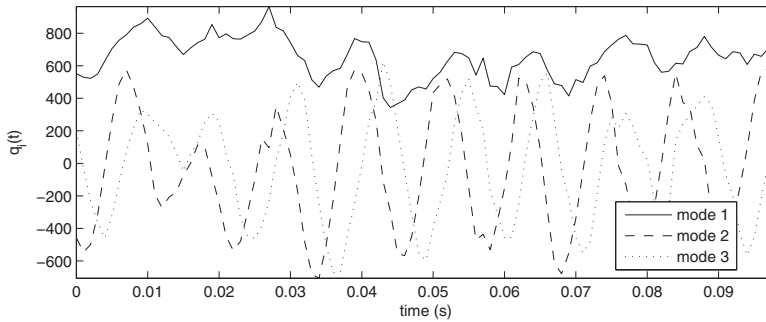


Fig. 13. Variation in time of the three retained generalized coordinates, Test 4

resulting generalized coordinates are plotted on figure 13. It can be clearly seen that the response of the first generalized coordinate is now much more oscillatory than in the case of figure 12. Furthermore, despite the randomness of this response, there is a clear periodic component at a frequency close to that of the oscillating modes.

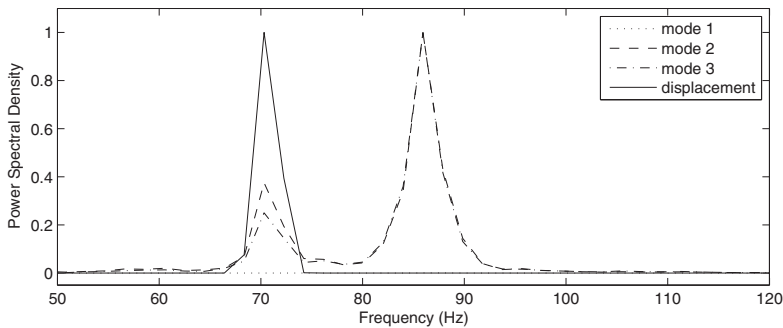


Fig. 14. Power Spectral Density plots of the generalized coordinates and the cylinder displacement.

The observations of Test 4 suggest that POD can decompose flowfields that feature unsteadiness due to the presence of both separated flow and structural motion of the wind tunnel model. However, for this decomposition to be successful, the response amplitude of the structure must be significantly higher than the size of the turbulent eddies. In such cases, straightforward POD will result in generalized coordinates that contain the response frequencies of both the separated flow and the structural motion. Figure 14 shows Power Spectral Densities (PSD) of the $q_i(t)$ and $z(t)$ signals, $z(t)$ being the vertical displacement time history of the cylinder at the PIV measurement position. The PSDs were calculated using the Welch method, with a Hamming window 512 samples long and 50% overlap. The cylinder's displacement response clearly contains only one frequency component at 70.5Hz. The generalized coordinates feature two frequency components, one at 70.5Hz and a stronger one at 85.9Hz. It can be inferred that 70.5Hz is the structural response frequency while 85.9Hz is the vortex shedding frequency. The Strouhal frequency at the Test 4 airspeed is 82.2Hz if a Strouhal number of 0.2 is assumed (see figure 4), i.e. quite close to 85.9Hz.

The generalized coordinates can be seen as the responses in time of the fluid due to both flow unsteadiness and cylinder motion. Furthermore, the cylinder motion can be seen as an external excitation acting on the fluid. Therefore, it is possible to set up an input-output POD model, whereby the input is the cylinder motion and the outputs are the generalized coordinates. Frequency Response Functions (FRF) can then be created of the form

$$H_i(\omega) = \frac{Q_i(\omega)}{Z(\omega)} \quad (11)$$

where H_i is the i th FRF, Q_i is the i th generalized coordinate in the frequency domain, Z is the cylinder displacement in the frequency domain and ω is the radial frequency. Such FRFs can be estimated using a Welch-type windowed approach and involving cross and auto-correlations of the outputs and input.

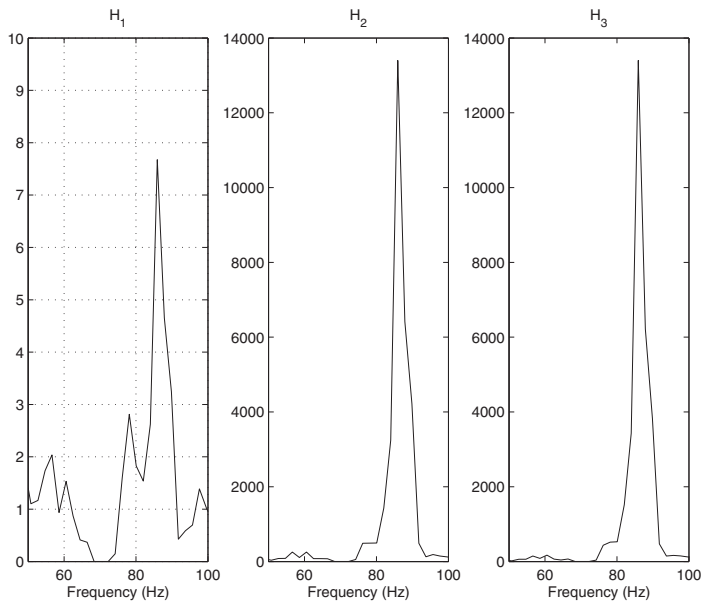


Fig. 15. FRFs between the generalized coordinates and the cylinder displacement.

Figure 15 shows the FRFs estimated for the first three modes of Test 4. It can be seen that the main frequency component of all FRFs is the vortex shedding frequency at 85.9Hz, in the frequency range between 50 and 100Hz. The FRF of mode 1, H_1 , features several other peaks but these are most likely noise; for this mode the main frequency component lies at 0Hz, since the mode mainly reflects the mean flow.

4.2.5 Mode shapes variation with airspeed

Here, the variation of the modes shapes with airspeed will be discussed. Only the free stream is subtracted from the local velocity field for the results in this subsection, not the mean flow. It was observed that the first three modes, i.e. the steady flow and the two laminar modes, change very little in shape with airspeed.

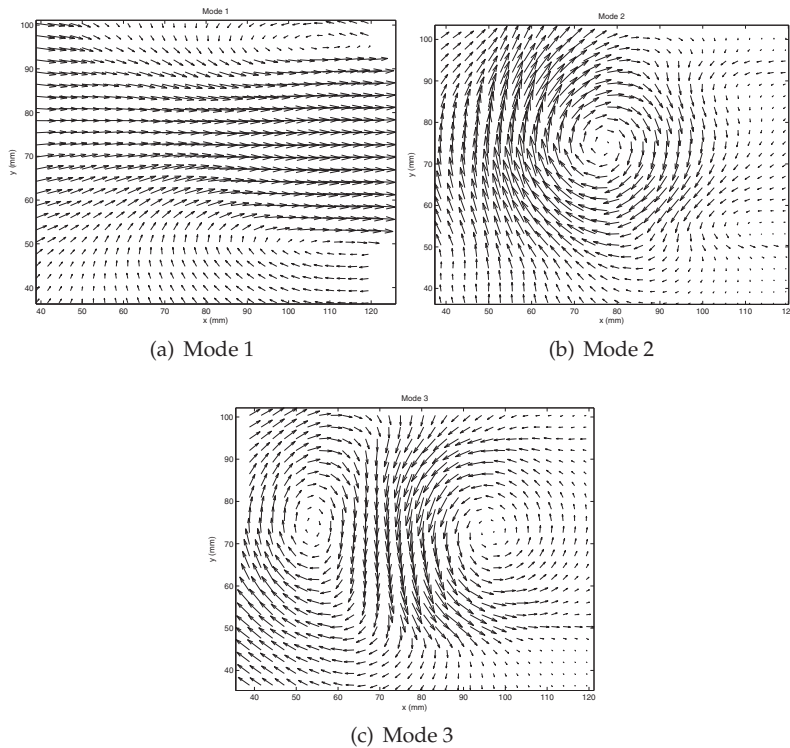


Fig. 16. Vector plots of the first three mode shapes

Figure 16 shows plots of the first three modes in vector form, whereby the vectors' horizontal component is taken as $\phi_{u,i}(x, y)$ and the vertical one as $\phi_{v,i}(x, y)$. Mode one (figure 16(a)) consists of two areas of recirculation behind the top and the bottom of the cylinder. Between them, they cause a significant area of flow towards the cylinder with a height approximately equal to the cylinder's diameter. Mode two (figure 16(b)) consists of a large vortex, positioned approximately one diameter behind the cylinder and centered on the cylinder's centerline. It is accompanied by two much smaller areas of recirculation lying just behind the top and bottom of the cylinder. Mode 3 (figure 16(c)) consists of two counter-rotating vortices at approximately half a diameter (the strongest) and one diameter (the weakest) behind the cylinder. They are both lying on the cylinder's centerline. As mentioned above, these three modes remain largely unaffected by the airspeed.

Figure 17 shows vector plots of mode 4 obtained for the four different tests, i.e. at four different airspeeds. It can be seen that all mode shapes are different. The mode shape for Test 1 consists of four vortices; for Test 2 of three vortices, one of which is very weak; for Test 3 the mode shape consists of three vortices again but in a different arrangement; finally, for Test 4 the number of vortices is difficult to determine because they are quite weak and small.

The reason for the change in mode shape 4 with test airspeed may be numerical rather than physical. In fact, mode shapes very similar to that of figure 17(a) appeared as mode 6 in Test 3 and mode 5 in Test 4. Therefore, the same mode shape can be preserved but its

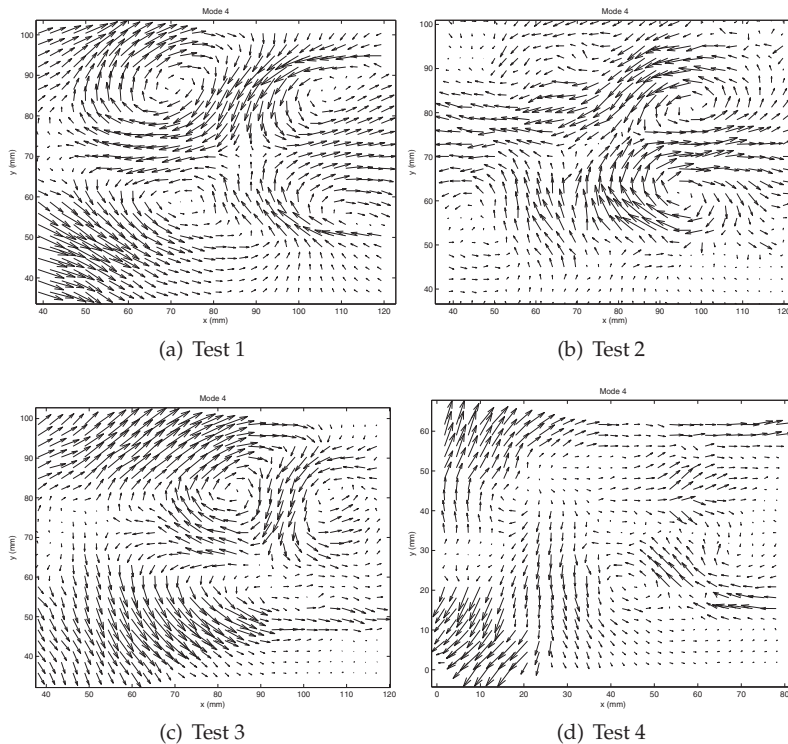


Fig. 17. Vector plots of the fourth mode shape for the four different tests

relative importance changes between tests. This phenomenon may provide justification for the assertion presented here concerning the higher modes, i.e. that modes higher than 3 represent transitional effects.

5. Conclusions

The feasibility of applying Proper Orthogonal Decomposition to experimentally measured flows around vibrating structures has been demonstrated. It has been shown that this type of decomposition analysis can provide some very interesting data about the observed flows, such as the dominant mode shapes and frequencies. Furthermore, it was shown that structural vibrations can be detected by the POD procedure applied on PIV flow visualization data using an output-only approach.

By considering the cylinder structural response as a forcing function, it is possible to create input-output POD models, whereby the generalized coordinates can be obtained from Frequency Response Functions relating the cylinder displacement response to the generalized coordinates themselves. It is shown that such FRFs feature two main frequency components, the mean flow frequency (i.e. 0Hz) and the vortex shedding frequency. Therefore, they are independent of the structural response frequency.

6. References

- Cipolla, K. M., Liakopoulos, A. & Rockwell, D. (1998). Quantitative imaging in proper orthogonal decomposition of flow past a delta wing, *AIAA Journal* 36(7): 1247–1255.
- Dowell, E. H., Hall, K. C. & Romanowski, M. C. (1998). Eigenmode analysis in unsteady aerodynamics: Reduced order models, *Applied Mechanics Reviews* 50(6): 371–385.
- Hall, K. C. (1994). Eigenanalysis of unsteady flows about airfoils, cascades, and wings, *AIAA Journal* 32(12): 2426–2432.
- Kim, Y., Rockwell, D. & Liakopoulos, A. (2005). Vortex buffeting of aircraft tail: Interpretation via proper orthogonal decomposition, *AIAA Journal* 43(3): 550–559.
- Lie, T. & Farhat, C. (2007). Adaptation of aeroelastic reduced-order models and application to an F-16 configuration, *AIAA Journal* 45(6): 1244–1257.
- Lumley, J. L. (1967). Atmospheric turbulence and radio wave propagation, Nauka, Moscow, pp. 116–178.
- Tang, D., Kholodar, D., Juang, J. & Dowell, E. H. (2001). System identification and proper orthogonal decomposition method applied to unsteady aerodynamics, *AIAA Journal* 39(8): 1569–1576.
- Tutkun, M., Johansson, P. B. V. & George, W. K. (2008). Three-component vectorial proper orthogonal decomposition of axisymmetric wake behind a disk, *AIAA Journal* 46(5): 1118–1134.

Wind Tunnel Testing of Pneumatic Artificial Muscles for Control Surface Actuation

Curt S. Kothera¹ and Norman M. Wereley²

¹*Techno-Sciences, Inc.*

²*University of Maryland
USA*

1. Introduction

Control surfaces, such as trailing-edge flaps, provide a means to dynamically alter the aerodynamic characteristics of aircraft for primary flight control, secondary vibration control, and even higher frequency noise control. While the development of several novel technologies has been explored, many practical implementation barriers still exist for a single actuation system to serve all three of these objectives. This is particularly true for rotorcraft, where the demands of the harsh rotary and vibratory environment are severe in terms of actuator force and displacement, bandwidth limitations, life cycle concerns, and physical volume available. Accordingly, it has been assumed that on-blade active controls of a rotorcraft would be subject to the most stringent requirements in the subsonic flight regime, and if a control surface actuation technology could survive here, it could be reasonably applied to a fixed wing aircraft. A brief account of the current state-of-the-art for rotorcraft blade controls follows.

Helicopter rotors typically operate in a highly unsteady aerodynamic environment. In forward flight, the rotor blade sections experience large variations in angle-of-attack over one revolution. This is the primary source of performance degradation, such as high vibration and retreating blade stall. Actively changing the angle-of-attack of the blade sections as a function of blade azimuth has been shown to significantly alleviate vibration levels, as well as improve aerodynamic performance of the rotor (Straub et al., 2000). The change in angle-of-attack can be accomplished in a variety of ways. Implementation of high bandwidth hydraulic actuators in the rotating frame has demonstrated the ability to actively change the root pitch of the rotor blades and has since been demonstrated in both scale models (Lorber et al., 2001) and full scale tests (Arnold & Strecker, 2002). Another approach is to vary the aerodynamic forces on the blades by dynamically changing the geometry of the airfoil sections. This can be accomplished through actively controlling blade twist, airfoil camber, or through the use of trailing-edge flaps (Hall & Wereley, 1993). Recent advances in adaptive materials have led to a variety of schemes for on-blade actuation in these areas (Chopra, 2000). Some of these include piezoelectric innovations such as adaptive twist of the rotor blade (Chen & Chopra, 1997; Chen et al., 2001; Shin et al., 2005), trailing-edge flaps (Straub et al., 2001; Fulton, 2000; Fulton, 2005), and active camber control (Konstanzer et al., 2001; Nissly et al., 2005).

In comparing these approaches to active rotor systems, there are potential drawbacks, however. For instance, implementation of hydraulic systems in the rotating frame of

production helicopters is a challenging task due to the complexity of the system, the increase in maintenance associated with the large number of moving parts, as well as the hydraulic slip ring, and the added on-blade mass associated with the weight of the hydraulic fluid and piping. Considering the active blade twist concept, there is also a large weight penalty due to the distributed nature of the actuators. There are also several unanswered questions as to whether active material solutions like piezoelectrics can survive in the operational environment, whether they have sufficient fatigue life for practical consideration, or whether they are properly scaled for operating over broad deflection and frequency ranges in full size rotors. Despite this, there have been numerous developments aimed at demonstrating the potential that active materials have for full scale rotors. Most notable is the piezoelectric actuator work conducted independently by Boeing and Eurocopter. Both using piezoelectric actuators to drive trailing-edge flaps on rotor blades, the Boeing development led to full scale whirl testing for vibration control (Straub et al., 2004) and a full scale wind tunnel test for noise reduction (Straub et al., 2009), and the Eurocopter development led to full scale flight testing for vibration control (Roth et al., 2006; Dieterich et al., 2006).

Trailing-edge flaps provide localized actuation and can generate significant control authority, but these discrete control surfaces do increase drag from the discontinuities and abrupt changes in airfoil contour. The active camber control concept alleviates this issue by varying the camber of the airfoil to produce a conformal shape change. There are several technical barriers that exist in actual implementation, such as the development of a flexible skin and supporting core that can withstand the harsh rotating environment of a helicopter. These topics are beginning to be addressed in the fixed frame, such as in unmanned air vehicles (Flanagan et al., 2007; Bubert et al., 2010; Olympio & Gandhi, 2010), but the technology has not reached the maturity level required for rotorcraft. Therefore, it appears that the trailing-edge flap may be the leading candidate control scheme for active rotors given the current state-of-the-art in practical actuation strategies.

Using these drawbacks as motivation to investigate alternative approaches to active aerodynamic control, a less conventional, yet properly scalable, approach to trailing-edge flap actuation has been developed and tested, and it employs Pneumatic Artificial Muscles, or PAMs, as actuators (Kothera et al., 2010). These actuators, originally developed for orthotic devices in the 1950s by J.L. McKibben (Gaylord, 1958; Schulte, 1961), typically contract in response to an increase in internal pressure, and have been used in robotic applications (Tondou et al., 1994; Medrano-Cerda et al., 1995; Daerden & Lefeber, 2002). Typically constructed of an elastomeric bladder surrounded by a braided sleeve, the stroke in these low cost and light weight actuators comes from re-orientation of the stiff braid fibers as the bladder expands radially. Previous research with these devices has experimentally confirmed their applicability to trailing-edge flaps in both the fixed frame (Woods et al., 2007; Kothera et al., 2008; Woods et al., 2010a) and the rotating frame (Bubert et al., 2007; Woods et al., 2010b). The development of and results from these fixed-frame tests will be presented here from two different mechanical configurations and loading conditions, as a step toward demonstrating the feasibility of using PAM actuators for aerospace applications. The next section will discuss the general system design, which will be followed by a discussion of bench-top testing results. Then the wind tunnel test article development is shown, along with experimental test data.

2. System design

Three different PAM actuation systems were designed, built, and tested, with experimental evaluations taking place first on the bench and then moving on to a wind tunnel. In each case, the aerodynamic hinge moment was predicted first and then the design of the actuation mechanism followed.

2.1 Aerodynamic prediction

The actuation system design used two-dimensional thin airfoil theory to predict the hinge moments that were used in sizing the actuators and bench-test loading springs to simulate the aerodynamic hinge moments. Environmental parameters used in the calculations are those of Sea Level Standard (SLS), which have a temperature of $T = 288$ K, pressure of $P = 101.3$ kPa, and air density of $\rho = 1.225$ kg/m³. The maximum speed of the Glenn L. Martin wind tunnel (GLMWT) at the University of Maryland is Mach 0.3, so this was also used in the design as a maximum free-stream condition, and a reasonable angle-of-attack of $\alpha = 6^\circ$ was also incorporated. It was assumed in this loading mechanism design that there was no flow separation over the airfoil and that the gap between the flap and the airfoil was sealed. The most important quantity for prediction in terms of sizing the actuation system is the hinge moment. This can be calculated according to

$$c_h = c_{h\alpha}\alpha + c_{hf}$$

$$H = \frac{1}{2}\rho v^2 S_f c_f c_h,$$

where c_h is the hinge moment coefficient, $c_{h\alpha}$ is the hinge coefficient due to angle-of-attack, c_{hf} is the hinge coefficient due to flap deflection, H is the actual hinge moment, v is the wind speed, S_f is the flap area, and c_f is the chord of the flap. For the angle-of-attack effects, tabulated airfoil data can be used with the equation

$$c_{h\alpha} = (b_1)_0^* + 2 \left[(a_1)_{0T}^* - (a_1)_0^* \right] \tan(0.5\tau - t/c),$$

where (b_1) is the rate of change of hinge moment coefficient with incidence, the (a_1) terms are related to the lift-curve slope, τ is the trailing-edge angle, and t/c is the thickness ratio (Etkin, 1982). The effect on the hinge moment due to flap deflection is computed by

$$c_{hf} = \frac{dc_h}{dc_l} c_l + \frac{dc_h}{d\delta} \delta,$$

where dc_h/dc_l is the rate of change of the hinge moment coefficient with respect to the change in lift coefficient, $dc_h/d\delta$ is the rate of change of the hinge moment coefficient with respect to the change in flap deflection, c_l is the lift coefficient, and δ is the flap deflection (Abbott & von Doenhoff, 1959). Because this term depends on the lift coefficient, its computation was also required in the prediction. For the current case with a flap on the trailing-edge, added lifting effects from the flap on the lift coefficient can be approximated as

$$c_l = c_{l\alpha}(\alpha + k\delta),$$

where k is the fraction for how the flap deflection angle changes the effective angle-of-attack of the airfoil (Eastman & Pinkerton, 1930). Here, the lift coefficient due to angle-of-attack is estimated with Mach scaling according to

$$c_{l\alpha} = \frac{2\pi}{\sqrt{1-M^2}},$$

where M is the Mach number. The denominator in this equation is commonly denoted as the parameter β .

As was mentioned, a total of three PAM-flap systems were evaluated. Table 1 lists the key design parameters for each and defines each with a "system number," which will be used throughout to more easily identify the results being shown. As can be seen, all three systems were sized for NACA 0012 airfoils with nominal angles-of-attack of 6 degrees. It should also be noted that each successive system was designed and tested for a higher Mach number. The first two systems were identical in terms of the overall model size and flap size, with the second containing stronger PAM actuators for the higher air loads. The third system was designed for an even higher wind speed and a smaller airfoil section to better illustrate the capability of the PAM actuators for scalability and high performance.

System No.	1	2	3
Wind Speed (M)	0.1	0.3	0.56
Angle-of-Attack (deg)	6	6	6
Airfoil Type	NACA 0012	NACA 0012	NACA 0012
Airfoil Chord (in)	21	21	10.5
Flap Chord (in)	3.15	3.15	1.61
Flap Span (in)	10	10	34

Table 1. Details of specific trailing-edge flap systems

Using the aerodynamic equations listed above with the airfoil specifics and wind speeds in Table 1 led to predictions of the hinge moments that would need to be generated by the PAM actuation systems to deflect the various flaps. Figure 1 displays the simulation results for the noted systems and conditions. In each set of results, the estimated, bi-directional hinge moment contributions are shown from the airfoil angle-of-attack (green) and the flap deflection (red), along with the summed total (blue). Figure 1(a) shows the hinge moment for system 1 at the design condition, Figure 1(b) shows the hinge moment for system 2 at the design condition, and Figure 1(c) shows the hinge moment for system 3 at the design condition. Figure 1(d) has also been included to estimate the wind tunnel test condition for system 3. While designed for Mach 0.56, the test facility has a maximum wind speed of only Mach 0.3, so the designed actuation system was bench tested to the full spring-simulated aerodynamic stiffness, but it was wind tunnel tested to a reduced load with input pressure scaled accordingly. In order to meet the goal of at least 10 degrees of flap deflection, the PAM actuators must be able to produce 2.2 in-lb, 23 in-lb, and 70 in-lb for the noted design conditions of systems 1 - 3, respectively. Being that system 3 would be designed for operating at Mach 0.56, it would have little trouble meeting the reduced hinge moment requirement of only 22 in-lb for the wind tunnel test.

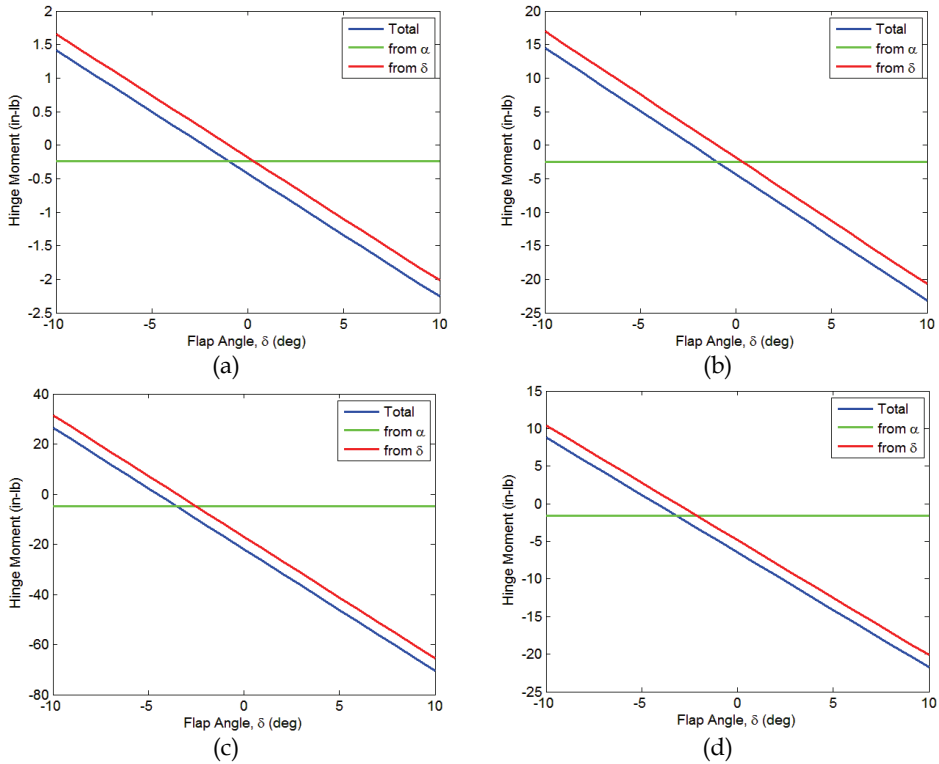


Fig. 1. Hinge moment predictions for actuation system designs – (a) system 1; (b) system 2; (c) system 3 bench-top; (d) system 3 wind tunnel

2.2 Actuator design

For the most part, the PAM actuation systems were sized to fit entirely within the airfoil contour. A schematic diagram of how the PAM system functions is provided in Figure 2. In this figure, the upper PAM is inactive (open to atmosphere, $P_1 = 0$) and the lower PAM is active (pressurized, $P_2 > 0$). The basic operation of a PAM actuator is to produce a contractile stroke upon internal pressurization. This stroke is the result of radial expansion of the elastomeric bladder, which is surrounded by a double helical weave of stiff fibers (e.g., polyethylene terephthalate - PET). As the softer bladder expands, the stiff fibers maintain their length and reorient themselves to accommodate the radial expansion. Consequently, the length of the device decreases. Also as indicated in the figure, any time pressure in one of the PAMs exceeds that in the other antagonistic PAM, a moment is generated about the flap hinge. The case shown is $P_1 < P_2$, which causes the flap to deflect in the downward direction.

There are two key equations for predicting the deflections of the antagonistic PAM actuation system. The first is the arc length formula

$$\frac{\Delta L}{r} = \frac{L_1 - L_2}{r} = \delta,$$

where L_1 is the length of the inactive PAM, L_2 is the length of the active PAM, and r is the hinge radius. These are all labeled in Figure 2 with the convention that downward flap deflection angles are positive and upward flap deflection angles are negative.

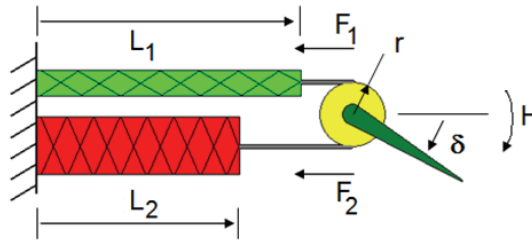


Fig. 2. Diagram of bi-directional PAM-flap actuator

The second equation considers the available actuation force by

$$\Delta F = F_2 - F_1 = \frac{H}{r},$$

where F_1 is the inactive PAM force (e.g., at 0 psi), F_2 is the active PAM force, and H is the hinge moment generated on the flap. For bi-directional operation of the flap, an antagonistic actuator arrangement is typically preferred.

Based on these actuator design equations and the aerodynamic hinge moment predictions from section 2.1, an in-house database of PAM actuator performance data was consulted to select the actuator characteristics best suited to each of the three systems. Table 2 displays the results of this actuator sizing analysis. For the first two systems, which are essentially the same except for the increased strength of the second, a chordwise PAM orientation was selected. This means that the length and stroke direction of the PAM actuators is along the airfoil chord, which was made possible by the large airfoil section (21-in chord). System 3 could not use chordwise actuators because of the higher forces required and the smaller size of the airfoil section. In this case, a spanwise orientation was selected, whereby the spanwise pulling motion of the PAM actuators is transferred into chordwise motion to deflect the flap through the use of a kinematic mechanism. While adding complexity and increasing the part count, having a mechanism does allow for consideration of mechanical advantage trade-offs to better tune system performance. For instance, when comparing the system 2 and 3 actuators, it can be seen that larger diameter PAMs were used for system 2 although the expected loads were smaller here than for system 3. Note that it is a general design rule for PAMs with the same braid angle that larger diameter actuators will produce more force for a given pressure. This use of smaller diameter PAMs of essentially the same braid angle was facilitated by the mechanism, where stroke could be traded for force. As indicated in the table, the PAMs for system 3 are over 9 inches long, whereas the PAMs for system 2 are just over 3 inches in active length.

Force-contraction data was collected from experiments conducted on a servo-hydraulic load frame. For each case, the PAM actuator was installed in the machine at its resting length, as shown in Figure 3(a). Next, the noted pressure was applied and held constant throughout the test. Immediately after the pressure was applied, the actuator blocked force measurement was recorded. Then, the actuator was allowed to contract slowly, or quasi-statically, to the point where no force was measured. This point is known as the free

System No.	1	2	3
Orientation	Chordwise	Chordwise	Spanwise
No. PAM Pairs	1	2	1
Diameter (in)	0.5	1.0	0.625
Active Length (in)	3.15	3.15	9.10
Resting Braid Angle (deg)	47	60	61
Braid Material	PET	PET	Kevlar
Bladder Material	Latex	Latex	Latex
Mechanical Advantage	1	1	1.15

Table 2. Details of specific PAM actuators selected for system designs



Fig. 3. Characterization testing of PAM actuator - (a) resting length; (b) free contraction

contraction value and is shown in Figure 3(b). After recording this value, the PAM actuator was stretched back to its resting length and the test was stopped. Typical performance data from each of the three selected PAM configurations is provided in Figure 4 at various pressure settings. Note that the x-axis data is presented as the non-dimensional contraction percentage. For the range of PAM lengths considered in this work, it has been shown that contraction percentage is largely independent of PAM length for a given diameter and braid angle. As an example, a particular PAM at a given pressure may have a free contraction of 25%. This actuator with a 4-in resting length would thereby have a free contraction of 1 inch, whereas a 12-in resting length actuator would have a free contraction of 3 inches.

It can be seen in Figure 4 that both force and contraction increase with pressure. For the performance metric of blocked force (measured force with 0% contraction, i.e., resting length and maximum possible force), the increase in force is linear with pressure, but the same is not true for the performance metric of free contraction (measured contraction with 0 lb force, i.e., maximum possible stroke). The free contraction increases with pressure, but tends to roll off as a maximum limit is approached. These trends are valid, of course, only over the pressure range which does not lead to yield in the braid fibres. It should be noted here that our tests have shown that the PET braid does not begin to yield until approximately 200 psi and the yield point for the Kevlar braid is over 1000 psi. Given that the three system designs here are all intended to operate below 100 psi, a more than adequate safety margin exists for burst failure. Another characteristic to mention in regard to the typical force-contraction

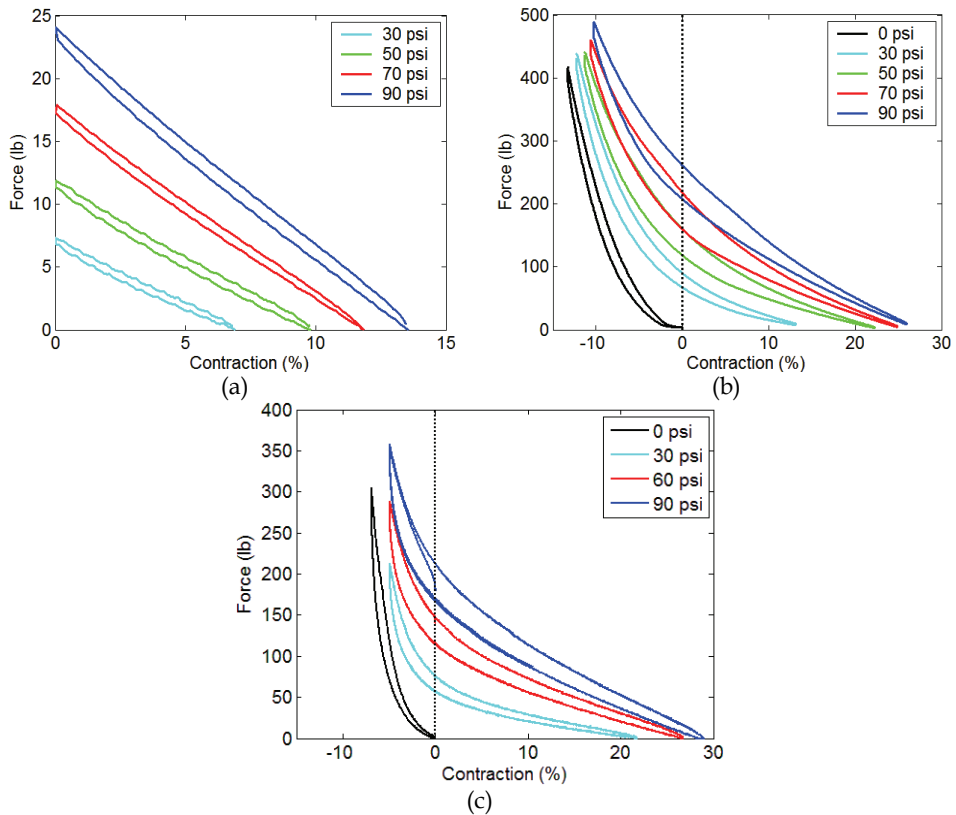


Fig. 4. Performance data from PAM actuators selected for system designs – (a) system 1; (b) system 2; (c) system 3

behaviour of PAM actuators is that some measure of hysteresis does exist in the loop. Despite the noticeable hysteresis, average values and a linear force-contraction approximation between blocked force and free contraction may be sufficient for initial system design and component sizing exercises. To state the maximum values of blocked force and free contraction (at 90 psi) for the system 1 – 3 actuators, respectively, we have 24 lb with 14%, 250 lb with 27%, and 200 lb with 29%.

3. Bench-top testing & validation

3.1 Experimental setup

To evaluate the PAM trailing-edge flap actuation systems prior to entering a wind tunnel environment, each of the three actuation systems was tested on a laboratory bench. Figure 5 shows the test setups that were designed, fabricated, and tested. First in Figure 5(a) is a system sized for low subsonic air loads with the single pair of antagonistic PAM actuators (system 1) oriented along the chord of the airfoil. Here, the compressed air enters and exits the PAM actuators from their end near the upper-right corner of the photograph. Two aluminum extensions are at their other end and are instrumented with resistive strain gages

for measurement purposes. Representative inertia is mounted on the axis of flap rotation and a bending spring is attached to simulate aerodynamic stiffness. Figure 5(b) shows a similar arrangement with chord-oriented PAM actuators, but this system has two antagonistic pairs of larger PAM actuators (system 2) to increase the quasi-static flap deflection output. It can be seen in the figure that the PAMs attach to the hinge from one side and a spring loading mechanism attaches to the hinge axis from the other side. Linear extension springs were used for this test. Figure 5(c) shows an antagonistic pair of PAM actuators intended for spanwise orientation in the airfoil section, which uses a mechanism (not pictured) to turn the actuator work into chordwise motion that rotates the flap about its hinge axis (system 3). An inertial element was attached to the top of the axis of rotation here and linear extension springs were connected at a different radius than the PAMs to account for the mechanism that would be installed in the airfoil section. Also note that the difference in physical appearance of the PAMs from system 1 and 2 (black) to those in system 3 (yellow) is due to the use of a different braid material.

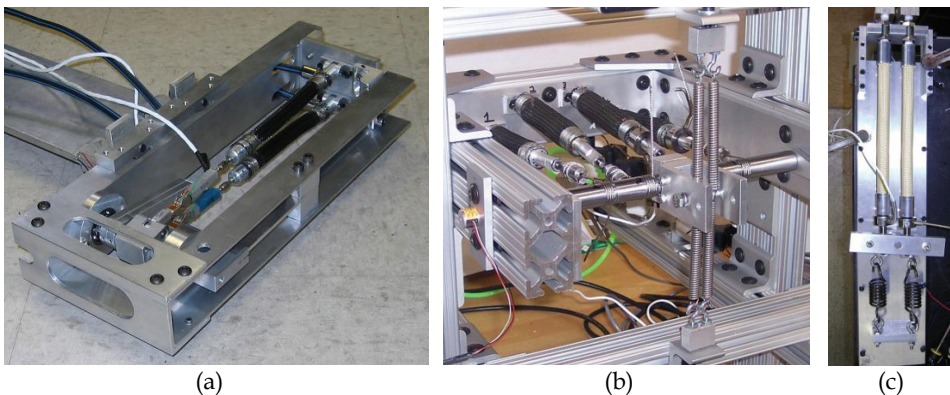


Fig. 5. Experimental setups for bench-top evaluations – (a) system 1; (b) system 2; (c) system 3

For each of the three test cases, the hinge rotation angle was measured with a Hall-effect angle sensor (Midori, series QPC). Two of the PAM actuators were instrumented with load cells (Honeywell) and the actuation pressure was measured with a pressure transducer (Omega, series PX209). Solenoid valves were used to direct the air flow into and out of the PAMs, as directed by a square wave voltage input for these open-loop experiments. For the two chordwise PAM configurations, the control valves used were SMC model VZ solenoids and for the spanwise PAM configuration, it was a Festo model MPYE valve with a much higher flow capacity. A National Instruments data acquisition system and laptop computer were used to run the experiments and to collect data. The test procedure included driving the control valves at various input frequencies and under different spring loads to measure the dynamic response of the PAM actuation systems in terms of flap deflection angle bandwidth.

3.2 Bench-top test results

Figure 6 shows the bench-top test results from the three cases as half peak-to-peak deflection values that were averaged over several actuation cycles. Here, Figure 6(a) shows data from system 1 for a range of pressures. It should be noted that the spring load indicated in the caption simulates air loads existing at a free-stream velocity of Mach 0.23, while the design

condition was only for Mach 0.1. The difference here was due to spring availability at the time of the test, so a more conservative loading condition (approximately four times the expected wind tunnel load) was tested on the bench-top. Given that the PAM actuation system was able to produce nearly ± 5 degrees of flap deflection over the tested frequency range of 30 Hz provided sufficient assurance that the system would meet, and most likely surpass, the ± 10 degree target in the wind tunnel. As expected from basic PAM operation, this figure also shows that increasing the pressure led to increased deflection capability. Figure 6(b) shows data from the Mach 0.3 spring load of the chordwise, double PAM pair actuators (system 2) at various pressures, showing a different characteristic than was shown for system 1. As can be seen, the quasi-static deflection output increases fairly linearly with actuation pressure, but there is a sharp roll-off in deflection performance at frequencies above 1 Hz that reduces the achievable deflection level at higher frequencies. Additionally, the measured deflection at high frequency appears to be independent of pressure. These response features indicate that air flow restrictions were present in the pneumatic supply system. This is a reasonable outcome when considering that the same pneumatic valves were used for systems 1 and 2, while the air volume required for operating system 2 was much larger than that for system 1. This was later improved upon in a revised bench-

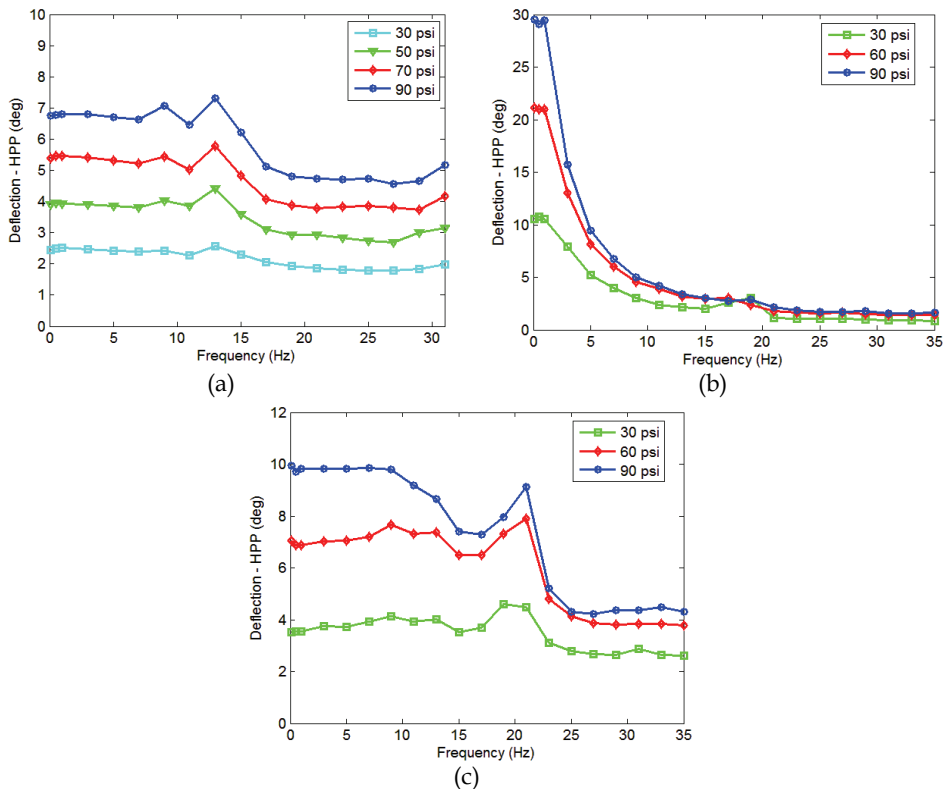


Fig. 6. Bench-top test results – (a) system 1 with Mach 0.23 spring load; (b) system 2 with Mach 0.3 spring load; (c) system 3 with Mach 0.56 spring load

top test, but the improved pneumatics for system 2 was not tested in a wind tunnel, so those results will not be presented here (Kothera et al., 2008). In continued scaling of the PAM actuation system, system 3 did incorporate improved pneumatic elements. Figure 6(c) shows experimental flap deflection measurements from a Mach 0.56 spring load at various pressures for system 3, where it can be seen that the deflection bandwidth was significantly increased over that seen from system 2, with ± 10 degrees now being produced up to nearly 10 Hz at 90 psi. Based on these results, it was concluded that systems 1 and 3 would meet the goal of at least ± 10 degrees of flap deflection in the dynamic response for their respective wind tunnel tests, but system 2 would likely fall short of the goal due to the flow rate restrictions in the pneumatic circuit. These tests also verified proper basic functionality of the actuation systems.

4. Wind tunnel testing

After successful bench-top evaluations, the trailing-edge flap actuation systems were placed in various wind tunnel test articles to assess their performance under actual aerodynamic loading conditions. This section will discuss the test article fabrication and experimental test results.

4.1 Wind tunnel test article development

The three PAM actuation systems were integrated into different test articles based on their originally specified performance conditions and measured performance from the bench-top evaluations. Systems 1 and 2 had the same geometry, as stated in Table 1, but different construction was used to better match the test conditions. That is, system 2 was designed with a stronger frame structure and skin than system 1. The frame for system 1 was constructed with 0.25-in aluminum and consisted of a spar running the span of the airfoil section (24-in), an airfoil-shaped end plate at both ends, and two intermediate support ribs that extended from the spar to the trailing-edge. The flap hinge was fabricated from a precision ground 0.25-in stainless steel rod, and the flap was able to rotate about the hinge with a bearing at each end. The skin was made with a wet lay-up process using two plies of pre-impregnated fibreglass, and formed the shape of the airfoil section with a Styrofoam mold. Additional reinforcement at the leading-edge was provided with a thin sandwich structure of fibreglass and foam, which formed a shell-like structure around the spar so that the solenoid valves and air tubing could be installed inside. The system 2 wind tunnel model had the same basic layout as the system 1 model, but it was made to be stronger since it was to be tested at Mach 0.3. That is, it had two airfoil-shaped end plates and two mid-span support ribs, all constructed of 0.5-in aluminum, and a steel spar. The entire skin was also fabricated as sections of sandwich structure composites with foam core inside 2-ply fibreglass. There was a separate leading-edge, or D-spar section, and aft panels that were fastened to the frame structure. As with system 1, system 2 also placed the solenoid control valves inside the D-spar cavity surrounded by the shell-like skin. Figure 7(a) shows the system 1 wind tunnel model installed in the test fixture between two acrylic vertical walls and positioned in front of the free-jet wind tunnel. Figure 7(b) shows the wind tunnel model for system 2, which was fixed at the floor of the Glenn L. Martin wind tunnel at the University of Maryland and cantilevered upward. There was also an elliptical top plate bolted to the top of the cantilevered model to promote more desirable air flow characteristics over the test section. The primary difference in appearance of these two models is that the system 1 model was left bare and the system 2 model was painted black. Note also that strips of aluminum tape were placed over the recessed fasteners.

The wind tunnel model for system 3 was fabricated with an entirely different approach than those for systems 1 and 2. In this case, instead of building the complete airfoil section from raw materials, the outboard section of a scrapped full-scale Bell 407 helicopter rotor blade was employed as the basis for the wind tunnel model. Since this rotor blade does not currently feature a trailing-edge flap, the blade was physically modified to accept a flap and the PAM actuation system. The spanwise PAM actuators and mechanism were mounted inside the D-spar of the blade and the aft section of the blade was removed. This section was first used to create a mold for the new trailing-edge flap so that the geometry of the blade could be matched exactly. Note that the production Bell 407 blade contains taper and twist, which would have otherwise been difficult to match in constructing the flap. Aluminum strips were bonded inside the remaining aft portion of the blade skin where the flap section had been removed in order to provide bearing surfaces and structural support to fasten the trailing-edge flap in place. The flap was supported at the inboard and outboard ends and at two intermediate locations. A hole was drilled in the aft wall of the spar and a slot was placed in the skin to attach a control rod from the mechanism inside the spar to a control horn on the trailing-edge flap. These parts are on the opposite side of blade section in Figure 7(c), so they are not visible in the photograph; the control rod was located at the inboard edge of the flap, or near the floor in the figure. Recall that system 3 was the only system for which a component of the PAM actuation system violated the baseline airfoil profile. This was due largely to the smaller size of the airfoil section and the higher wind loading condition. Also note that the tip of the cantilevered blade section was laterally restrained with a cable to limit side-to-side motion of the blade during flap actuation.

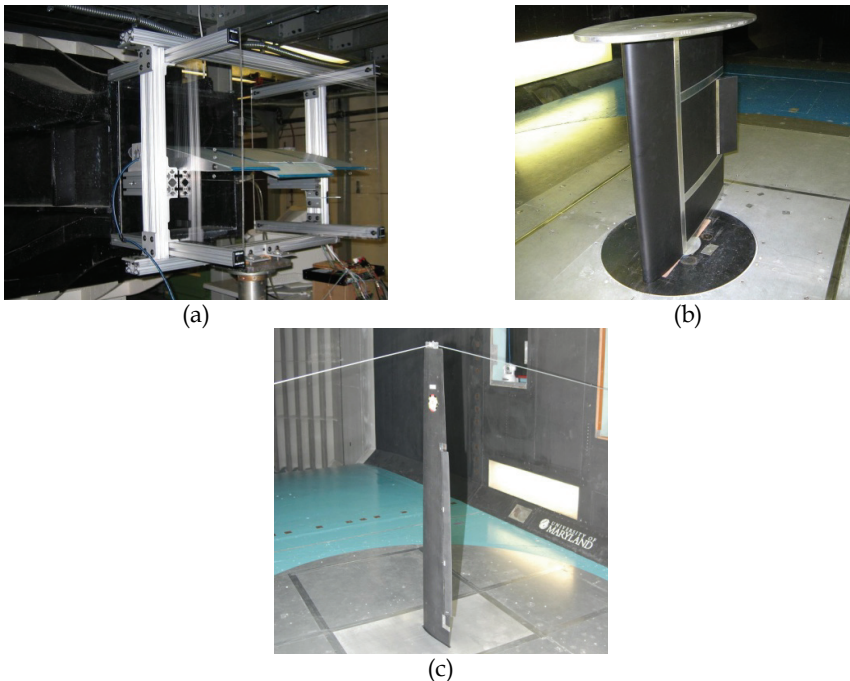


Fig. 7. Wind tunnel test articles - (a) system 1, free-jet; (b) system 2, closed-circuit; (c) system 3, closed-circuit

4.2 Wind tunnel test results

Test results in the form of averaged, half peak-to-peak deflection are displayed in Figure 8, following the same layout as the previous figures. Shown in each case are the measured results from the previously specified wind tunnel test conditions, with the effect of varying actuation pressure also displayed for systems 1 and 3. Reaching a maximum speed of Mach 0.1, Figure 8(a) shows the open-loop dynamic response of system 1 at various actuation frequencies and pressures. As was inferred from the bench-top test, this PAM actuation system was able to far exceed the original goal of ± 10 degrees at high frequency. At only 30 psi operating pressure in the PAMs, this system was able to produce ± 10 degrees beyond 20 Hz, and operating the PAM actuators with 90 psi led to ± 20 degrees of flap deflection being produced up to nearly 25 Hz. There is also a resonance phenomenon apparent in this data set, which can be seen to increase in frequency with pressure. This changing resonance frequency is attributed to the changing stiffness of the PAM actuators as their operational pressure changes. Figure 8(b) shows the experimental flap deflections from system 2 that were measured at 90 psi in the PAM actuators and at two different angles-of-attack, though there is little noticeable difference in the dynamic response of the system at the two angles-of-attack.

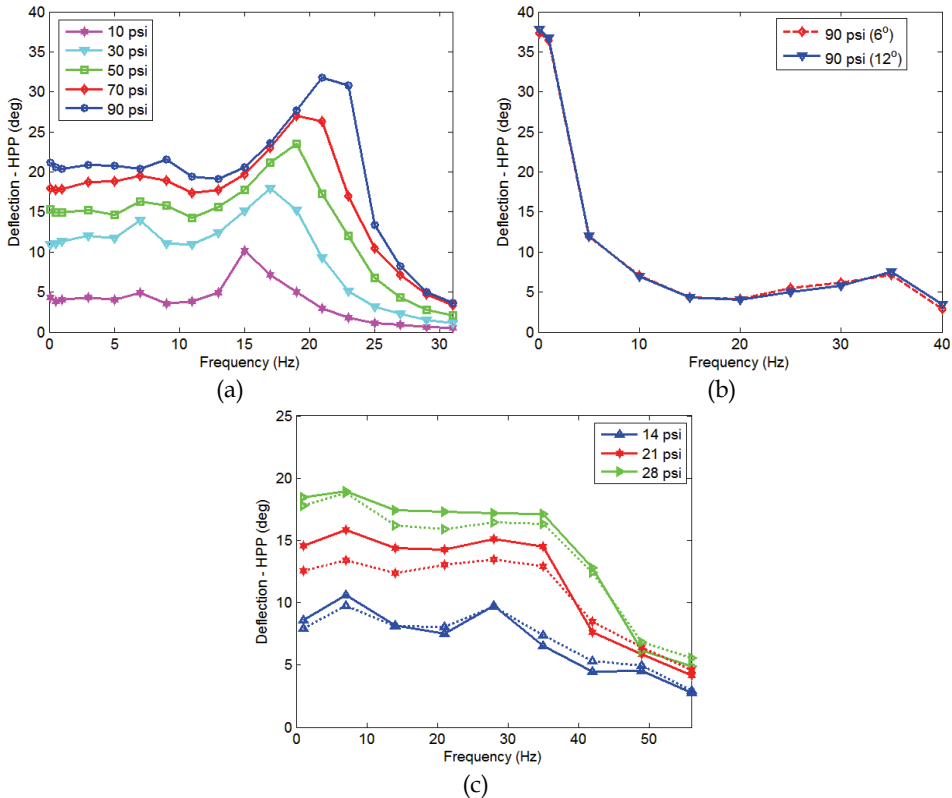


Fig. 8. Wind tunnel test results – (a) single PAM pair, chordwise at Mach 0.1; (b) double PAM pair, chordwise at Mach 0.3; (c) single PAM pair, spanwise at Mach 0.3

As was expected from the bench-top test results, this system again illustrates a rapid drop off in achievable flap deflection as the actuation frequency increases. Recall that this was due to flow limitations in the pneumatic components. The ability to produce almost ± 40 degrees quasi-statically at Mach 0.3, however, is a promising result for the technology, especially when the dynamic response shown can be viewed as potentially a worst case situation achieving ± 4 degrees of flap deflection up to 40 Hz.

Figure 8(c) shows the wind tunnel results for system 3 at Mach 0.3. Recall that this is reduced from the bench-top test condition (Mach 0.56), but was the maximum possible speed of the wind tunnel used for testing. There are also two lines for each of the noted actuation pressure levels. The solid line represents the flap deflection measured at the inboard edge of the flap and the dotted line represents the deflection at the outboard edge of the flap. Since there is some difference between the two ends of the flap, this implies that there was some wash-out present in the model. This could be reduced in the future by increasing the torsional stiffness of the trailing-edge flap or attaching the actuation mechanism to a more central location on the flap instead of at the inboard end. Regardless of this effect, the measured actuation performance met and exceeded the goal of ± 10 degrees dynamically. Nearly 10 degrees can be maintained for up to 30 Hz at only 14 psi PAM operating pressure, whereas nearly 18 degrees can be maintained for up to 35 Hz when driving the PAM actuators with 28 psi. Recall that this test case is a reduced load from the expected condition, so the PAM input pressures had to be reduced, as well. Based on all of these results, it can be stated that PAM actuation systems have clearly demonstrated their high performance capabilities for aerospace applications.

5. Conclusion

This research has developed and tested a series of innovative trailing-edge flap actuation systems that exploit antagonistic configurations of Pneumatic Artificial Muscles (PAMs) to generate bi-directional flap deflections. The systems were designed and built for experimental evaluation on the bench-top under simulated aerodynamic loadings with spring mechanisms and in the wind tunnel under actual aerodynamic conditions up to the maximum speed (Mach 0.3) of the Glenn L. Martin wind tunnel at the University of Maryland. Results showed that the flap deflection range produced was attractive to various flight control regimes, including flight control, vibration control, and even noise control. The key conclusion of this work is that PAM actuation systems have demonstrated the ability to dynamically control large flap deflections over a wide bandwidth in these varying control regimes and offer an attractive solution to aerodynamic control applications.

6. Acknowledgments

This research and development was conducted under several SBIR projects sponsored by the Army. Specifically contract number W911W6-05-C-0007 (technical monitors Drs. Tin-Chee Wong and John D. Berry), contract number W911W6-06-C-0033 (technical monitor Dr. Mark V. Fulton), and contract number W911W6-07-C-0053 (technical monitor Dr. Mark V. Fulton). The authors greatly appreciate this support. The authors would also like to acknowledge the effort and contributions made by Prof. Jayant Sirohi, Mr. Benjamin K.S. Woods, Mr. Edward A. Bubert, Mr. Robert D. Vocke, and Mr. Shane M. Boyer.

7. References

- Abbott, I.H. and von Doenhoff, A.E. (1959). *Theory of Wing Sections*, Dover Publications, New York.
- Arnold, U.T.P. and Strecker, G. (2002). Certification, ground and flight testing of an experimental IBC system for the CH-53G helicopter, *Proceedings of American Helicopter Society 58th Annual Forum*, ISBN, Montreal, Quebec, June 2002.
- Bubert, E.A., Woods, B.K.S., Sirohi, J., Kothera, C.S., and Wereley, N.M. (2007). Whirl Testing of Pneumatic Artificial Muscle Systems for Helicopter Rotor Applications, *Proceedings of ASME International Design Engineering Technical Conference*, Las Vegas, NV, September 2007.
- Bubert, E.A., Woods, B.K.S., Lee, K., Kothera, C.S., and Wereley, N.M. (2010). Design and Fabrication of a Passive 1D Morphing Aircraft Skin, *Journal of Intelligent Material Systems and Structures*, Vol. 21 (November 2010) pp. 1699-1717.
- Chen, P.C. and Chopra, I. (1997). Wind Tunnel Test of a Smart Rotor Model With Individual Blade Twist Control, *Journal of Intelligent Material Systems and Structures*, Vol. 8 (May 1997) pp. 414-425.
- Chen, P.C., Baeder, J.D., Evans, R., and Niemczuk, J. (2001). Blade-Vortex Noise Reduction with Active Twist Smart Rotor Technology, *Journal of Smart Materials and Structures*, Vol. 10 (January 2001) pp. 77 - 83.
- Chopra, I. (2000). Status of application of smart structures technology to rotorcraft systems, *Journal of the American Helicopter Society*, Vol. 45 (October 2000) pp. 228-252.
- Daerden, F. and Lefeber, D. (2002). Pneumatic Artificial Muscles: actuators for robotics and automation, *European Journal of Mechanical and Environmental Engineering*, Vol. 47 (January 2001) pp. 10 - 21.
- Dieterich, O., Enenkl, B., and Roth, D. (2006). Trailing Edge Flaps for Active Rotor Control Aeroelastic Characteristics of the ADASYS Rotor System," *Proceedings of the American Helicopter Society Annual Forum*, Phoenix, AZ, May 2006.
- Eastman, J.N. and Pinkerton, R.M. (1930). Pressure Distribution Over a Symmetrical Airfoil Section with Trailing Edge Flap, In: *NACA Technical Report No. 360*, NACA Digital Library.
- Etkin, B. (1982). *Dynamics of Flight*, 2nd ed., Wiley Publications, New York.
- Flanagan, J.S., Strutzenberg, R.C., Myers, R.B., and Rodrian, J.E. (2007). Development and Flight Testing of a Morphing Aircraft, the NextGen MFX-1, *Proceedings of AIAA Structures, Structural Dynamics and Materials Conference*, Honolulu, HI, April 2007.
- Fulton, M.V. (2000). Design of the Active Elevon Rotor for Low Vibration, *Proceedings of American Helicopter Society Aeromechanics Specialists Meeting*, Atlanta, GA, November 2000.
- Fulton, M.V. (2005). Aeromechanics of the Active Elevon Rotor, *Proceedings of American Helicopter Society 61st Annual Forum*, Grapevine, TX, June 2005.
- Gaylord, R. (1958). Fluid actuated motor system and stroking device, United States Patent No. 2,844,126.
- Hall, S.R. and Wereley, N.M. (1993). Performance of higher harmonic control algorithms for helicopter vibration reduction, *AIAA Journal of Guidance, Control and Dynamics*, Vol. 16 (Jul-Aug 1993) pp. 794-797.
- Konstanzer, P., Grohmann, B., and Kroplin, B. (2001). Decentralized Vibration Control and Coupled Aeroservoelastic Simulation of Helicopter Rotor Blades with adaptive Airfoils, *Journal of Intelligent Material Systems and Structures*, Vol. 12 (April 2001) pp. 209 - 214.

- Kothera, C.S., Wereley, N.M., Woods, B.K.S., and Bubert, E.A. (2008). Wind Tunnel Testing of a Trailing-Edge Flap Actuated by Pneumatic Artificial Muscles, *Proceedings of American Helicopter Society 64th Annual Forum*, Montreal, Quebec, April 2008.
- Kothera, C.S., Woods, B.K.S., Sirohi, J., Wereley, N.M., and Chen, P.C. (2010). Fluid-driven artificial muscles as mechanisms for controlled actuation, United States Patent No. 7,837,144.
- Lorber, P., Park, C., Polak, D., O'Neill, J., and Welsh, W.A. (2001). Active rotor experiments at Mach scale using root pitch IBC, *Proceedings of American Helicopter Society 57th Annual Forum*, ISBN, Washington DC, May 2001.
- Medrano-Cerda, G.A., Bowler, C.J., and Caldwell, D.G. (1995). Adaptive position control of antagonistic pneumatic muscle actuators, *Proceedings of IEEE Intelligent Robots and Systems Conference*, Vol. 1 (1995) pp. 378 - 383.
- Nissly, A., Anusonti-Inthra, P., Gandhi, F., and Frecker, M. (2005). Design Optimization of a Controllable Camber Rotor Airfoil, *Proceedings of American Helicopter Society 61st Annual Forum*, Grapevine, TX, June 2005.
- Olympio, K.R. and Gandhi, F. (2010). Flexible Skins for Morphing Aircraft Using Cellular Honeycomb Cores, *Journal of Intelligent Material Systems and Structures*, Vol. 21 (November 2010) pp. 1719-1735.
- Roth, D., Enenkl, B., and Dieterich, O. (2006). Active Rotor Control by Flaps for Vibration Reduction - Full scale demonstrator and first flight test results, *Proceedings of the European Rotorcraft Forum*, Maastricht, Netherlands, September 2006.
- Schulte, H.F. (1961). The characteristics of the McKibben artificial muscle, In: *The Application of External Power in Prosthetics and Orthotics*, Publication 874, National Academy of Sciences - National Research Council, Washington DC, App. H, pp. 94 - 115.
- Shin, S.J., Cesnik, C.E.S., and Hall, S.R. (2005). Closed-loop control test of the NASA/Army/MIT active twist rotor for vibration reduction, *Journal of the American Helicopter Society*, Vol. 50 (April 2005) pp. 178-194.
- Straub, F.K., Ngo, H.T., Anand, V., and Domzalski, D.B. (2001). Development of a piezoelectric actuator for trailing edge flap control of full scale rotor blades, *Smart Materials and Structures*, Vol. 10 (2001) pp. 25 - 34.
- Straub, F.K., Kenedy, D.K., Stemple, A.D., Anand, V.R., and Birchette, T.S. (2004). Development and whirl tower test of the SMART active flap rotor, *Proceedings of SPIE Symposium on Smart Structures and Materials*, San Diego, CA, March 2004.
- Straub, F.K., Anand, V.R., Birchette, T.S., and Lau, B.H. (2009). Wind Tunnel Test of the SMART Active Flap Rotor, *Proceedings of the American Helicopter Society Annual Forum*, Grapevine, TX, May 2009.
- Tondu, B., Boitier, V., and Lopez, P. (1994). Naturally compliant robot-arms actuated by McKibben artificial muscles, *Proceedings of IEEE Conference on Systems, Man, and Cybernetics*, Vol. 3 (October 1994) pp. 2635 - 2640.
- Woods, B.K.S., Bubert, E.A., Kothera, C.S., Sirohi, J., and Wereley, N.M. (2007). Experimental Testing of Pneumatic Artificial Muscles for Trailing-Edge Flap Actuation, *Proceedings of AIAA Structures, Structural Dynamics and Materials Conference*, Waikiki, HI, April 2007.
- Woods, B.K.S., Kothera, C.S., and Wereley, N.M. (2010a). Whirl Testing of a Pneumatic Artificial Muscle Actuation System for a Full-Scale Active Rotor, *Proceedings of American Helicopter Society 68th Annual Forum*, Phoenix, AZ, May 2010.
- Woods, B.K.S., Wereley, N.M., and Kothera, C.S. (2010b). Wind Tunnel Test of a Helicopter Rotor Trailing Edge Flap Actuated via Pneumatic Artificial Muscles, *Proceeding of ASME Conference on Smart Materials, Adaptive Structures and Intelligent Systems*, Philadelphia, PA, September 2010.

Experimental Study of Flow-Induced Vibrations and Scattering of Roof Tiles by Wind Tunnel Testing

Satoru Okamoto
Shimane University
Japan

1. Introduction

The tremendous destruction caused by recent typhoons in Japan has caused a substantial upsurge in interest in the subject of global warming among news media and the wider public. There are concerns that global climate change may have played a significant role in these events. Some believe that global warming is responsible for an increase in the frequency of destructive natural events. Typhoons cause the destruction of tiles on the rooftops of Japanese residences. The wind load on a roofing element is created by the difference between the external and internal pressures. The net wind load is, in general, determined by the building flow field, wind gustiness, and the element flow field (Peterka et al, 1997; Cermak, 1998). Although these parameters directly influence the external pressure distribution on a roofing element, the development of internal pressure, which indirectly depends on these parameters, is governed by a dynamic response that varies according to different roofing elements. The pressure distribution on an external roof surface and internal pressure distribution have been determined in numerous studies (Hazelwood, 1980; Ginger, 2001). Element wind loading may differ significantly from the load derived from the external pressure distribution. Internal pressure is governed by the wind permeability of the surface, which is determined by openings, such as gaps between tiles or venting devices, and by the equilibrating resistance through and underneath a wind permeable surface (Kramer et al, 1979).



Fig. 1. Japanese residence and roof tiles

Flow-induced vibration of roof tiles usually appears just before they are scattered. The flow-induced vibration (aeroelastic instability) of structures is an important phenomenon for the following two reasons: (1) strong lateral self-excited oscillations can develop at a certain wind velocity (onset velocity) as a result of the lateral aerodynamic force component and (2) these vibrations have a tendency to affect the behavior of the structure prior to the onset velocity because they produce negative aerodynamic damping that can considerably reduce the total damping available to the structure (Naudascher et al., 1993). However, the flow-induced vibration of roof tiles prior to scattering has been given very little attention. This study investigates the nature and source of the vibrating and scattering behavior of the roof tiles in order to provide better insight into this mechanism. This paper presents the first results of studies on the wind-inducing mechanism in roof tiles, which are widely used for roofing Japanese wooden dwellings (Fig. 1).

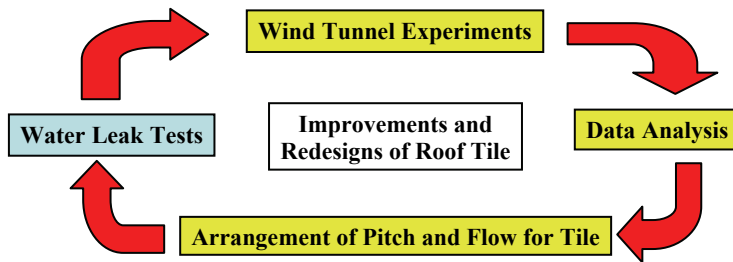


Fig. 2. Outline of the research

Using wind tunnel tests, an experimental study was conducted to explain the behavior of roof tile vibration and the primary factors that affect their scattering. The results indicate that the vibration mechanism behaves in a manner that is consistent with that of a self-excited system, and the surface flow creates reasonable up-lifting moments only when the wind direction is roughly perpendicular to that of the eaves (Fig. 2).

Nomenclature

- θ pitch angle (degree)
- ϕ flow angle (degree)
- U upstream flow velocity (m/s)
- X streamwise coordinate
- Y transverse coordinate
- Z coordinate perpendicular to the surface of a roof tile

2. Test facility and analysis procedure

Fig. 3 illustrates the general layout of the apparatus used in this experiment. The experiments were conducted in an open-circuit wind tunnel that was driven by an axial flow fan. The nozzle of the wind tunnel had a 500 mm \times 1,300 mm cross section. The maximum velocity of flow from the nozzle was approximately 50.0 m/s. The representative wind velocity was measured by a hot-wire anemometer and a linearizer on the exit nozzle of the wind tunnel. Approximately 10.0% of the flow's streamwise turbulence intensity was

generated by the grids. The spatial characteristics of air jet were checked for uniformity in wind speed and turbulence to ensure that all tiles were exposed to a near uniform air flow. The turbulence intensity of the flow condition is of the same order as the turbulence intensity experienced in practice.

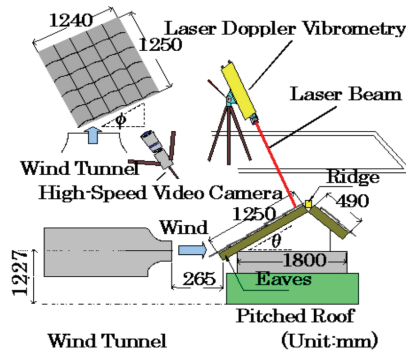
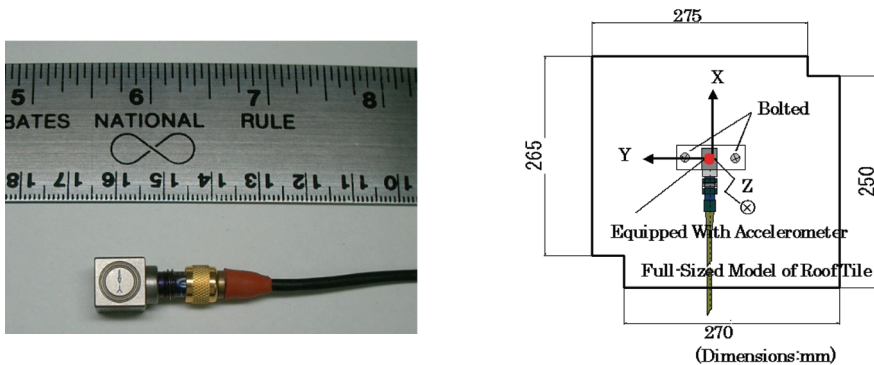


Fig. 3. Experimental apparatus

25 roof tiles were set up in 5 rows \times 5 columns on a pitched roof in the downstream flow of a wind tunnel (Fig. 3). The roof tiles were tested by the air flow, which barely covered the entire exposed area of the tiles. They were made of clay, and each weighed approximately 2.8 kg. The tiled pitched roof was fitted similar to a real roof arrangement with a plenum underneath the tiles, which acts as a roof cavity. This plenum was sealed with a clay pad. The internal pressure in this plenum was monitored and regulated by a pressure transducer placed underneath the tiles. The vibrations of the roof tiles were measured by a laser Doppler vibrometer (LDV, OMETRON VS1000) and an accelerometer (ONO SOKKI NP-3560, Fig. 4 (a)), and the normal natural frequencies of the roof tiles were analyzed using an impulse force hammer test. The vibration velocity could be measured up to 1,000 mm/s by a 1 mW LDV, and the range of the vibrational frequency was from 0 to 50 kHz. One roof tile was equipped with an accelerometer (Fig. 4 (b)). The accelerometer was used to measure the dynamic behavior of the tiles in three directions, X-, Y-, and Z under a no-flow condition,



(a) Accelerometer

b) Roof tile equipped with accelerometer

Fig. 4. Accelerometer used in the experiments

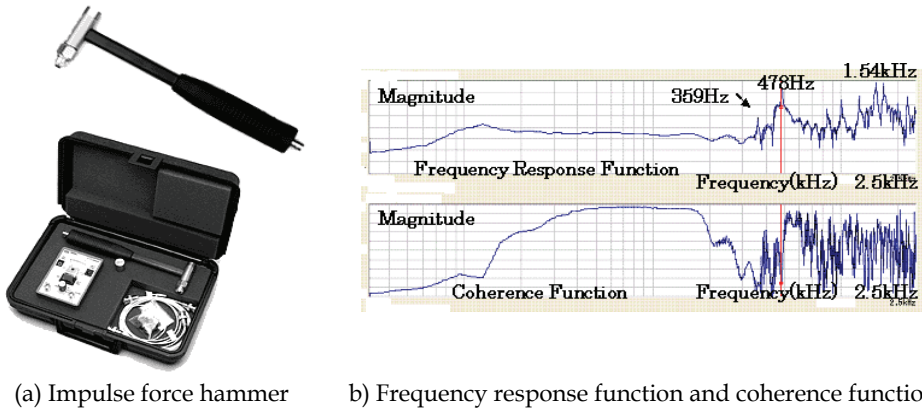


Fig. 5. Frequency response function and coherence function of a roof tile generated by an impulse force hammer test

and weighed approximately 5.0 g. The experimental measurement of the vibration frequencies for tiles was performed with the accelerometer. However, the vibration frequencies identified by the LDV were limited to small-amplitude modes. In this study, the accelerometer and LDV were used to determine the resonant frequencies of roof tiles that were and were not bolted to the roof bed.

An impact hammer with a force transducer was used to excite the tiles under no-flow conditions (Fig. 5 (a)). Two signal conditioners were used to provide power to the accelerometer and the force transducer, whose spectral analyses were performed using a fast Fourier transform (FFT) spectrum analyzer (ONO SOKKI DS-2100 4CH). The sampling frequency was 5,120 Hz over a frequency range of 0 - 2.5 kHz; 1,024 data points were sampled per spectrum. Unless otherwise stated, 64 spectra were averaged for each measurement. The frequency resolution of the spectra was 5 Hz. In order to analyze acceleration in a direction perpendicular to the surface of a roof tile, the time taken by the acceleration signal was recorded using the FFT analyzer. Two accelerometers were used simultaneously. Roof tiles that showed significant vibrations at any velocity, found from a series of experiments using accelerometers, were attached to two neighboring roof tiles on a model roof.

The dynamic instability of the structure under excitation was also visually investigated. Large amplitude vibrations and the scattering of roof tiles were observed by a high-speed video camera (PHOTRON FASTCAM-PCI 2KC). The images were acquired at 2,000- frames per second, at a resolution of 512 pixels \times 480 pixels per full frame. A hot-wire anemometer and a linearizer were used to measure the turbulence intensity of surface flow over the roof tiles.

3. Results and discussion

3.1 Impulse force hammer test for roof tiles

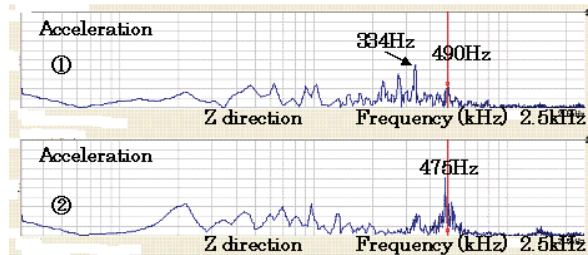
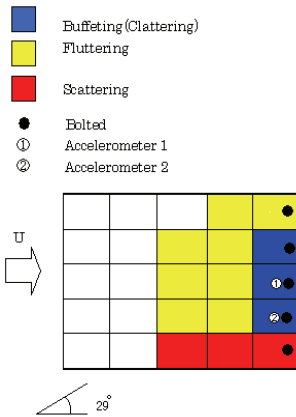
Fig. 5 (b) shows the frequency response function curve and coherence function curve of roof tiles measured using an impact hammer with a force transducer. One of the resonant frequencies obtained by the accelerometer was 478 Hz. As stated in the next section, the measured frequencies obtained using the wind tunnel test are nearly consistent with the resonant frequencies obtained by the excitation analysis of the impulse force hammer test.

The value of the input excitation level is set to be approximately constant for the excitation analysis. However, the flow-induced excitation level is amplified and a higher level should be provided to obtain vibration measurements. On the other hand, the variation in the measured values of resonant frequencies for the accelerometer measurement and excitation analysis may be attributed to the added weight of the accelerometer in this experimental technique. In order to eliminate the effect of the added weight of the accelerometer on the resonant frequencies of the roof tile, the corresponding frequency response curve of this roof tile was obtained using the LDV. The peak values of this frequency response curve were compared with those obtained using the accelerometer method. It was found that the results of resonant frequencies measured using LDV and those using the accelerometer agreed satisfactorily.

3.2 Acceleration measurements of roof tile

In the measurement and analysis of roof tile vibration and its acceleration, the pitch of the roof θ was set at 19 degrees, 24 degrees, and 29 degrees and the flow angle ϕ was set at 0 degrees. The wind velocity was gradually increased from 0 to 50.0 m/s or until scattering of the tiles occurred. The signals from the accelerometers were recorded to be analyzed later using a personal computer.

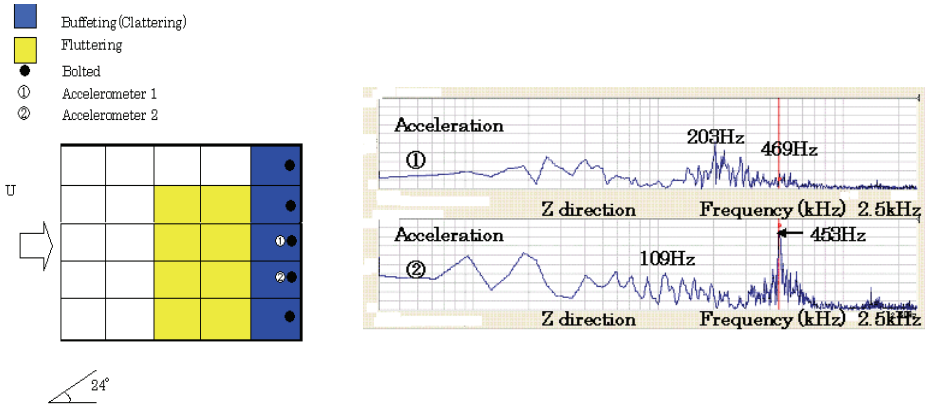
The slope angle of the roof was changed, and the effects of fluttering in the last stage of roof tile scattering were examined (Figs. 6-8). The small-amplitude vibration of the model roof tiles appeared in a low-velocity flow at the maximum pitch angle of 29 degrees, while the model roof tiles showed fluttering when the wind velocity reached approximately 38 m/s. They were more buffeted at the pitch angle of 24 degrees than at the pitch angle of 29 degrees, and then fluttered when the wind velocity reached approximately 40 m/s. The model roof tiles did not flutter at the minimum pitch angle of 19 degrees, and they were buffeted at a higher wind velocity than that at other pitch angles. They did not flutter at pitch angles of 24 and 29 degrees because of the weight of the neighboring roof tiles and bolts. The fluttering of the model roof tiles appeared with relatively large-amplitude vibrations, and it was regarded as fluttering when the roof tile was completely lifted from the roofing board and the board was exposed.



(a) Vibration of roof tiles

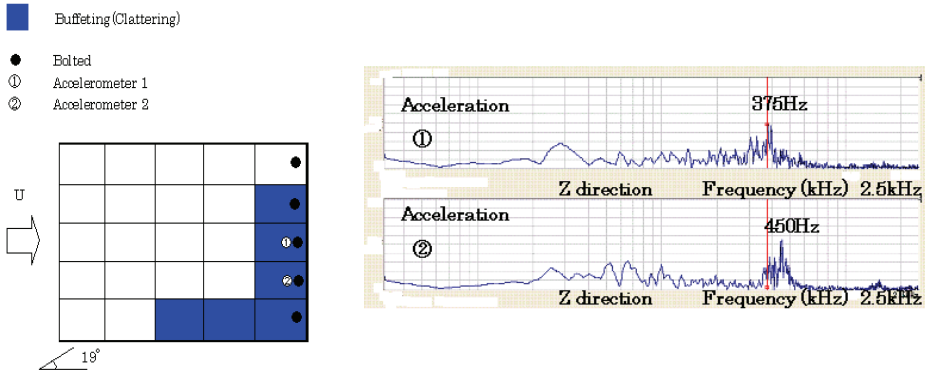
(b) Vibrational acceleration power spectrum for roof tiles

Fig. 6. Effect of slope angle of roof on vibration of roof tiles at $\theta = 29$ degrees, $U = 39.0$ m/s



(a) Vibration of roof tiles (b) Vibrational acceleration power spectrum for roof tiles

Fig. 7. Effect of slope angle of roof on vibration of roof tiles at $\theta = 24$ degrees, $U = 38.5$ m/s



(a) Vibration of roof tiles (b) Vibrational acceleration power spectrum for roof tiles

Fig. 8. Effect of slope angle of roof on vibration of roof tiles at $\theta = 19$ degrees, $U = 39.9$ m/s



Fig. 9. Observation of the flow on the surface of the roof tile by the oil film method

The occurrence of fluttering was considered as one of the last stages of roof tile scattering. Fluttering did not occur at the lower pitch angle and, as a result, the model roof tiles resisted vibration and scattering at even higher velocities, whereas fluttering occurred at a higher pitch angle because the model roof tiles were often buffeted and scattered by lower critical velocities. In addition, the oil-film method was used to observe the flow pattern on the surface of the every tile in the model roof (Fig. 9). Separation regions appeared over the surface of the roof tiles as the flow angle was gradually increased. The wind flow was along the surface of the roof at a lower pitch angle, whereas the flow was split directly by the surface and the edge of the roof tile at a higher pitch angle. The wind flow was toward the edge of the roof, and it was found that the flow became very turbulent locally over the edge and formed the separation regions. The appearance of the separation regions was considered to indicate a significant fall in the external pressure and a rise in the internal pressure, causing the fluttering of the roof tiles. The clattering of the model roof tiles was recognized in the Y-axis direction at a pitch angle of 29 degrees. It was found that this may be caused by the decrease of the critical velocity, which lifted up the tiles and caused them to flutter.

Figs. 6-8 show the results for several pitch angles. The largest number of roof tiles were buffeted and fluttered at the maximum pitch angle of 29 degrees (Fig. 6 (a)), resulting in three roof tiles being scattered. The roof tiles were not scattered at a pitch angle of 24 degrees (Fig. 7 (a)), whereas they were both buffeted and scattered at a pitch angle of 29 degrees. In this case, the roof tiles attached with the accelerometers and the eight neighboring roof tiles fluttered. At the minimum pitch angle of 19 degrees (Fig. 8 (a)), the roof tiles did not flutter even at the maximum velocity of 40 m/s, but a few roof tiles were buffeted.

Similarly, the signals from the accelerometers revealed fluttering at pitch angles of 24 and 29 degrees. The results obtained by the FFT analysis of the accelerometer signals at pitch angles of 24 and 29 degrees are shown in Figs. 7 (b) and 6 (b), respectively. The small-amplitude vibrations were recognized using accelerometers 1 and 2 at a low velocity at these pitch angles. However, a 50 m/s² vibration was recognized momentarily when the wind velocity was increased. The small-amplitude vibrations appeared at a low velocity, but gradually increased at a higher velocity (Peterka et al., 1997; Cermak, 1998). Moreover, acceleration and amplitude of the vibrations are related to the critical velocity at which fluttering occurs for a constant pitch angle of the roof. At a pitch angle of 24 degrees, the values of acceleration and amplitude increased when the wind velocity reached 40 m/s (Fig. 7 (b)). The acceleration and amplitude observed at a relatively high velocity for a pitch angle of 24 degrees also appeared at a low velocity for a pitch angle of 29 degrees (Fig. 6 (b)).

The maximum acceleration value prior to fluttering was found at pitch angles of 24 and 29 degrees. Moreover, it was found that the acceleration decreased when the roof tiles fluttered at both pitch angles. This was found to be caused by the balancing of internal pressure in the space between the attic side and the roofing board by the external pressure of the flow over the roof tiles. On the other hand, it was occasionally observed that the neighboring roof tiles touched each other and unexpected acceleration signals were found because of contact between neighboring roof tiles during vibration. The effects of the roof's pitch angle on their scattering were recognized by analyzing the acceleration signals.

In a series of wind tunnel tests, the pitch angles of the roof were changed and two accelerometers were attached to neighboring roof tiles in order to detect and analyze acceleration signals. Fig. 10 shows an example of the acceleration signals that were frequently found whenever small-amplitude vibrations occurred. It shows the acceleration

signals and the behavior of the 25 model roof tiles at a pitch angle of 24 degrees and wind flow of 40 m/s. In this experiment, it was also recognized that the tiles locally arranged at the back and right side of the roof were often buffeted and scattered by strong winds. In a typical construction method, tiles are piled up and laid on the upper and lower side of a roof by their own weight. Therefore, the roof tiles locally arranged at the back and right side of the roof are held by the relatively lighter weight of the neighboring roof tiles. The wave-forms shown for case A in Fig. 10 (a) indicate that the signals are out of synchronization by a half cycle from both accelerometers. The wave-forms shown for case B in Fig. 10 (b) indicate the nearly synchronized signals from both accelerometers. Fig.10 shows the time history of the acceleration signals caused by the wind effect. These results show that it was found that the accelerations and time histories of the two roof tiles differ from each other. The forces affected both roof tiles simultaneously. On the other hand, even when a force did not act directly on a roof tile, it affected the other roof tile. In this case, the roof tile equipped with accelerometer ① was held by the roof tile equipped with accelerometer ② and the force of the roof tile equipped with accelerometer ② was added, although the force of the roof tile equipped with accelerometer ① did not act directly on it. The force of the tile equipped with accelerometer ① was added to the roof tile equipped with accelerometer ② although the force of the roof tile equipped with accelerometer ② did not act directly on it (case A). It was observed during a series of experiments that the roof tiles were buffeted almost simultaneously when vibration occurred (case B).

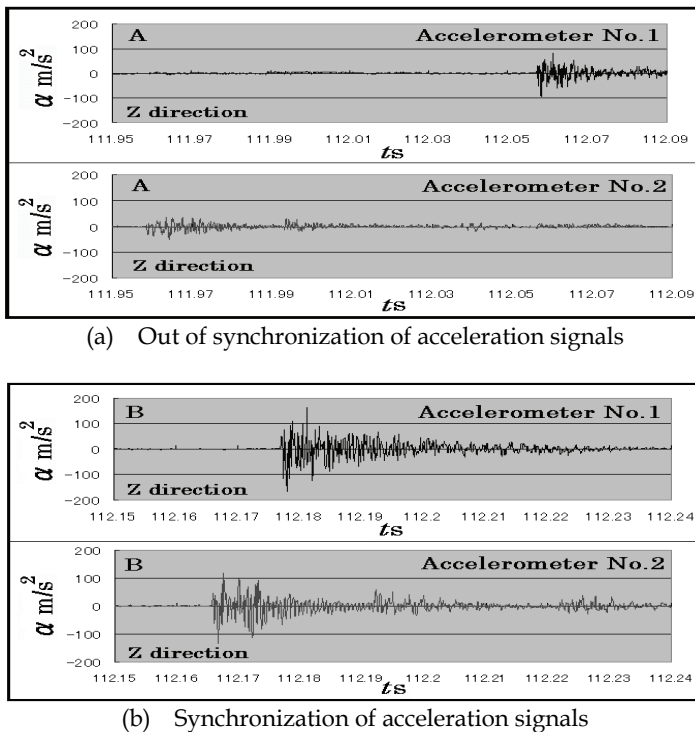


Fig. 10. Acceleration signals from accelerometers 1 and 2 at $\theta = 24$ degrees, $U = 40.0$ m/s

These results suggest that the roof tile held by the other roof tile was buffeted and then produced the reaction force on the neighboring roof tile. This behavior may be same as the "wave motion of roof tiles" phenomenon described by Ginger (2001), which is often reported to cause construction damage.

Hazelwood (1980b) described the lifting mechanism of a tile by a moment turning the tile upward around the pivoting point on the batten. The moment consists of a lifting force and two force couples caused by the external and internal pressure distributions, respectively. Fig. 11, which shows snapshots of a high-speed video camera picture, demonstrates this lifting mechanism for wind direction perpendicular to the eave. For a local flow direction perpendicular to the ridge, the internal pressure in the space between the tiles and underlay may become positive because of stagnation. As a result, the net wind load increases because of the sealing effect of the underlay. However, pressure equilibration in the gable roof is prevented, leading to a much lower net wind load for the leeward roof tiles. Aerodynamically favorable tiles should have a shape that prevents stagnation at the overlaps. The permeability at the overlapping gaps parallel to the ridge should be small and the permeability at the interlocking gaps perpendicular to the ridge, where suction occurs due to the element flow field, should be high (Hazelwood, 1980a).

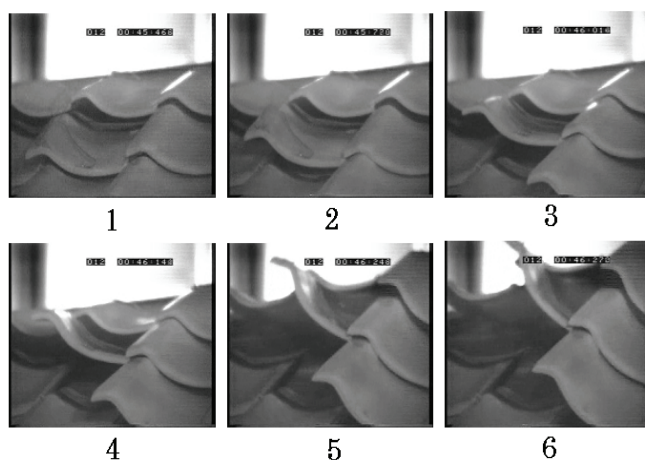
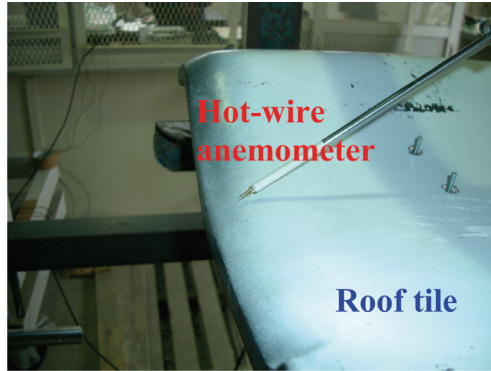


Fig. 11. Lifting up of roof tiles due to wind action as recorded by a high-speed video camera at $U = 40.0$ m/s

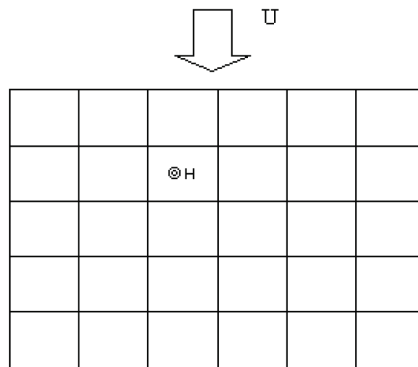
3.3 Transverse vibration of roof tiles

Fig. 12 shows an example of the typical turbulence spectrum obtained by the hot-wire anemometer for $\theta = 0$ degrees, $\phi = 90$ degrees, and $U = 40$ m/s. With a turbulence level of surface flow close to the roof tiles, the tiles exhibited only the typical turbulence-buffeting response within the intermediate ranges of the angle of incidence. The Reynolds number during the experiment was so high that the edge separation was turbulent. The sources of vibration are the front and side edge vortices (Fig. 13). The vibration amplitudes increased progressively with increasing velocity, which indicates a typical buffeting response.

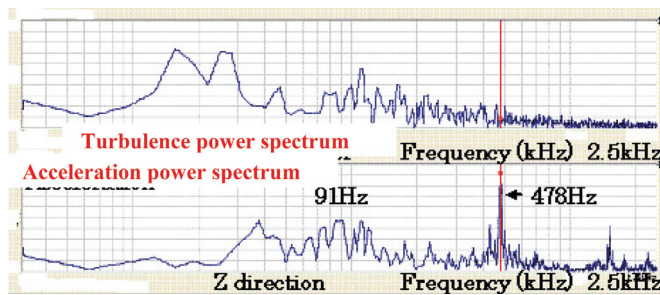


(a) Hot-wire anemometer and roof tile

⊙ Accelerometer
 H Hot wire anemometer



(b) Positions of accelerometer and hot-wire anemometer



(c) Vibrational acceleration and turbulence power spectrum.

Fig. 12. Vibrational acceleration and turbulence power spectrum of roof tiles for $\theta = 0$ degrees, $\phi = 90$ degrees, and $U = 40.0$ m/s

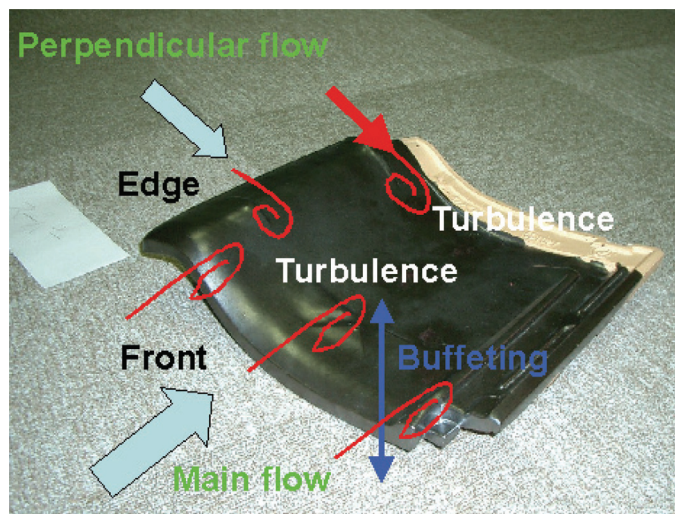


Fig. 13. Transverse vibration of roof tile

The local flow due to the outer shape of a surface element is of importance if the element is located in an area with attached flow, such as on the windward surface of a pitched roof. The gaps between the tiles may be exposed to local stagnation and/or suction depending on the shape of the tiles. If suction prevails, the internal pressure is decreased and the opposite takes place for predominating stagnation. For $\theta = 30$ degrees, a front edge vortex with its axis parallel to the ridge is formed, causing significantly higher negative pressure coefficients (Ginger, 2001). It is observed by the surface oil-flow visualization method that reattachment takes place upstream of the ridge and the flow is completely separated at the leeward roof area. If the roof pitch is increased, the vortex on the windward side decreases in size and reattachment takes place much closer to the eave. In the region of flow bifurcation, the pressure coefficient becomes positive (Peterka et al., 1997).

However, if the external pressure distribution is changed because of the shape of the element, the internal pressure can be affected significantly. In particular, for the local flow direction perpendicular to the ridge of a tiled roof, the flow is stagnated at the overlaps of the tiles. The stagnation pressure increases because of the step formed by overlapping tiles and leads to an increase in the internal pressure if the permeability of the overlap gaps is sufficient. This value depends on the shape of the front and side edges of the tile, i.e., square or round, and the level of free-stream turbulence; the larger the value of free-stream turbulence, the larger is the critical value of incidence. Because the pressure distribution on the roof is strongly influenced by the turbulence of the oncoming flow, this turbulence will also affect the net loading on roof elements.

If a roof tile is inclined with respect to the free stream, the flow will separate from one side as soon as the angle of incidence exceeds a critical value. Visualization using the surface oil flow method shows that the vortex cones caused by the yawing flow separation at the leading edges result in the highest negative pressure coefficients close to the windward gable and the windward eaves. If the roof pitch is increased, the vortex cones decrease in strength. In regions of separated flow, the external pressure distribution on a tiled surface

coincides with the pressure distribution on the roof surface, as described by Peterka et al. (1997). In regions of attached flow, however, the pressure distribution on a tile is influenced by the flow around the tile. A typical example for the change in the external pressure distribution due to the element flow field is shown in Hazelwood (1980a).

The pressure distribution, indicating an acceleration region at the eave-facing end of the tile and a stagnation zone in front of the overlap of the tile in the upper row, results in an upward-lifting moment. The predominant geometric parameter for the pressure distribution is the tile thickness related to the non-overlapping length (Peterka et al., 1997). The fluctuations of the surface flow velocity caused by the instabilities of the flow field over the roof will change the pressure distribution and make the tiles clatter. When the wind load exceeds a certain value, the tiles are lifted up and the permeability of the roof surface increases rapidly. If this happens in a region with low external pressure, the wind load on the tiles will decrease. However, if lifting-up occurs because of surface flow action on the windward side, the stagnation effect will lead to an increase in the internal pressure and the up-lifting tile load. The internal pressure underneath the tiles affects the overall stability of the tiles and acts as the up-lifting tile load.

The small-amplitude vibrations of the roof tiles appeared first, the amplitude grew gradually larger as the wind velocity increased, and then fluttering with large-amplitude vibrations occurred, finally followed by scattering. The vibrational frequency was identified by image analysis of the high-speed video camera to measure relatively high-amplitude vibration in fluttering, which is considered to be the direct cause of tile scattering. The roof tiles do not always oscillate with a fixed vibrational frequency. Because vibrations with several frequencies affected the tiles and showed complex behaviors, some oscillation patterns were chosen at random from the data to be analyzed further. It was found that the amplitudes of tile vibration were larger than that of their natural frequency, and the vibration frequencies were low (in the range of 10 - 20 Hz).

The results obtained by the FFT analysis of the acceleration signals in the experiment in which fluttering occurred are shown in Fig. 14. The results show the oscillation of fluttering at a pitch angle of 24 degrees and a wind velocity of 40 m/s. The wind velocity was gradually increased from the start of the wind tunnel test to its maximum velocity, and the acceleration measurement and the video camera recording were then started simultaneously. The sampling time of the FFT analyzer was set at 2,048 points, the frequency resolution was set at 800 lines, and the frequency range was 0 - 5 kHz. Moreover, the peak frequency of approximately 470 Hz, which appeared just before tile scattering, was the natural frequency and was also recognized by FFT analysis. To minimize the effects of sampling time on the results of the FFT frequency analysis, the FFT frequency was analyzed using a sufficient sampling time. As a result the relatively high frequency, i.e., the natural frequency, as well as the relatively low frequencies were recognized.

It was observed in the wind tunnel test that the bolted roof tiles were lifted up, damaged, and then scattered by the wind, and they induced further fluttering and clattering by lifting up their neighboring roof tiles. In other words, it is believed that the amplitude was the largest in one cycle of tile vibration and the largest energy was obtained at those moments. The force acting on the roof tile can be estimated by Newton's second law of motion. In the case of the measured acceleration of 11 m/s^2 and the given mass of 2.8 kg, the force acting on the roof tile was 30.8 N.

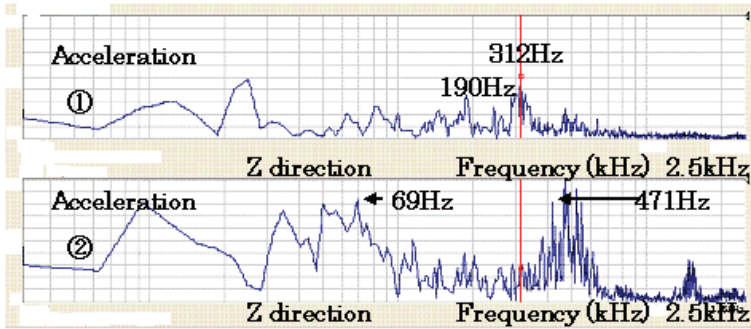


Fig. 14. Vibrational acceleration power spectrum of roof tiles at $\theta = 24$ degrees, $U = 40.0$ m/s

The natural frequency of the roof tile was measured by the impulse force hammer test. The center of a roof tile hung from the ceiling was hit by the impulse hammer. The natural frequency of the tile was analyzed in terms of a frequency-response function and a coherence function. By analyzing the frequency-response function, the peak frequency was found to be 478 Hz. The coherence function was strongly correlated with the frequency-response function (Fig. 5 (b)). It was recognized that the dominant frequency, which occurred just before the scattering shown in Fig. 14, almost coincided with the natural frequency of the tiles that was found by the impulse force hammer test. The natural frequencies of the roof tile hung from the ceiling were found to be between 430 and 460 Hz. The peak frequency of the roof tile appeared just before scattering, as shown in Fig. 14. The roof tiles were arranged on the model roof in order to measure their vibrational frequency caused by the wind at the center of the opposite side of the roof. It was found that the measured frequency was different from the frequency of fluttering and the natural frequency of the tiles (Naudascher et al., 1993; Hazelwood, 1980b).

These test results showed that the vibrational frequency of about 14 Hz almost coincided with the vibrational frequency that was obtained by analyzing the images of the high-speed video camera. On the other hand, the information of the acceleration and the results of the image were analyzed to specify the vibration occurring during fluttering. Low-frequency vibrations (10 - 20 Hz) were detected first (Fig. 14). Next, the significant peak amplitude of the natural frequency, which appeared just before fluttering, was also recognized. In other words, it is believed that the vibration at the relatively low frequency has a dominant effect on fluttering, and this natural frequency appears prior to fluttering because of the significant vibration at the relatively high natural frequency just before fluttering. Finally, the occurrence of vibration at the low frequency with a relatively large amplitude has the greatest effect on fluttering, and this mechanism can result in the lifting of the roof tiles. Hence, the dynamics of the roof tiles were due to the balance of their own weight, to which the external pressure was added by the fluid over the surface of the roof, and the internal pressure (i.e., the space between the roof tile and the roofing board). Because the external pressure and the internal pressure were changed, an unbalance of both pressures occurred, the tiles became unstable, and then fluttering occurred. It is believed that the relatively low-frequency vibrations have the greatest effect on scattering and can be the main factor that controls the behavior of the roof tiles.

4. Future research

Strong winds not only result in tile scattering leading to damage of tiles, but also result in water leak damage. Experiments pertaining to water leaks can be broadly classified into pressure box-type experiments and blower/water dispersion-type experiments. Pressure box-type experiments allow for the recreation of model wind pressures using devices for either increasing or decreasing pressure. Conversely, blower/water dispersion-type experiments make use of devices consisting of blowers and water dispersion equipment, which allow experiments to be conducted in conditions very similar to the actual flow of wind and rain during stormy weather. However, these types have both advantages and disadvantages, and neither of these types is able to reproduce the actual conditions of both rain damage and the damage caused by heavy winds simultaneously.

In future work, the authors will focus their attention on vibrations which cause the preliminary phenomena eventually leading to the scattering of tiles due to the effects of the wind, and will seek to understand the mechanism of these vibrations. Consequently, the authors will be able to connect together the mechanism and the preliminary phenomena of the occurrence of tile vibration induced by fluid flow. In accordance with these results, in future work the authors will go beyond the conventional understanding of water leakage amounts, aiming to establish appropriate experimental methods and to clarify the mechanism underlying the occurrence of water leak phenomena. The authors intend to investigate the previously unknown influence exerted by tile vibrations on water leaks. The ultimate goals are to provide a conclusive understanding of the effects of wind and to provide suggestions for possible improvement and redesign of roof tiles (Fig. 15).

5. Conclusions

An experimental study was conducted using wind tunnel tests in order to explain the behavior of roof tile vibration and the primary factors that affect scattering. The results are summarized as follows.

1. The basic mechanism that can lead to flow-induced vibrations of roof tiles is similar to that of the so-called fluttering instability, which appears as self-excited oscillations in the natural mode of a structure at a certain critical flow speed. The oscillating frequencies are related to the natural frequencies of vibration.
2. Surface flow is only important on the windward side of a roof and creates reasonable up-lifting moments only for wind directions roughly perpendicular to the eaves.
3. The effects of a roof's pitch angle on the fluttering of roof tiles were confirmed by analyzing acceleration information as the pitch angle was increased; the absolute value of acceleration and the amplitude also increased with increasing pitch angle.
4. The "wave motion of roof tiles" appeared just before scattering was observed, and the forces acting on two neighboring roof tiles were found to be either synchronized or out of phase.
5. Low-frequency vibrations, which have the greatest effect on scattering, were identified by a high-speed video camera, and the major factor that controls the behavior of the roof tiles was found to be the balance between the external pressure and the internal pressure.

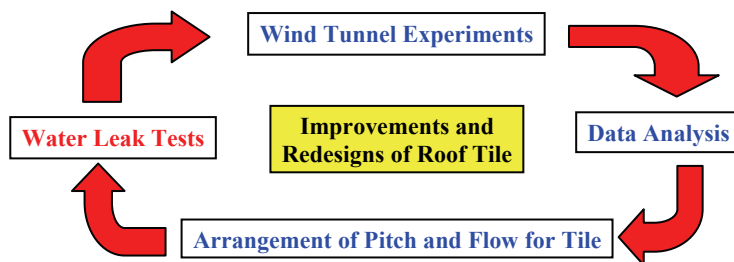


Fig. 15. Research plan for future work.

6. Acknowledgments

We wish to thank Dr. R. Nanba, Mr. K. Shibao, Mr. M. Satou and Mr. Y. Shibao of Shibao Co. Ltd. for their guidance in planning the present work. We also wish to thank the staff of Shimane Institute for Industrial Technology for their assistance. This work was supported by Grant-in-Aid for Scientific Research (C) of Japan Society for the Promotion of Science.

7. References

- Cermak, J. E. (1998). Wind damage mitigation - Wind engineering challenges, In: *Wind Effects on Buildings and Structures*, Riera, J. D. & Davenport, A. G. (Eds.), pp. 335-352, A. A. Balkema, 9054109599, Rotterdam.
- Ginger, J. D. (2001). Characteristics of wind loads on roof cladding and fixings. *Wind and Structures*, Vol.4, No.1, pp. 73-84.
- Hazelwood, R. A. (1980a). Principles of wind loading on tiled roofs and their application in the British standard BS5534. *Journal of Wind Engineering and Industrial Aerodynamics*, Vol.6 (July 1980) pp. 113-124, 0167-6105.
- Hazelwood, R. A. (1980b). The interaction of the principal wind forces on roof tiles, *Proceedings of 4th Coll. Industrial Aerodynamics, part1*, pp. 119-130, Aachen, 1980.
- Kramer, C., Gerhardt, H. J. & Kuster, H. W. (1979). On the wind-loading mechanism of roofing elements. *Journal of Wind Engineering and Industrial Aerodynamics*, Vol.4 (August 1979) pp. 415-427, 0167-6105.
- Kramer, C. & Gerhardt, H. J. (1983). Wind loads on permeable roofing systems. *Journal of Wind Engineering and Industrial Aerodynamics*, Vol.13 (December 1983) pp. 347-358, 0167-6105.
- Naudascher, E. & Wang, Y. (1993). Flow-induced vibrations of prismatic bodies and grids of prisms. *Journal of Fluids and Structures*, Vol.7, Issue 4 (May 1993) pp. 341-373, 0889-9746.

Peterka, J. A., Cermak, J. E., Cochran, L. S., Cochran, B. C., Hosoya, N., Derickson, R. G., Harper, C., Jones, J. & Metz, B. (1997). Wind uplift model for asphalt shingles. *Journal of Architectural Engineering*, (December 1997) pp. 147-155.